Jun 25th, 12:00 AM - Jun 27th, 12:00 AM

Full Proceedings: IJREWHS 2019

International Association for Hydro-Environmental Engineering and Research

Table of Contents

7th International Junior Researcher and Engineer Workshop on Hydraulic Structures, IJREWHS'19, B. HEINER and B. TULLIS (Eds), Report 1, U.S. Bureau of Reclamation, Denver, CO, USA - ISBN 978-0-578-69809-0
https://doi.org/10.26077/5qw4-ne72

THREE-DIMENSIONAL NUMERICAL MODELING OF A SCROLL VORTEX INTAKE

S.N. CHAN
Department of Civil and Environmental Engineering and Institute for Advanced Study,
The Hong Kong University of Science and Technology, Hong Kong, China, treechansn@ust.hk

Abstract: Scroll vortex intakes are vortex drop structures commonly used in water supply, drainage and sewerage systems, characterized by a vortex chamber with its wall curling inwards to the dropshaft and a horizontal bottom. The stormwater flows into the intake via an eccentrical approach channel, which imparts vortex motion to the flow, forming a swirling vortex flow with a stable air core through the center of dropshaft. Over past decades, much effort has been devoted to investigating the scroll intake vortex flow, yet the understanding and predictions of the vortex flow is still far from complete due to a lack of detailed investigation on its velocity field and air core characteristics. In this work, a three-dimensional (3D) computational fluid dynamics (CFD) model using the Volume-of-Fluid (VOF) method is used for investigating the complex flow of a scroll vortex intake. The CFD model predictions are validated with detailed flow profile, flow velocity and air core measurements on a physical hydraulic model. It is found that the vortex flow in the scroll chamber resembles a free vortex and the circulation is approximately equal to that at the inlet to the chamber, with a thin bottom boundary layer. For the vortex flow at the bellmouth outlet, the tangential velocity distribution satisfies a Rankine vortex. Furthermore, the vortex flow at the bellmouth outlet possesses a circulation constant which is smaller than that in the chamber.

Keywords: scroll vortex intake, swirling flow, air-core, Volume-of-Fluid method.

INTRODUCTION

Scroll vortex intakes are vortex drop structures used in water supply, drainage and sewerage systems. A scroll vortex intake (c.f. Fig. 1) is characterized by a vortex chamber with its wall curling inwards to the dropshaft and a horizontal bottom. The water flows into the intake via an eccentrical approach channel. Thus the intake can impart the vortex motion to the flow and then a swirling vortex flow with a stable air core is formed along the dropshaft. The air core acts as a chimney for the air trapped into the approaching flow to escape freely, and the extended path of water motion increases the energy dissipation of the flow. Therefore, such vortex intakes usually possess the hydraulic characteristics of low air entrainment and high energy dissipation.

The concept of scroll intake design was first introduced by DRIOLI (1947). Since then, much effort has been devoted to predict the scroll intake vortex hydraulic characteristics. Past investigation

heavily depends on physical hydraulic models and the idealized vortex flow pattern for modeling the flow process (JAIN and KENNEDY, 1983; LEE et al. 2006; MULLIGAN et al. 2016). A standard design of scroll intake geometry has been proposed by DRIOLI (1969) and JAIN and ETTEMA (1987). A deeper understanding of the vortex flow process in scroll intakes promotes the attempts for reaching a rational approach for scroll intake design. VIPARELLI (1950) proposed a semi-empirical approach for predicting the head-discharge relationship of scroll intake. ACKERS and CRUMP (1960) proposed an analytical approach for scroll intakes by assuming the vortex flow satisfies a free vortex model. PICA (1970) proposed an improved semi-empirical solution that predicts the head-discharge relationship, later simplified into a dimensionless form by HAGER (1985). However, the prediction of the air core size by many of these theoretical models fails to agree well with experiment and field observation data. The scarce data of the detailed vortex flow field in literature make it difficult to develop a more accurate rational model for hydraulic design of scroll intakes. GUO (2012) measured, for the first time, the detailed flow field of a typical scroll intake design using Laser Doppler Anemometry (LDA). Based on the experimental data, the theory of ACKERS and CRUMP (1960) is considered the most justified, and an improved model is proposed.

Attempts have been made to model the air-water flow in vortex intake problems using three-dimensional (3D) computational fluid dynamics (CFD) models with the Volume-of-Fluid (VOF) method. Using VOF, the interface between the water and air can be located and tracked when it moves through the computational domain. CHAN et al. (2018) used a 3D CFD model to study the detailed flow structures of a stable tangential vortex intake. The model prediction was validated with measurements of head-discharge, air core and velocity profiles, which sheds light on the physics of a tangential vortex intake. An empirical relationship was also established for predicting air core size according to the flow and geometry of the intake.

This paper presents the 3D CFD modeling results of a scroll vortex intake of typical design. The numerical model results are validated against flow profile, velocity and air core measurements on a physical model of a scroll vortex intake. In this paper, the details of the CFD model are first presented; the numerical model results are then discussed and compared with experimental measurements.

COMPUTATIONAL FLUID DYNAMICS MODEL

The scroll vortex intake model investigated in this study is designed based on the standard geometry recommended by DRIOLI (1969). Fig. 1a schematically shows the geometry and key dimensions of the scroll vortex chamber. The chamber wall consists of four arcs with decreasing radii in the flow direction. The center of each arc is offset from the dropshaft center by a certain distance, which is determined by an eccentricity $e = (B + s)/7$, where $B = 0.167$ m, approach channel width, and $s = 27$ mm, offset distance between the approach channel wall and the chamber wall. The radius of each arc, R_1 to R_4, is then determined by following relations (Eq. 1):

7th International Junior Researcher and Engineer Workshop on Hydraulic Structures, IJREWHS'19, B. HEINER and B. TULLIS (Eds), Report 1, U.S. Bureau of Reclamation, Denver, CO, USA - ISBN 978-0-578-69809-0
https://doi.org/10.26077/5qw4-ne72

$$R_4 = D/2 + \delta + a + e,\ R_3 = R_4 + e,\ R_2 = R_3 + 2e,\ R_1 = R_2 + 2e,\ \Delta = R_1 + e - B/2 \quad (1)$$

In Eq. (1), the dropshaft diameter, $D = 0.12$ m; radius of curvature of the dropshaft entrance, $\delta = 0.052$ m; distance between the top of bellmouth and the chamber wall, $a = 0.028$ m; and the eccentricity between the approach channel and the dropshaft, $\Delta = 0.25$ m. B and D are first determined based on the design discharge. Then Δ, s and a are chosen based on structural considerations. Finally e and R_1 to R_4 are determined based on Eq. (1). Experimental measurements of flow profile, velocity field and air core sizes of such scroll vortex intake design has been reported by LEE et al. (2006) and GUO (2012).

Fig. 1 – (a) Geometry definition of a scroll vortex intake, (b) 3D view of the computational mesh.

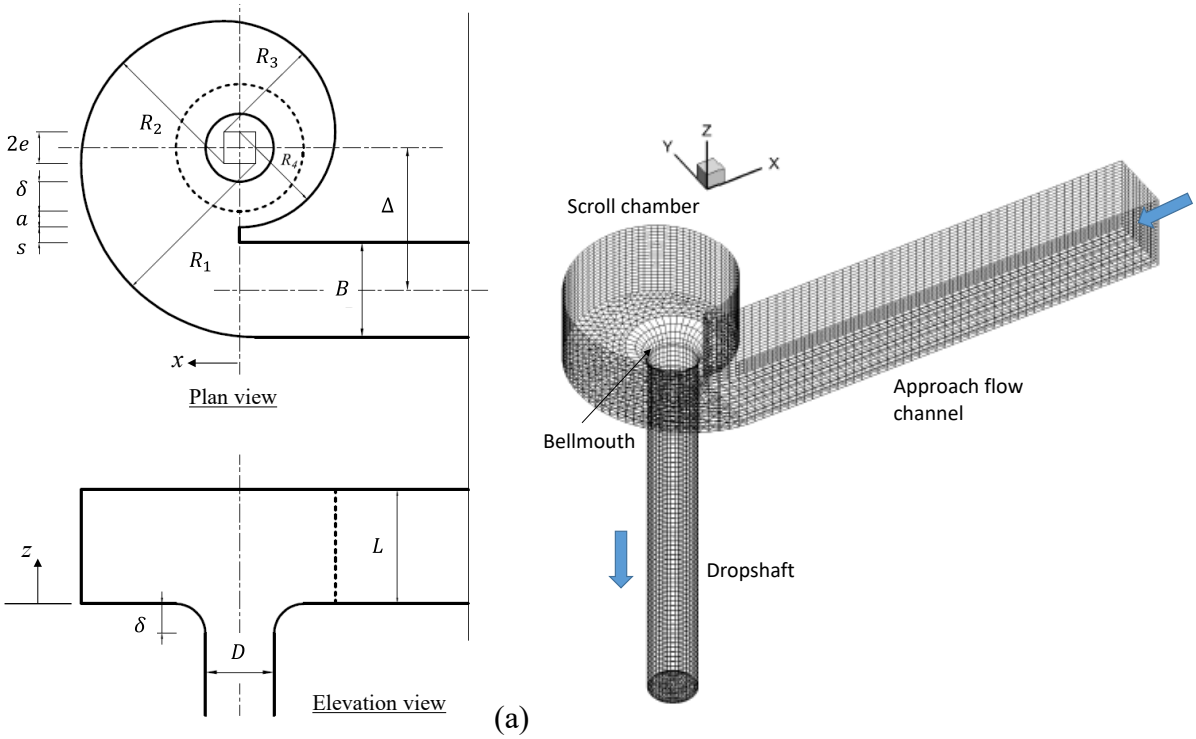

The VOF model (HIRT and NICHOLS, 1981) predicts water flows with a free surface by solving a single set of momentum equations and tracking the volume fraction of water and air throughout the domain. The tracking of the interface between the phases is accomplished by the solution of the transport equation for the volume fraction of water phase α_w (Eq. 2):

$$\frac{\partial}{\partial t}(\alpha_w \rho_w) + \nabla \cdot (\alpha_w \rho_w \mathbf{U}) = 0 \quad (2)$$

A single momentum equation is solved throughout the domain, and the resulting phase-averaged velocity field $\mathbf{U} = (u, v, w)$ is shared among the phases (Eq. 3).

$$\frac{\partial}{\partial t}(\rho\mathbf{U}) + \nabla\cdot(\rho\mathbf{U}\mathbf{U}) = -\nabla P + \nabla\cdot[\mu_t(\nabla\mathbf{U} + \nabla\mathbf{U}^T)] + \rho\mathbf{g} \quad (3)$$

where the air-water mixture density, $\rho = (1\text{-}\alpha_w)\rho_a + \alpha_w\rho_w$; μ_T is the dynamic molecular viscosity obtained from a k-ε turbulence model; P is the pressure; the gravitational acceleration vector, $\boldsymbol{g}$ = (0,0,-9.81) m/s^2; ρ_w and ρ_a are water and air densities, respectively. The air-water interface is defined at water volume fraction $\alpha_w = 0.5$.

The governing equations (2) and (3), and the k and ε equations of the turbulence model were solved numerically in the CFD software of ANSYS FLUENT 15 (ANSYS INC., 2013). A second order upwind advection scheme was used for momentum and density, while a first order upwind advection scheme was used for k and ε. The volume fraction equation is spatially discretized using the Modified High Resolution Interface Capturing (HRIC) Scheme in FLUENT. Convergence for each time step was declared when the normalized residual is less than 10^{-4} for all variables.

An unstructured boundary-fitted model grid was used (Fig. 1b). The computational mesh has 69,944 grid cells with hexahedral cells for the approach channel and dropshaft, and triangular-prismatic cells for the scroll chamber with mesh refinement close to the dropshaft wall. The minimum grid size near the dropshaft wall region is 2 mm. Mesh convergence was tested using a fine mesh with 436,880 cells. The differences on the predicted approach flow depth, air core size and swirling velocity are less than 5%.

The computational model has three open boundaries: the inlet, the outlet of the vortex dropshaft, and the top atmospheric boundary. The upstream inflow of the approach channel is prescribed with the total water flow rate and a head discharge relationship at the inlet of the model measured experimentally. The upper boundary of the CFD model is prescribed with zero gauge pressure/atmospheric pressure. The dropshaft outlet is prescribed with zero gauge pressure. A roughness height of 0.01 mm is used for all wall boundaries.

Numerical simulations were carried out for five representative flow rates of Q = 2, 4, 6, 8 and 10 L/s. The supercritical flow in the approach channel and the vortex intake developed from the inlet. A time step of 0.001 s was used for the simulation; typically about 20 s of flow simulation were required for the vortex flow to reach steady state with a computation time of approximately 20 h.

RESULTS AND DISCUSSIONS

Flow-profile and head-discharge relation

Figure 2a shows the CFD predicted general vortex flow features for the case of Q = 6 L/s. It is seen that the flow surface is depressed as it approaches to the dropshaft. An air core is formed in the center

and continues all the way along the dropshaft. After entering the dropshaft, the flow clings to the shaft wall and descends down the shaft wall vertically with a decreasing axis swirl. The flow depth in the approach channel and the scroll chamber increase smoothly with increasing discharge. No unstable feature is observed within this range of discharge (Q = 2-10 L/s). Figure 2b shows that the dimensionless approach flow depth h_a/D (measured at 70 mm upstream of the scroll chamber inlet using a point gauge) increases linearly with the dimensionless discharge $Q/(gD^5)^{1/2}$. The CFD prediction follows the trend of measured head-discharge relationship closely although it under-estimate the approach flow depth at high flows by a maximum relative error of 15%.

Fig. 2 – (a) Predicted free surface for Q = 6 L/s; (b) head-discharge relationship of the scroll vortex intake.

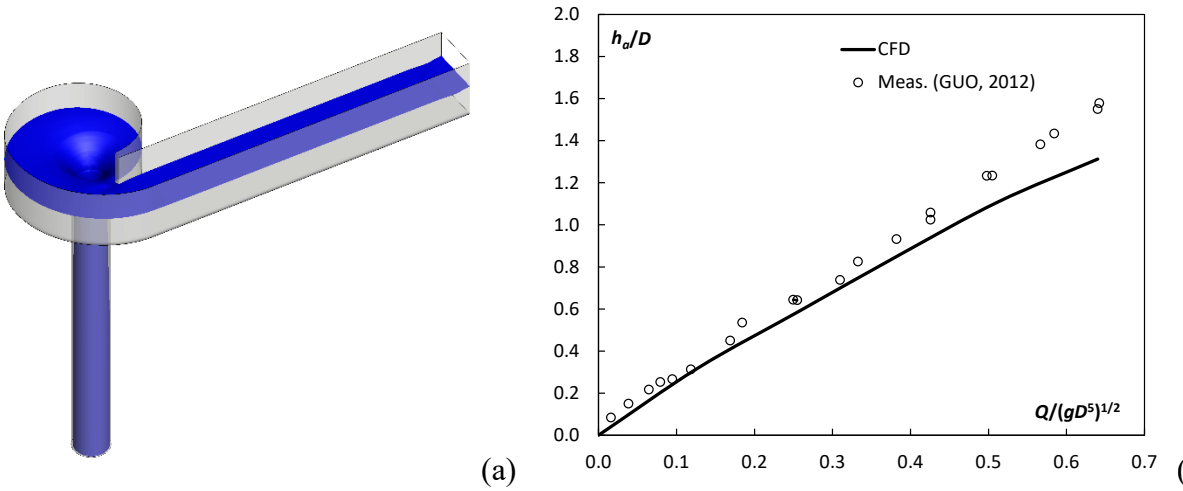

Vortex air core

Fig. 3a shows the predicted air core at the throat for Q = 10 L/s. The air-core is not axisymmetric; it has a larger flow thickness at the quadrant between the azimuth angles of 0º and 270º. The minimum air core (throat) lies between the bellmouth and the bottom of the scroll chamber. The minimum air core size along the vertical direction of the intake A_m decreases with increase in discharge. The predicted minimum air core size ratio $\lambda_m = A_m/(0.25\pi D^2)$ compare satisfactorily with the measurement with a maximum relative error of about 30% at high flows (Fig. 3b).

Scroll chamber flow

Due to the eccentric geometry, the inflow from the approach channel imparts angular momentum and results in a swirling flow in the scroll chamber (Fig. 4a). The swirling flow drains down the dropshaft through the bell-mouth. Fig. 4b shows the tangential velocity distribution at the azimuth of 75° (c.f. Fig. 4a) for Q = 6 L/s. Generally, the distribution of tangential velocity v_t decreases with greater radial distance r from the center of chamber. The vortex circulation $\Gamma = v_t r$ reveals that the flow satisfies a free vortex: Γ is approximately constant over r and equals the circulation at inlet $\Gamma = v_A \Delta$ (where v_A

is the average approach flow velocity = Q/Bh_a), except near the chamber bottom and at very low discharges where the viscous effect becomes significant. The CFD predicted tangential velocity and vortex circulation have excellent agreement with the measurement (Fig. 4b).

Fig. 3 – (a) Predicted air core at the throat for Q = 10 L/s, (b) Variation of minimum air core ratio with discharge.

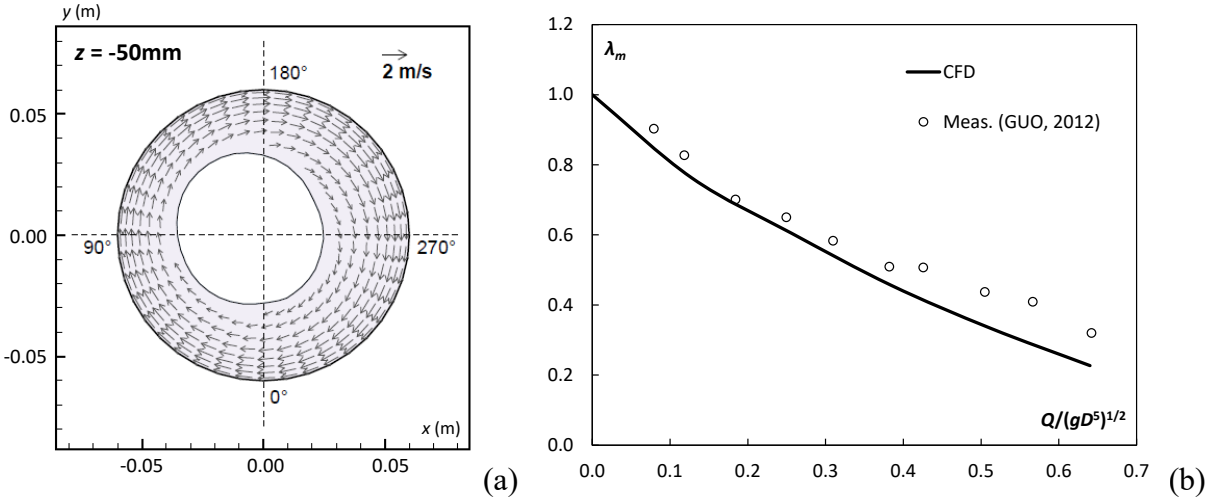

Fig. 4 – (a) Flow field and air core at the scroll chamber, (b) distribution of tangential velocity v_t at the scroll chamber of azimuth 75° for Q = 6 L/s, Γ = 0.08 m^2/s. Measured data from GUO (2012).

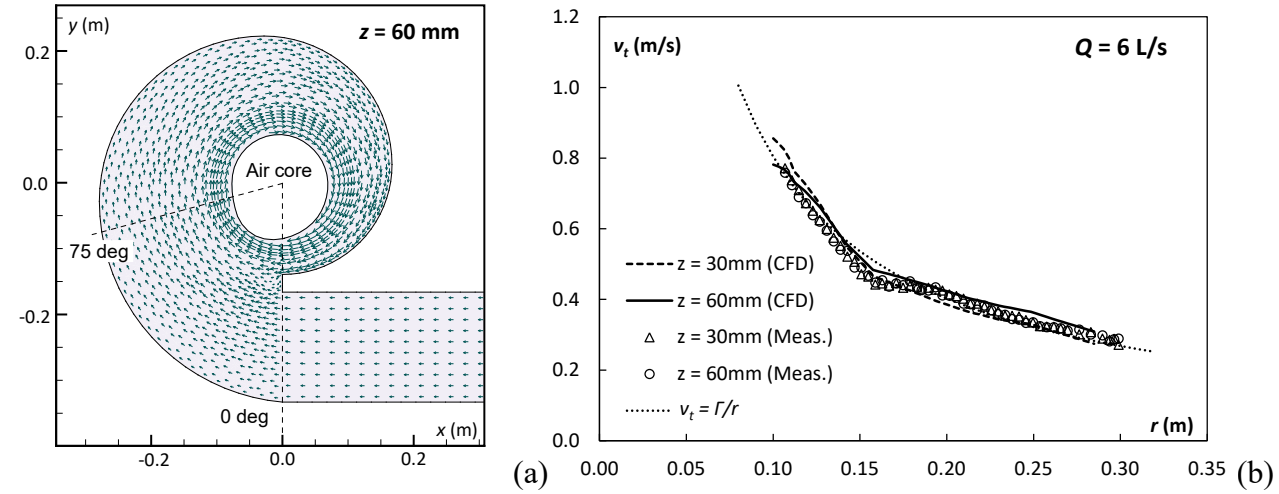

Bellmouth flow

The existing scroll vortex theories consider the bellmouth as a control section, thus it is important to understand its velocity distribution to validate the assumptions of these theories. Fig. 5a shows the distribution of tangential velocity v_t and vertical velocity v_z of the bellmouth for Q = 6 L/s. In general, the flow can be divided into three regions: 1) a forced vortex region starting from the free surface of the air core to a certain radial distance within the vortex flow, where tangential velocity increases

with greater radial distance from the shaft center; 2) a free vortex region in the remaining outside area where tangential velocity decreases; and 3) a boundary layer near the wall. This is similar to a Rankine combined vortex. The formation of the forced vortex region is due to the viscous dissipation at the air core region induced by the flow turbulence. It can be seen that the forced vortex region (increasing v_t) dominates the tangential flow field at the bellmouth (Fig. 5a).

In the forced vortex region, v_z decreases with increasing radial distance. This is consistent with the tangential velocity distribution of a Rankine combined vortex and the conservation of energy: the vertical velocity is constant for a free vortex flow (BINNIE and HOOKINGS, 1948). Since both tangential velocity and pressure increase with radius in the forced vortex flow, the vertical velocity decreases to maintain energy conservation. The prediction by CFD shows a relatively large region of forced vortex with increasing v_t, and a decreasing trend of vertical velocity against radial distance (Fig. 5a). The numerical prediction indicates that the assumptions of free vortex flow at the bellmouth by the model of ACKERS and CRUMP (1960) is not entirely correct. The vortex circulation, $\Gamma = v_t r$, shows an increasing trend with increasing radius (Fig. 5b). The maximum value of circulation is between 0.060 and 0.070 m^2/s, which is significantly lower than the initial circulation $\Gamma = 0.08$ m^2/s ($\Gamma = v_A \Delta$).

Fig. 5 – (a) Distribution of tangential velocity v_t and vertical v_z velocity, (b) distribution of vortex circulation at the bellmouth. $Q = 6$ L/s, azimuth angle of 0°. Measured data from GUO (2012).

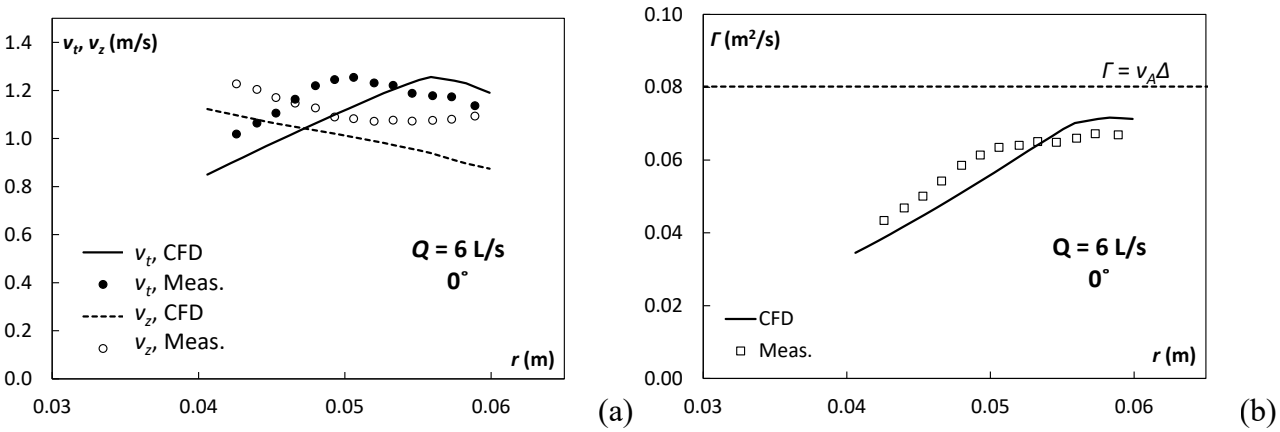

CONCLUSIONS

In this study, the flow of a scroll intake vortex is studied using three-dimensional (3D) computational fluid dynamics (CFD) modeling. The head-discharge relationship and minimum air core sizes have been predicted by the CFD model. The minimum air core of the vortex flow occurs within the bellmouth. The vortex flow in the scroll chamber is similar to a free vortex with a circulation approximately equal to the circulation at the inlet, and the circulation gradually decreases as the flow swirls around the scroll chamber.

The predicted tangential velocity distribution of the vortex flow at the bellmouth is dominated by the forced vortex flow. The predicted vertical velocity distribution in the bellmouth decreases with increasing radial distance. The CFD modeling results provide useful insight for improving the current theoretical models for scroll vortex intake design.

ACKNOWLEDGMENTS

This study was supported by a grant from the Hong Kong University of Science and Technology (IGN17EG05).

REFERENCES

ANSYS INC. (2013). *ANSYS FLUENT 15.0 Theory Guide*.

ACKER, P., and CRUMP, E.S. (1960). "The vortex drop." *Proceedings of Institute of Civil Engineers, Part I*, 16(4), 433-442.

BINNIE, A.M., and HOOKINGS, G.A. (1948). "Laboratory experiments on whirlpools." *Proceedings of the Royal Society of London, Series A*, 194(1038), 398-415.

CHAN, S.N., QIAO, Q.S. and LEE, J.H.W. (2018). "On the three-dimensional flow of a stable tangential vortex intake." *Journal of Hydro-environment Research*, 21, 29-42.

DRIOLI, C. (1947). "Su un particolare tipo di imbocco per pozzi di scarico." *L'Energia Elettrica*, 24(10), 447–452 (in Italian).

DRIOLI, C. (1969). "Esperienze su installazioni con pozzo di scarico a vortice." *L'Energia Elettrica*, 46(6), 399–409 (in Italian).

GUO, J.-H. (2012). *Velocity field measurement of a scroll vortex intake flow*. M.Phil. Thesis, The University of Hong Kong.

HAGER, W. (1985). "Head-discharge relation for vortex shaft." *Journal of Hydraulic Engineering*, ASCE, 111(6), 1015–1020.

HIRT, C. W. and NICHOLS, B. D. (1981). "Volume of fluid (VOF) method for the dynamics of free boundaries." *Journal of Computational Physics*, 39(1), 201-225.

JAIN, S.C. and KENNEDY, J.F. (1983). *Vortex-Flow Drop Structures for the Milwaukee Metropolitan Sewerage District Inline Storage System*, Report No. 264, Iowa Institute of Hydraulic Research, The University of Iowa, Iowa City, Iowa.

JAIN, S.C., and ETTEMA, R. (1995). "Swirling flow problems at intakes." In: *Vortex Intakes, IAHR hydraulic structures design manual 1*, J. Knauss eds., Balkema, Rotterdam, The Netherlands, 125-137.

LEE, J.H.W., YU, D.Y. and CHOI, K.W. (2006). *Physical hydraulic model tests for Lai Chi Kok transfer scheme intake structure.* Croucher Laboratory of Environmental Hydraulics, The University of Hong Kong.

MULLIGAN, S., CASSERLY, J. and SHERLOCK, R. (2016). "Effects of geometry on strong free-surface vortices in sibcritical approach flows." *Journal of Hydraulic Engineering*, 142(11),

04016051.

PICA, M. (1970). “Scaricatori a vortice.” *L'Energia Elettrica*, 47(4), 1–18 (in Italian).

VIPARELLI, M. (1950). “Su un particolare tipo di imbocco e sull'efflusso con vortice.” *L'Energia Elettrica*, 27(10), 610–624 (in Italian).

7th International Junior Researcher and Engineer Workshop on Hydraulic Structures, IJREWHS'19, B. HEINER and B. TULLIS (Eds), Report 2, U.S. Bureau of Reclamation, Denver, CO, USA - ISBN 978-0-578-69809-0
https://doi.org/10.26077/2s9r-ad12

PHYSICAL MODEL TESTING OF SUPERCRITICAL FLOW DIVERSION FOR COMBINED SEWER OVERFLOW CONTROL

Tony LOESER
IIHR - Hydroscience & Engineering, University of Iowa, United States, tony-loeser@uiowa.edu

Abstract: In this study, a 1:8 scale physical hydraulic model was used to demonstrate that a novel widening ramp concept was applicable for diverting supercritical inflows for a proposed regulator chamber and also to establish design dimensions for the proposed structure to meet project goals. The following conclusions were determined from the testing. The widening ramp concept proposed for this project was able to adequately pass the full range of design inflows of 0-425 MGD without experiencing undesirable flow conditions that would produce excessive water depths while meeting the diversion goals of the project. The proposed diversion conduit could adequately pass the range of diverted discharges without affecting the hydraulic performance of the regulator chamber. The results of this study establish the potential for the widening ramp structure to be utilized for tackling other challenging supercritical flow diversion problems.

Keywords: Supercritical flow diversion, Widening ramp, Combined sewer separation

INTRODUCTION

Combined sewer systems (CSS) are single-pipe systems that convey sanitary sewer and/or industrial wastewater to a wastewater treatment facility. During rainfall events, storm water runoff is also routed to this pipe network and combines with the wastewater. For large rainfall events, the capacity of the CSS or the wastewater treatment facility may be exceed and results in the discharge of untreated sewage directly to surface water bodies via safety outlets. This is called a combined sewer overflow (CSO). CSO reduction/elimination is a priority water quality objective for nearly 860 municipalities (EPA, 2018) across the United States that operate combined sewer systems.

A regulator chamber is a structure placed in-line on a CSS and is used as a means to divert flows to an offline storage or conveyance system that can accommodate higher inflow volumes. Subsequently, the diverted inflows can still be treated prior to final discharge to a surface water body. CSO's can also be reduced by intercepting storm water runoff prior to it entering the CSS. For this project, storm water interception was the focus, in which the diverted flows are being routed to a treatment plant prior to final discharge. The design challenge of the regulator chamber discussed in this study is the steepness of the upstream existing sewer, which produces supercritical inflow conditions. Typical flow diversion measures that work for flow in the subcritical regime do not work as well for supercritical flows due high energy losses, which can result in a hydraulic jump and potentially

undesirable flow depths.

A 1:8 scale physical hydraulic model was used to demonstrate that a unique widening ramp concept that had been successfully implemented in a stormwater regulator in New South Wales, Australia (VAN DRIE and HERNGREN, 2006 and 2007) would be applicable for diverting supercritical inflows for a proposed regulator chamber in Lynchburg, Virginia. The widening ramp concept was identified as a potential option by a design team from the Alexandria, Virginia office of Greeley & Hansen, Inc. (G&H). Through G&H's communications with Rudy VAN DRIE (referenced above) and a subsequent literature search, it is believed that the New South Wales regulator is the only documented application of such a structure being used for diverting supercritical inflows.

The proposed regulator chamber (inset in Figure 1) included a widening channel section combined with a raised channel bottom (ramp) and a sidewall diversion orifice upstream of the ramp.

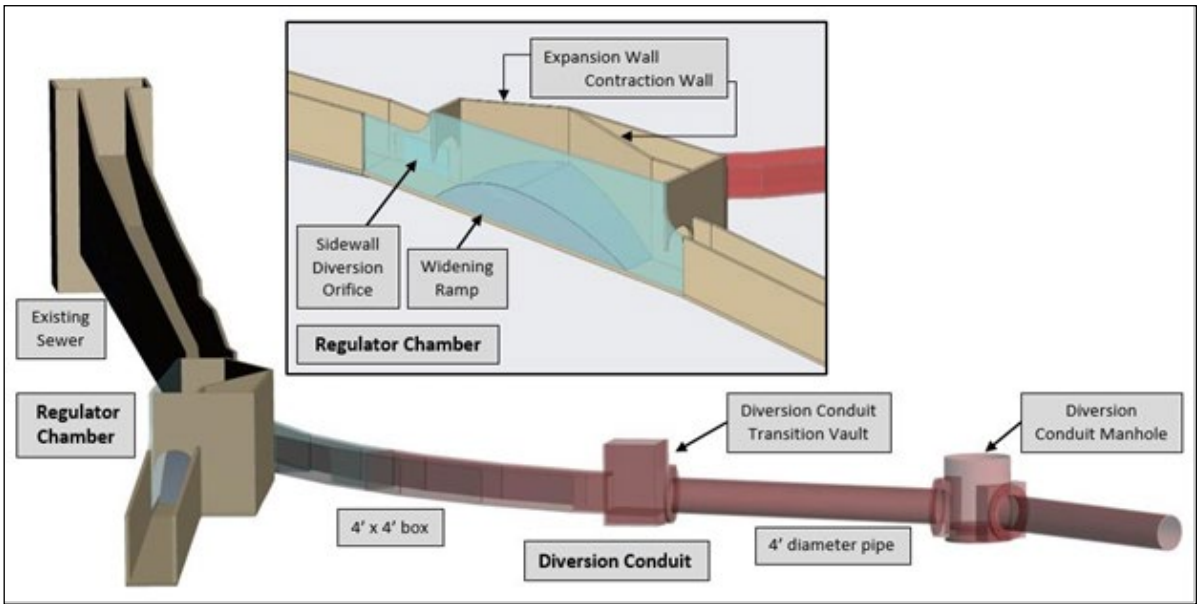

Fig. 1 – Physical model study components

The premise of the widening ramp regulator chamber is that energy is dissipated as the inflow contacts the ramp. For low inflows, a hydraulic jump occurs and the energy dissipation is great enough that a resulting conjugate depth standing wave forms in the area upstream of the ramp and the flow enters the diversion conduit via the sidewall orifice. Up to a certain inflow threshold, 100% is diverted. As inflow increases beyond this threshold, a portion of the inflow is diverted and the remainder exits the regulator chamber over the ramp. For a range of inflows, a hydraulic jump still occurs and a conjugate depth standing wave remains present upstream of the ramp. The widening of the channel/ramp allows for lateral expansion of the flow that exits over the ramp instead of vertically, which could cause undesirable water depths. At a point, identified herein as the hydraulic jump sweeping out, the energy in the inflow becomes great enough that a hydraulic jump no longer occurs and the portion of the flow that exits over the ramp remains supercritical.

In this project, the City of Lynchburg's 2014 Long Term Control Plan defined the project's diversion

goals. The overall project goals were to design the regulator chamber such that it would: (1) completely intercept inflows up to 60 million gallons per day (MGD) and divert them into the adjacent diversion conduit; (2) pass peak inflows up to 425 MGD through the regulator chamber without experiencing unacceptable water depths, while still diverting a portion of the inflow; and (3) limit the diverted flows during high flow events to less than 80 MGD for inflows up to 360 MGD. The physical model was used to determine the design dimensions of the proposed structure to meet those objectives.

MODEL DESIGN, CONSTRUCTION, AND CONSIDERATIONS

The physical model was constructed with marine plywood and transparent acrylic segments where visualization of the diversion structure hydraulics were desired. Testing was performed in two phases. Phase I focused on proving that the concept of using a widening ramp for supercritical flow diversion was feasible for the regulator chamber and for preliminary determination of the dimensions required to meet the objectives as specified in the City's 2014 Long Term Control Plan. Phase II included testing a variety of geometries and sizes for the sidewall diversion orifice opening to balance the flow diversion capabilities at low inflow and high inflow conditions, as well as to determine if the diversion conduit could adequately pass the diverted discharges without adversely affecting the hydraulic performance of the regulator chamber.

Physical model extent

The existing sewer is constructed of rock blocks with varying geometry and slopes. It has approximate dimensions of 5.2-feet wide by 7.2-feet tall with an arch shaped top near the flow diversion location. The physical model included approximately 229 feet (full-scale dimension) of the existing sewer upstream of the location of the proposed regulator chamber. The upstream sewer section included a variable width section (~92 feet), capturing the first three width changes closest upstream of the proposed regulator chamber. Three grade changes were captured in the existing sewer portion of the model as well.

Model scaling considerations

Accurate simulation of flows in a laboratory model requires geometric, kinematic, and dynamic similarity (ETTEMA, et al., 2000). However, it is not possible to achieve similarity of all forces when utilizing the prototype fluid and using an alternative fluid is generally not practical, so similarity is sought only among the dominant forces (NOVAK, et al., 2010). Flows that involve free surfaces, such as flows in conduits like the one being tested, are dominated by gravitational, inertial, and pressure forces. The Froude number is a dimensionless number defining the ratio of inertial to gravitational forces and kinematic similarity (i.e. similarity of velocity and acceleration components) is achieved if Froude numbers for the model equal the Froude numbers of the full-scale structure

(prototype). Energy dissipation is adequately simulated in a Froude-scaled model, provided the flow is sufficiently turbulent (NOVAK, et al., 2010). For this study, the physical model was constructed at 1:8 scale based on Froude scaling laws. This scale provides adequate Reynolds numbers to ensure fully turbulent flow.

Sewer roughness

The painted plywood channel surfaces representing the existing sewer were smooth in the model, resulting in higher velocities in the approach channel than would occur in the existing combined sewer, which is constructed of rock blocks with varying geometry. Approach velocities, and subsequent energy associated with momentum of the flow, influence the performance of the design by affecting the flow depth in the channel and location of the hydraulic jump/conjugate depth standing wave when it forms for certain conditions.

Approach velocities in the existing sewer for specified discharges were estimated utilizing computer hydraulic modeling simulations produced by G&H using existing field dimensions, as well as a computer hydraulic model (HEC-RAS) developed by IIHR – Hydroscience & Engineering using scaled model dimensions and inflows. Based on the results of the computer modelling, roughness elements (e.g., coarse sand, pebbles) were added iteratively to the plywood floor and walls of the model sewer approach channel to reduce velocities to match expected values.

Roughness can be difficult to quantify. In application, empirical resistance coefficients have historically been used. One such resistance coefficient is the Gauckler-Manning Coefficient, which is often called the Manning's Roughness Coefficient and denoted as n. This empirically derived coefficient is dependent on several factors, including surface roughness and sinuosity. Based on observed flow depths (occurring at measurement sections in the model with known channel width and slope) resulting from known discharges, an n value was estimated using Manning's equation. Prior to adding the roughness elements, the Manning's n value in the smooth channel was approximately 0.009. The Manning's n value for the model with the roughness elements added was approximately 0.0147. Froude scaling of Manning's n is described as $n_p = n_m \times L_r^{1/6}$ (WEBB, et al., 2010), where the subscripts p and m denote prototype and model values respectively. L_r is the geometric length ratio used for the physical model, which in this case was 8. Using this scaling method, an equivalent prototype Manning's n for the Lynchburg channel would be approximately 0.0208, which falls in the typical range of published Manning's n tables (CHOW, 1959) for channels constructed such as the existing Lynchburg sewer.

Flow conveyance and measurement

A 75hp pump with a variable frequency drive (VFD) controller supplied water to the model. Precise control of model flow rates was provided by a butterfly valve in the feed line and the VFD. The volumetric flow rate was measured with a Badger M2000 electromagnetic flow meter. The manufacturer states accuracy of ± 0.25% for the range of flows tested. The diversion discharge was determined using a v-notch weir built into a tail box that provided adequate stilling of the water

surface for accurate depth measurements, which were obtained using a Rickly Type-A point gauge. Water surface elevations in the model segment representing the existing sewer and depth measurements over the crest of the widening ramp were obtained with the same style point gauges. Velocity measurements were collected using a Nixon Streamflo series instrument with a 404 standard high speed velocity probe.

TEST RESULTS AND OBSERVATIONS

Phase I – Initial performance of concept

The physical model for the regulator chamber was initially constructed with a 2:1 expansion wall, a 2:1 contraction wall, and a ramp height of 2.6-feet (full-scale dimension). The initial configuration proposed for the structure was based on the design methodology developed by VAN DRIE and HERNGREN (2006 and 2007) for maintaining critical flow over the ramp during the 25-year storm inflow (360 MGD). However, the ramp height was determined to be too low to adequately divert 100% of inflow up to 60 MGD. It was determined that the ramp height needed to be 5.1-feet to be high enough to stop the inflow and create the standing wave condition for 60 MGD inflow. Periodic splashing or surging over the ramp crest was observed from instability and movement of the hydraulic jump/standing wave location. Testing with the increased ramp height identified that the full-sized sidewall diversion orifice created when abutting a 4-foot square diversion conduit to the chamber wall allowed too large of diverted discharges at higher inflow conditions. Subsequently, an adjustable orifice restrictor plate was placed across the top of the opening to reduce diverted discharges. The addition of the restrictor plate to the top of the sidewall orifice demonstrated that it was feasible to get the regulator chamber to operate near the desired range of flows. However, it was observed that adding a restrictor plate to regulate diverted discharge during high inflows slightly reduced the diverted discharge for the 60 MGD inflow. It was determined that the widening of the channel at a 2:1 expansion rate performed adequately over the range of tested flows. It was observed that as inflows increased and the supercritical flow passed over the ramp, there was a noticeable wave and upwelling that resulted from the water striking the wall of the 2:1 contraction section.

The Phase I physical model testing demonstrated proof of concept that the novel widening ramp diversion structure could be feasible for utilization in the Lynchburg regulator chamber. It was recommended the concept ramp be replaced with a new ramp equivalent to 5.25-foot high (full-scale) and that the diversion sidewalls be changed from 2:1 expansion and 2:1 contraction to 2:1 expansion and 3:1 contraction.

Phase II – Final testing with addition of diversion conduit

The physical model construction was modified to include a ramp that was built 5.25-feet high (full-scale) with a 2:1 expansion wall and a 3:1 contraction wall. The diversion conduit was also added to determine if the conduit could adequately pass the diverted discharges without adversely affecting

the hydraulics in the regulator chamber. As a part of the Phase II testing, the sidewall diversion orifice restrictor plate was further evaluated to optimize the balance of flow diversion capacity at low flow and high flow conditions. The final configuration selected for the diversion opening was 1.5-feet high by 9-feet wide (full-scale).

Inflow and corresponding diverted discharges

Inflow rates to the regulator chamber were selected based on return period inflows provided by G&H, as well as for intermediate inflow rates where unique phenomena were observed to occur. For the final testing configuration with 60 MGD inflow, diverted discharge was measured to be 57.2 MGD. Once again, intermittent splashing occurred over the ramp as a result of the transient nature of the hydraulic jump/standing wave moving in the vicinity of the face of the ramp and the sidewall orifice. See Figure 2 for photo of the regulator chamber at 60 MGD inflow.

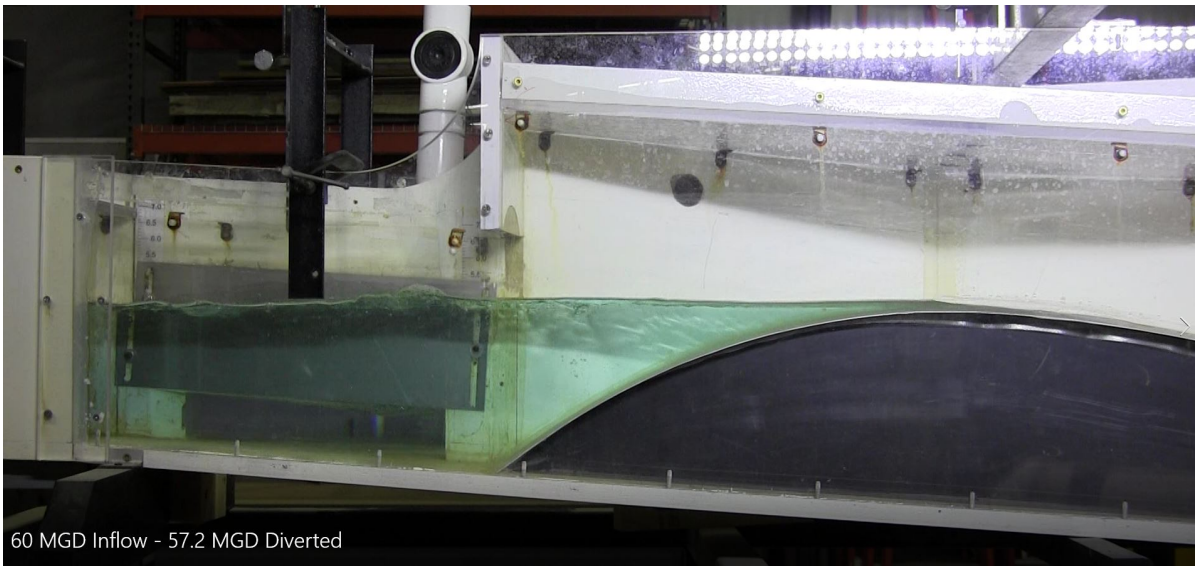

Fig. 2 – Final testing configuration of the regulator chamber – 60 MGD inflow

Diverted discharge increased with inflow up to approximately 212 MGD. At this point, the hydraulic jump was still occurring in the regulator chamber and the depth of water over the full width of the sidewall orifice was at a maximum, resulting in a diverted discharge of 76.7 MGD. As inflow increased beyond 212 MGD, the location of the hydraulic jump/standing wave moved closer to the face of the ramp and diverted discharge decreased. Figure 3 shows 234 MGD inflow.

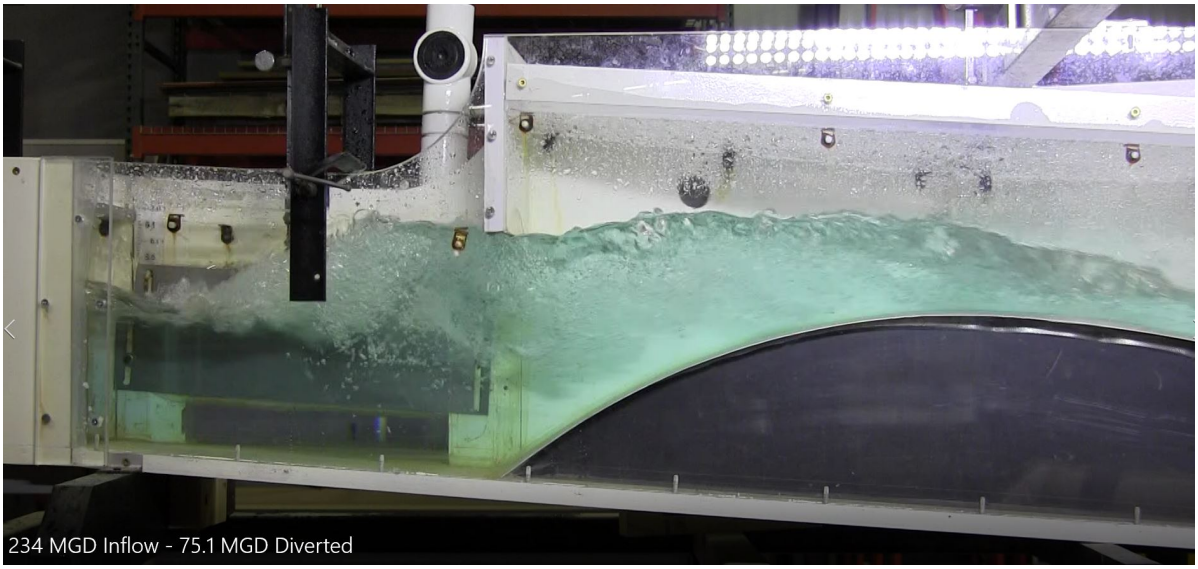

Fig. 3 – Final testing configuration of the regulator chamber – 234 MGD inflow

The hydraulic jump completely swept out at an inflow of approximately 249 MGD and the diverted discharge decreased to 62.8 MGD. Diverted discharges once again increased as inflow continued to increase beyond 249 MGD as the depth of water over the sidewall orifice continued to increase. For testing with inflows up to 425 MGD, the hydraulic jump remained swept out and the regulator chamber adequately passed these inflows without an undesirable hydraulic jump or excessive water depths. The diverted discharge reached 85.1 MGD at 425 MGD inflow. A photo with 425 MGD inflow is shown in Figure 4.

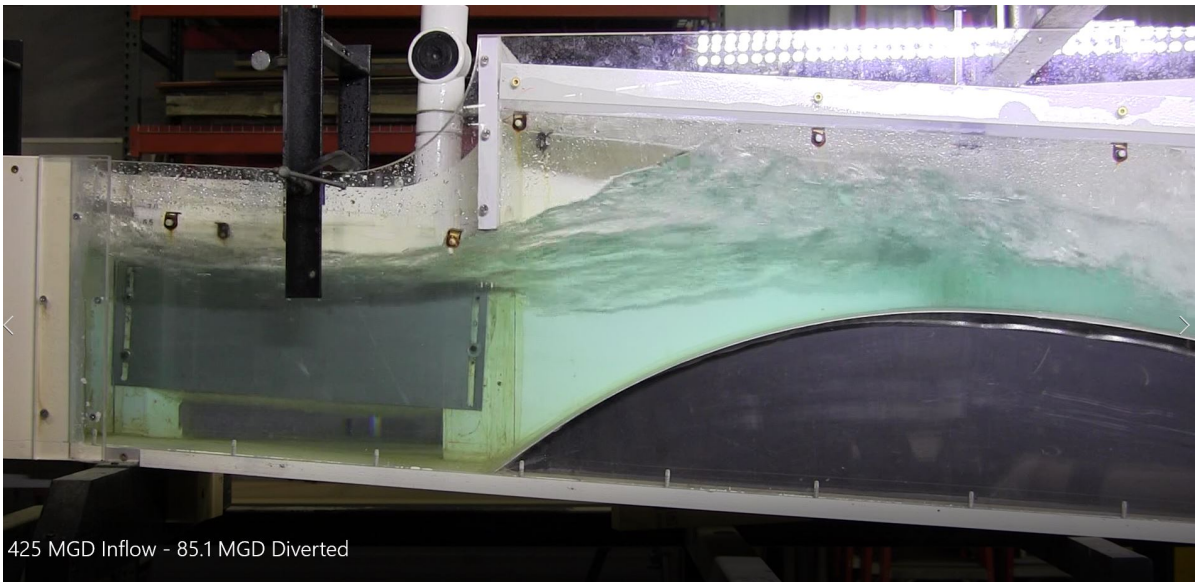

Fig. 4 – Final testing configuration of the regulator chamber – 425 MGD inflow

Table 1 provides a full listing of the final inflows and related diverted discharge values for the regulator chamber testing. These data are plotted in Figure 5.

7th International Junior Researcher and Engineer Workshop on Hydraulic Structures, IJREWHS'19, B. HEINER and B. TULLIS (Eds), Report 2, U.S. Bureau of Reclamation, Denver, CO, USA - ISBN 978-0-578-69809-0
https://doi.org/10.26077/2s9r-ad12

Table 1 – Inflow and related diverted discharges

Ramp height of 5.25-feet, diversion orifice restrictor plate set at 1.5-feet above floor. Phase II conduit added – vented.	
Inflow (MGD)	Diverted Discharge (MGD)
35.1	35.1
50.0	50.0
54.0	54.0
60.0	57.2
108.1	62.8
132.2	70.3
156.3	73.5
187.4	75.1
212.0	76.7
234.0	75.1
246.2	70.3
258.4	65.8
360.0	78.3
425.0	85.1

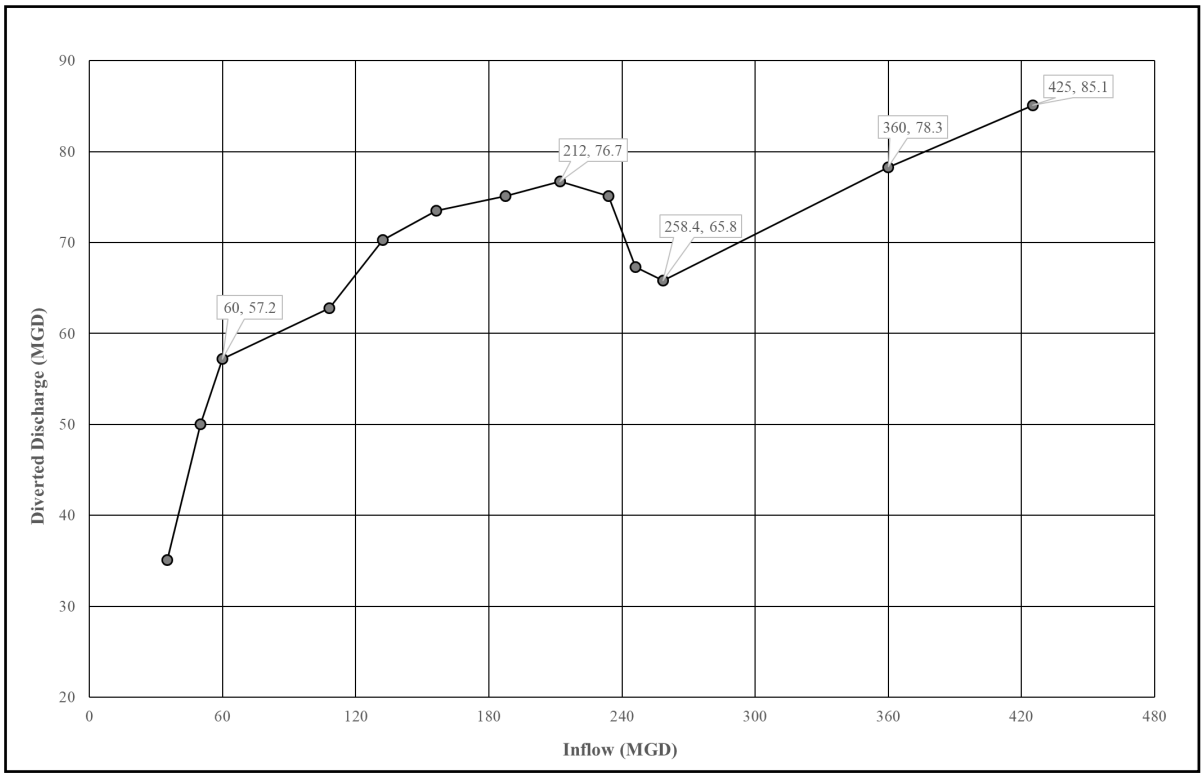

Fig. 5 – Inflow and related diverted discharges

Diversion Conduit Analysis

It was determined that the diversion conduit required venting to maintain free surface flow. Venting

was added to the diversion conduit in the model with options to vent either from the atmosphere near the regulator chamber or from the regulator chamber directly. The pipe used in the model for venting, as well as the hole placed in the regulator chamber wall was 1.5-inches in diameter, or an equivalent of 1-foot diameter at full-scale. Testing showed that both options provided adequate air flow into the diversion conduit to maintain free-surface flow for the full range of inflows/diverted discharges documented for the final testing configuration. Without venting, the diversion conduit filled, resulting in pressurized flow conditions in which diverted discharges increased, exceeding the conduit's capacity. With venting provided, the diversion conduit adequately passed discharges of 0-76.7 MGD for diverted flows generated prior to the hydraulic jump sweeping out (inflow of ~249 MGD). It was observed for diverted discharges of 80 MGD or greater that occurred from pre-hydraulic jump sweep out inflows, the diversion manhole could not adequately pass the flow, causing filling of the pipe section between the manhole and the diversion conduit transition vault. However, the diversion conduit was able to adequately pass the 85.1 MGD diverted discharge that occurred with the 425 MGD inflow (post-hydraulic jump sweep out conditions).

Diverted discharges generated without the orifice restrictor plate exceeded the ability of the diversion conduit to maintain free surface flows for inflows of 108.1 - 156.3 MGD, with splashing out of the top of the diversion manhole for inflows of 132.2 and 156.3 MGD. As the hydraulic jump/standing wave moved closer to the face of the ramp and then swept out, the diverted discharges decreased for inflows of 187.4 - 234 MGD. Diverted discharges increased as inflow increased beyond 234 MGD. A diversion discharge of 119.9 MGD was observed at the model's tail box with an inflow of 360 MGD (25-year inflow); however, the actual diverted discharge was higher, as diverted flow was ejected out of the top of the diversion transition vault and the diversion manhole, indicating the diversion conduit capacity was greatly exceeded. No test was conducted for inflow of 425 MGD without the orifice restrictor plate.

CONCLUSION

Effective diversion of supercritical flows for CSO control has been a challenging hydraulic design issue. Physical model testing demonstrated the novel widening ramp concept proposed for the regulator chamber in Lynchburg, Virginia was applicable and the design dimensions for the regulator chamber were derived through the use of the physical model. The Lynchburg regulator chamber was designed for a site specific range of inflows and allowable diverted discharges. This was also the case for the New South Wales, Australia regulator and likely will be the case for other applications of using the widening ramp concept for diversion of supercritical flows. However, the results of this study establish the potential for the widening ramp structure to be utilized for tackling other supercritical flow diversion problems. Without straightforward design guidelines to follow for future applications, physical modelling will be an advantageous tool to determine design dimensions for the use of the widening ramp for diversion of supercritical flows.

ACKNOWLEDGMENTS

This paper is based on the physical model testing conducted at IIHR – Hydroscience & Engineering located at the University of Iowa under the guidance of Mr. Troy Lyons, Director of Engineering Services. Great appreciation is bestowed to the design team of Greeley & Hansen, Inc., including Dr. Nikos Apsilidis and Mr. Lin Liang for invaluable input during testing and the foresight to identify the concept as a design option, and Mr. James Talian from the City of Lynchburg for important feedback throughout testing and final documentation.

REFERENCES

CHOW, V.T (1959). "Open-Channel Hydraulics." McGraw-Hill, United States. 680 pages.

Environmental Protection Agency (EPA) (2018). National Pollutant Discharge Elimination System (NPDES). "Combined Sewer Overflows." https://www.epa.gov/npdes/combined-sewer-overflows-csos. August 30, 2018.

ETTEMA, R., Chair and Editor, ARNDT, R., ROBERTS, P., WAHL, T. (2000). "Hydraulic Modeling: Concepts and Practice". Task committee on Hydraulic Modeling. Sponsored by the Environmental and Water Resources Institute of the American Society of Civil Engineers. 390 pages.

NOVAK, P., GUINOT, V., JEFFREY, A., REEVE, D. (2010). "Hydraulic Modelling – an Introduction. Principles, Methods, and Applications. Spon Press, United States and England. 599 pages.

VAN DRIE, R.P.J., HERNGREN, L. (2006). "Use of supercritical diversion structure to drive pollution control device. In 7th International Conference on Urban Drainage Modelling and the 4th International Conference on Water Sensitive Urban Design: Book of Proceedings. 313 pages. Monash University.

VAN DRIE, R.P.J., HERNGREN, L. (2007). "Use of supercritical diversion structure to drive pollution control device, Physical Modelling and 2D validation." NOVATECH 2007, Session 6.2. pgs. 1243-1250.

WEBB, C., BARFUSS, S., JOHNSON, M. (2010). "Modelling roughness in scale models." Journal of Hydraulic Research. Volume 28, Issue 2. pgs. 260-264.

7th International Junior Researcher and Engineer Workshop on Hydraulic Structures, IJREWHS'19, B. HEINER and B. TULLIS (Eds), Report 3, U.S. Bureau of Reclamation, Denver, CO, USA - ISBN 978-0-578-69809-0
https://doi.org/10.26077/z99p-xs05

Large-Eddy Simulations of T-shaped open-channel confluences with different downstream channel widths

Pedro Xavier RAMOS
Hydraulics Laboratory, Department of Civil Engineering, Ghent University, Sint-Pietersnieuwstraat 41 B5, Ghent B-9000, Belgium, Email: Pedro.Ramos@UGent.be.
Laurent SCHINDFESSEL
Hydraulics Laboratory, Department of Civil Engineering, Ghent University, Sint-Pietersnieuwstraat 41 B5, Ghent B-9000, Belgium.
João Pedro PÊGO
Faculty of Engineering – University of Porto, Rua do Dr. Roberto Frias, 4200-465 Porto, Portugal.
Tom De MULDER
Hydraulics Laboratory, Department of Civil Engineering, Ghent University, Sint-Pietersnieuwstraat 41 B5, Ghent B-9000, Belgium.

Abstract: Confluences of open-channel flows are common in nature as well as in urban drainage networks and in hydraulic structures. The complex hydrodynamics is often studied in schematized, right-angled confluences. In this paper, the influence of the downstream channel width onto time-averaged and turbulent flow features will be investigated numerically, based on Large-Eddy Simulations. For one flow situation, i.e. flow ratio and downstream Froude number, two geometries will be compared: a discordant width case, which was studied experimentally by Yuan et al. (2016) in a flume with a wider downstream channel than the upstream mean and tributary channels, and the corresponding concordant width case, in which the downstream channel has the same width as the confluent channels. The widening of the downstream channel turns out to reduce the backwater effects, the flow contraction and the associated water surface depression. Moreover, the three-dimensionality of the recirculation zone in the mean flow is enhanced due to complex flow patterns, resulting in a reduced width and length of the recirculation zone in the lowest third of the water column. Finally, the respective cores of high values of the dimensionless TKE and Reynolds shear stress, that persist over the water column, have lower peak values in the discordant width case and the shape of those cores is more distorted, especially near the bed.

Keywords: *open-channel confluence; unequal widths; Large-Eddy Simulation; CFD.*

INTRODUCTION

Confluences of open-channel flows are ubiquitous features in fluvial networks, urban drainage networks and even in hydraulic structures (e.g. outfalls, fish passes). Confluences are important

locations in those networks as they regulate the water levels, the mixing phenomena of the incoming flows and the transport and deposition of sediments, pollutants and nutrients (Best, 1987; Biron et al. 1996; Boyer et al. 2006; Rice et al., 2008; De Serres et al. 1999; Ludeña et al. 2017; Cushman-Roisin and Constantinescu, 2019).

The flow features in the confluence hydrodynamics zone (CHZ) are complex and are often studied in schematized geometries consisting of straight branches and sharp junction corners. Best (1987) developed a conceptual model discerning the features indicated (in planform) in Figure 1: a flow stagnation zone, a flow deflection zone, a flow recirculation zone (RZ), a zone of maximum velocity, a gradual flow recovery area and shear layers. The characteristics of these (three-dimensional) flow features depend, among other factors, upon the confluence angle between the inflowing branches, the ratio of the inflowing momentum fluxes, the tailwater Froude number and the bed elevation discordance (e.g. Đorđević, 2013; Biron et al. 1996; Penna et al. 2018; Birjukova-Canelas et al. 2019).

Among the schematized geometries, the right-angled confluences of a main channel and a tributary channel have been investigated the most extensively. The experimental data of Weber et al. (2001) pertain to lab experiments in such a T-shaped confluence with horizontal and concordant beds (i.e. no bed elevation discordance is present between the main and the tributary channels) and concordant widths (i.e. the post-confluence channel has the same width as the incoming channels). These data have been used frequently for validation of numerical models. By means of validated numerical models, the mean (i.e. time-averaged) and turbulent flow features in the CHZ can then be studied in more detail in similar or variant geometries and flow conditions as were studied experimentally (e.g. Huang et al., 2002; Constantinescu et al. 2001; Yang et al., 2013; Schindfessel et al., 2015; Ramos et al., 2019a,b).

For many years, the study of Weber et al. (2001) was one of the few studies investigating experimentally the flow structure of a T-shaped open-channel confluence. More recently, Yuan et al. (2016) experimentally studied a right-angled open-channel confluence with a wider post-confluence channel and adopting a higher time-resolution of the velocity measurements.

The present paper wants to contribute to assessing the effects of width discordance between the confluent channels on the confluence flow features. To this end, a numerical model based upon Large-Eddy Simulations will be first set up and validated for one of the flow cases investigated experimentally by Yuan et al. (2016) in the confluence with a wider downstream channel, which will be further referred to as the discordant width case. Then, the model will be adapted to simulate the corresponding concordant width case (i.e. the downstream channel will be narrowed to have the same width as the upstream channels).

The effect of width discordance onto the water surface elevations, the three-dimensional

7th International Junior Researcher and Engineer Workshop on Hydraulic Structures, IJREWHS'19, B. HEINER and B. TULLIS (Eds), Report 3, U.S. Bureau of Reclamation, Denver, CO, USA - ISBN 978-0-578-69809-0
https://doi.org/10.26077/z99p-xs05

structure of the recirculation zone and some turbulent flow features will then be assessed.

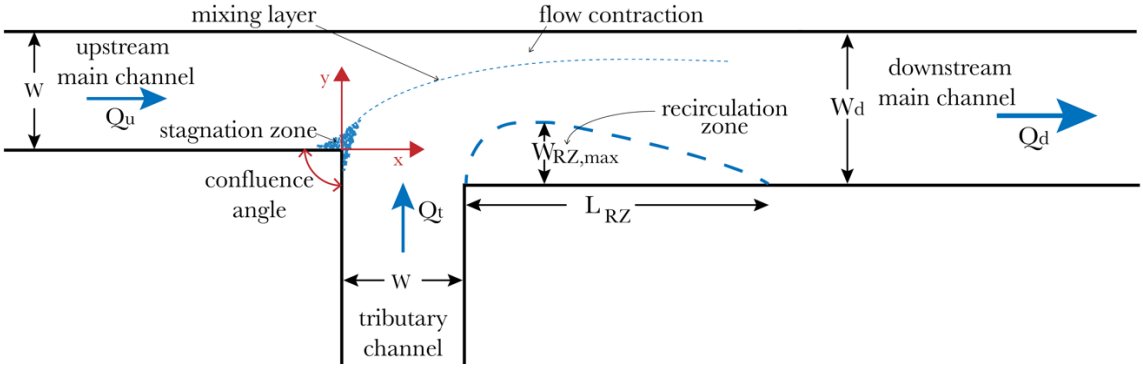

Figure 1. Schematic plan-view of the flow features in a right-angled open-channel confluence with channels of equal width (after Best, 1987) with coordinate system, nomenclature and recirculation zone dimensions at a given elevation z above the bed.

HYDRAULIC CONDITIONS

In this work, a right-angled confluence of open channels with a rectangular cross-section and with horizontal and concordant beds is considered. Let W be the width of the main upstream channel and the tributary channel and W_d the width of the downstream (i.e. post-confluence) channel (Figure 1). Two cases will be studied, having a different width discordance ratio:

$$\omega = {W}/{W_d} \quad (1)$$

The discordant width case (ω=0.75) has a wider downstream channel than the upstream channels (Figure 1) and corresponds to the lab experiment with fixed, horizontal and concordant beds by Yuan et al. (2016), which is referred to in the latter paper as "case two". The associated hydraulic conditions are given in Table 1, in which the discharge ratio is defined as follows:

$$q = {Q_u}/{Q_d} = {Q_u}/{(Q_u + Q_t)} \quad (2)$$

where Q_u and Q_t are the incoming discharge of the main channel and the tributary, respectively, and Q_d is the downstream discharge. The downstream Froude number is given by:

$$Fr_d = {U_d}/{\sqrt{g h_d}} \quad (3)$$

where $U_d=Q_d/(h_d W_d)$ is the cross-sectionally averaged downstream velocity, h_d the downstream flow depth and g the gravitational acceleration.

Table 1. Flow case with discordant width (ω=0.75) experimentally investigated by Yuan et al. (2016)

Q_u [l/s]	**Q_t [l/s]**	**Q_d [l/s]**	**q [-]**	**W** [m]	**W_d** [m]	**ω [-]**	**h_d** [m]	**U_d [m/s]**	**Fr_d [-]**
3.9	6.0	9.9	0.40	0.30	0.40	0.75	0.163	0.152	0.12

The concordant width case (ω=1.00) has a downstream channel width which is identical to the width of the upstream channels. Note that the concordant width case has not been investigated experimentally by Yuan et al. (2016). It will be simulated at the same hydraulic conditions (q, Fr_d) as the discordant width case (ω=0.75). As a consequence, the downstream water depth and cross-sectionally averaged velocity in the concordant width case (Table 2) differ from the discordant width case values (Table 1). Note that for both the discordant and the concordant width case, the origin of the coordinate system (Figure 1) is at the upstream confluence corner (x=0, y=0) and at bed elevation (z=0).

Table 2. Flow case with concordant width (ω=1.00)

Q_u	Q_t	Q_d	q	W	W_d	ω	h_d	U_d	Fr_d
[l/s]	**[l/s]**	**[l/s]**	**[-]**	[m]	[m]	**[-]**	[m]	**[m/s]**	**[-]**
3.9	6.0	9.9	0.40	0.30	0.30	1.00	0.197	0.167	0.12

NUMERICAL METHODOLOGY

Large-Eddy Simulations within the OpenFOAM toolbox

The numerical simulations in the present contribution are conducted within the three-dimensional computational fluid dynamics (CFD) software OpenFOAM, version 5.0. A Large-Eddy Simulation approach is adopted, requiring to solve the spatially-averaged continuity and Navier-Stokes equations, governing an unsteady, incompressible and viscous flow. As a Subgrid Scale Model (SGS), the standard Smagorinsky model is used, with a constant C_s of 0.158. In the OpenFOAM toolbox, the governing equations are discretized using the Finite Volume Method (FVM). The selected discretization schemes are second order accurate in time and space. The discretized equations are coupled and solved using the PISO algorithm.

Boundary conditions

In the present work, a rigid-lid approach is adopted as free surface treatment. This implies that the free surface is replaced by a frictionless and impermeable upper boundary of the computational domain. Ramos et al. (2019a) indicates that the implementation of a flat rigid-lid within the simulation of an open-channel confluence might not be valid close to the contracted section (i.e. adjacent to the recirculation zone) because the flow undergoes an acceleration that causes the water surface to drop substantially. With that in consideration, the present LES (Large-Eddy simulations) are run with a curved rigid-lid, approximating the numerical mesh height to the real flow depth. This curved rigid-lid will be defined by simulating first a flat rigid-lid (at an elevation z_{lid} above the bed) case and then converting the predicted time-averaged pressure field (P) onto the lid into an elevation of a virtual free surface (h), according to Equation (4):

$$h\,(x,y) = z_{lid} + \frac{P(x,y,z_{lid})}{\rho g} \quad (4)$$

Note that the latter equation implicitly assumes the hydrostatic pressure law to hold. On both the flat and the curved rigid-lids, zero shear stress and zero normal velocity conditions are imposed on the lids. The foregoing approach is further explained in Ramos et al. (2019a). In the present study, the low downstream Froude number of Fr_d = 0.12 (Table 1 and Table 2) suggests that the water surface variations are less pronounced as compared to the confluence flow cases studied in Ramos et al. (2019a), in which Fr_d, was 0.37. Nevertheless, the abovementioned methodology will be applied in this paper and only results of curved rigid-lid simulations will be shown.

For each of the two cases, ω=0.75 and ω=1.00, an impression of the adopted curved rigid-lid shape is given in Figure 2, by means of three longitudinal transects along the main and downstream channel.

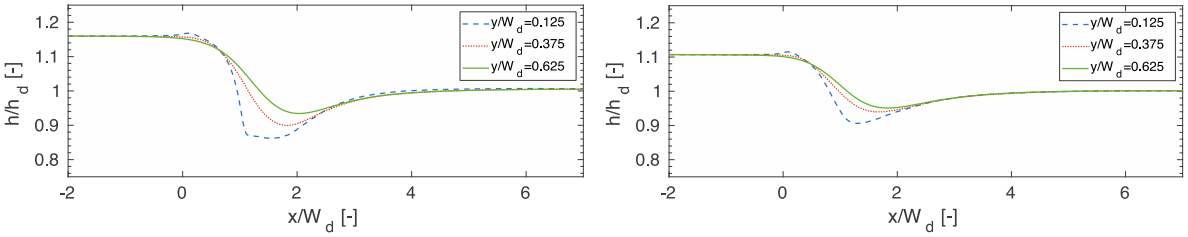

Figure 2. Curved rigid-lid shape indicated by three longitudinal transects along main and downstream channel (left: ω=1.00, right: ω=0.75).

In the present LES simulations, the wall boundary layers will not be fully resolved, with wall functions being adopted instead (see also Schindfessel *et al.*, 2015). This approach requires the first node to be located at z^+≈30−300 (Rodi, Constantinescu and Stoesser, 2013; Schindfessel, 2017).

Since a LES resolves a relatively big part of the turbulence and to approach the model to reality, the inlet velocity should also be turbulent and fully developed. In the present numerical set up, this is achieved by means of a so-called precursor simulation, which basically means that a periodic channel is simulated and its turbulent velocity is used as an inlet condition.

For the pressure variable, a zero value is imposed at the outlet and a zero gradient at the inlets (x/W_d=-5; y/W_d=-5), the walls and the rigid-lid. For the subgrid-scale viscosity a zero gradient is imposed everywhere, except at the walls, where the aforementioned wall model is implemented.

Mesh

A block-structured mesh has been defined for the present numerical investigation (Table 3) after a mesh sensitivity analysis of the results. Grading of the cell size is adopted, yielding a higher resolution in the confluence zone and a smooth transition between the different blocks. The mesh for a flat rigid-lid simulation is deformed for the subsequent curved rigid-lid

simulation, based upon the methodology suggested by Rameshwaran and Naden (2004), and adopted and described in Ramos et al. (2019a): along each vertical grid line (i.e. the z direction), the highest grid point is shifted to coincide with the curved surface defined by Equation (4), whereas the near-wall point is kept in place in order to maintain the dimensionless wall-normal distance, z^+, constant and apply the wall function always under the same circumstances. The grid points in between are gradually redistributed along the vertical gridline (see Figure 4 in Ramos et al., 2019a). Our mesh sensitivity analysis shows that a coarser resolution than adopted in this paper will miss the secondary currents, like it is reported for another open-channel confluence in Ramos et al. (2019a) and in open-channel flows in general by Talebpour and Liu (2019). Therefore, special care was devoted to the mesh independence in terms of secondary flow results.

Table 3. Number of mesh cells for each simulation.

Case	upstream channels	main and tributary		downstream channel			total
	longitudinal (length=5W)	lateral (W=0.30 m)	vertical (h_d=0.18 W)	longitudinal (length=8 W)	lateral (W=0.40 m)	vertical (h_d=0.18 W)	number of cells
ω=0.75	600	100	45	850	120	25	4.2×10^6
ω=1.00					90		3.7×10^6

Model verification

The mesh used in the present paper (Section 3.4) is defined on the basis of a mesh sensitivity and independency analysis, as well as on the validation described in Section 4. Like it was already stated, as a consequence of the use of wall functions, the wall-normal distance of the first grid cells along the sidewalls and the bed should meet the criterion $30<z^+<300$. This condition is met for all the simulations, with z^+ being usually above 30, except for the zones of low flow velocity. These minor exceptions are expected and accepted, especially in the stagnation zone (McSherry et al., 2013; Schindfessel et al., 2015). To obtain the LES results presented in this paper, the simulations have advanced more than 600 seconds, before the data collection started. This initialization time corresponds to 33T (where $T=12W/U_d$ is an approximate flow-through time for the 12W long main channel). Data collection and time-averaging span an additional 75T of simulation (1350 s).

Computational resources

The simulations were computed on a 2×16-core Intel E5-2670 (Sandy Bridge @ 2.6 GHz). The total computational cost of the simulation is approximately 4200 CPU hours. Since the numerical domain is decomposed in 36 sub-domains, the real computational time, due to the parallel processing capabilities, is of 116 hours for each simulation.

RESULTS

Validation of the simulations

Figure 3 depicts the time-averaged horizontal velocity fields near the free surface (red arrows) and near the bed (black arrows) as predicted by the present simulation with discordant widths and as measured by Yuan et al. (2016) in the laboratory. The discrepancies, especially regarding the near bed flow (black arrows), between the LES results and the experiments suggest that the RZ is wider in the simulations. The simulated and measured velocities have the same order of magnitude and, despite the aforementioned discrepancies, the agreement is satisfactory.

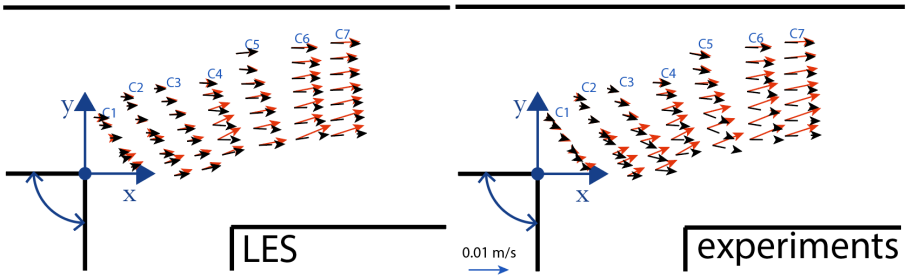

Figure 3. Horizontal velocity fields in the discordant width case (ω=0.75), close to the bed (z/h_d=0.12; black arrows) and close to the free surface (z/h_d=0.8; red arrows), as predicted by the LES simulation (left) and measured by Yuan et al. 2016 (right).

The turbulent kinetic energy (TKE) is shown in Figure 4 for the experiments and in the simulations of the case with ω=0.75. The vertical profiles are located in the cross-sections (C2, C3 and C5) depicted in Figure 3, more specifically in the location where the measured TKE assumes its maximum value in the experimental data of (Yuan et al. 2016). Note that in Figure 3, the vertical coordinate z is non-dimensionalized with respect to the local water depth, h'. The agreement is fair.

Figure 4.b shows the vertical profiles of the measured and simulated Reynolds shear stress ($\overline{u'v'}$) in the same locations as in Figure 4.a. Typically, the higher values occur at about half-depth, both in the experiments and in the simulations. Again, the results suggest a fairly confident validation of the simulations.

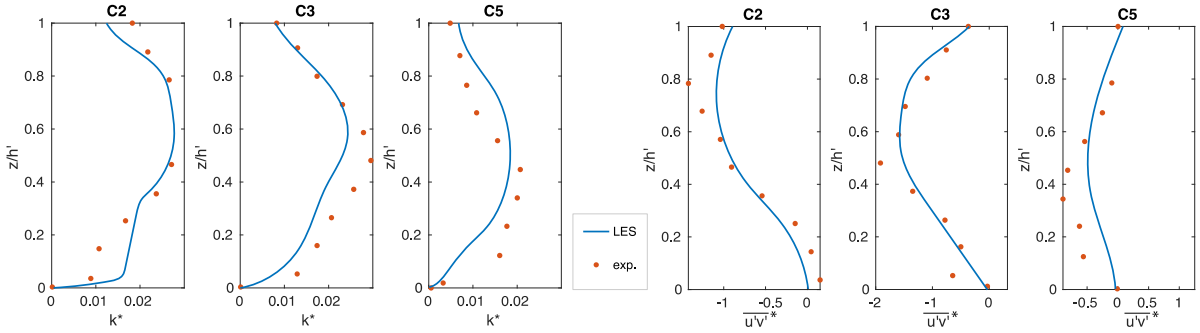

Figure 4. a. (left) Vertical profiles of dimensionless TKE (k*=TKE/U_d^2) in the core of the mixing layer in the discordant width case (ω=0.75); b. (right) Vertical profiles of the dimensionless (with respect to 10^6 x U_d^2) Reynolds shear stress ($\overline{u'v'}$) in the core of the mixing layer in the discordant width case (ω=0.75).

Water surface elevations

In order to assess the influence of the width discordance onto the water surface elevations, the curved rigid-lids (Figure 2) of the discordant and concordant width cases can be compared. It is obvious that the backwater effect is lower in the discordant width case, because of the wider downstream channel. Similarly, the water surface dip in the flow contraction (and recirculation) zone, is less pronounced in the discordant width case.

Mean flow

Based on the time-averaged flow fields, the RZ dimensions (i.e. the maximum width $W_{RZ,\,max}$ and the length L_{RZ}, see Figure 1) are determined by applying the *isovel method* (see e.g. Qing-Yuan et al., 2009; Schindfessel et al., 2015). This means that the RZ boundaries are retrieved from the calculated contourline corresponding to a zero longitudinal velocity component, where its maximum excursion from the downstream channel's inner bank determines $W_{RZ,max}$, while its downstream intersection with the aforementioned bank determines L_{RZ}. Table 4 summarizes the time-averaged dimensions of the RZ in three horizontal planes, with different elevations above the bed, for both the discordant width and the concordant width cases. Note that the predicted near surface (i.e. at z/h_d=0.80) value of $W_{RZ,max}$= 0.27W_d for the discordant width case is slightly larger than the experimental value of $W_{RZ,max}$= 0.23W_d at the water surface (see Fig. 3b in Yuan et al., 2016).

Table 4. RZ dimensions (see Figure 1).

	ω=1.00 (W_d=0.30m; h_d=0.197m)		**ω=0.75 (W_d=0.40m; h_d=0.163m)**	
Location	L_{RZ}	$W_{RZ,max}$	L_{RZ}	$W_{RZ,max}$
z/h_d=0.12	2.50W_d	0.23W_d	1.52W_d	0.13W_d

z/h_d=0.50	$2.49W_d$	$0.24W_d$	$1.76W_d$	$0.27W_d$
z/h_d=0.80	$2.48W_d$	$0.24W_d$	$1.84W_d$	$0.27W_d$

As was already deduced by observation of Figure 3, the RZ dimensions in the discordant width case seem to be substantially smaller near the bed as compared to higher in the water column. Moreover, the near bed value of $W_{RZ,max}$ may even be somewhat smaller than predicted (see section 4.1), which means that the 3D effects in the RZ shape are even more pronounced than the simulations suggest. For the concordant width case, however, Table 4 shows that the simulated RZ dimensions do not change significantly over the flow depth.

As can be seen from the vertical sections near the inner bank of the downstream channel (Figure 5), the differences between the RZ dimensions of the discordant and concordant width cases are related to differences in flow structure. More specifically, a pronounced upwelling flow occurs in the discordant width case (around $x/W_d \approx 1.3$) which results near the bed in a longitudinal extent of the RZ that does not start at the downstream confluence corner. In other words: the total length of the RZ is smaller than the $L_{RZ}=1.52W_d$ value indicated in Table 4 (which represents the distance from the downstream corner to the point where the u=0 isoline reattaches to the wall).

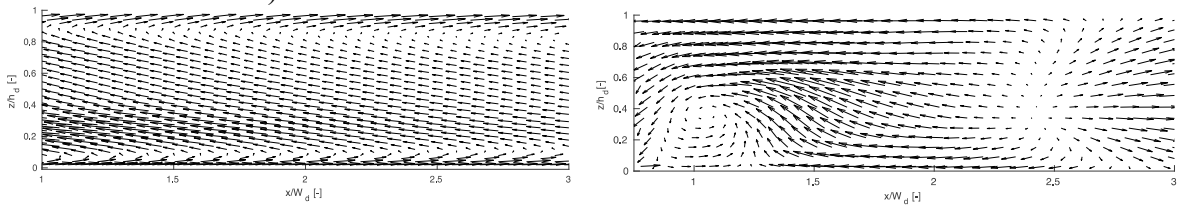

Figure 5. Time-averaged velocity vectors (*u,w*) in a vertical section near the inner bank of the downstream channel (left: section at y/W_d=0.0375 for ω=1.00 case, right: section at y/W_d=-0.2125 for ω=0.75 case).

The top panels of Figure 6 show mean flow streamlines originating from locations at an elevation of z/h_d=0.12 in the upstream main channel. It is clear that the flow contraction is lower in the discordant width case. Similarly, the bottom panels of Figure 6 show mean flow streamlines originating from locations at an elevation of z/h_d=0.12 in the tributary channel, revealing complex flow behaviour. By means of similar streamline plots originating at different elevations above the bed (not shown) it was found that hardly any fluid from the upstream main channel enters the recirculation zone.

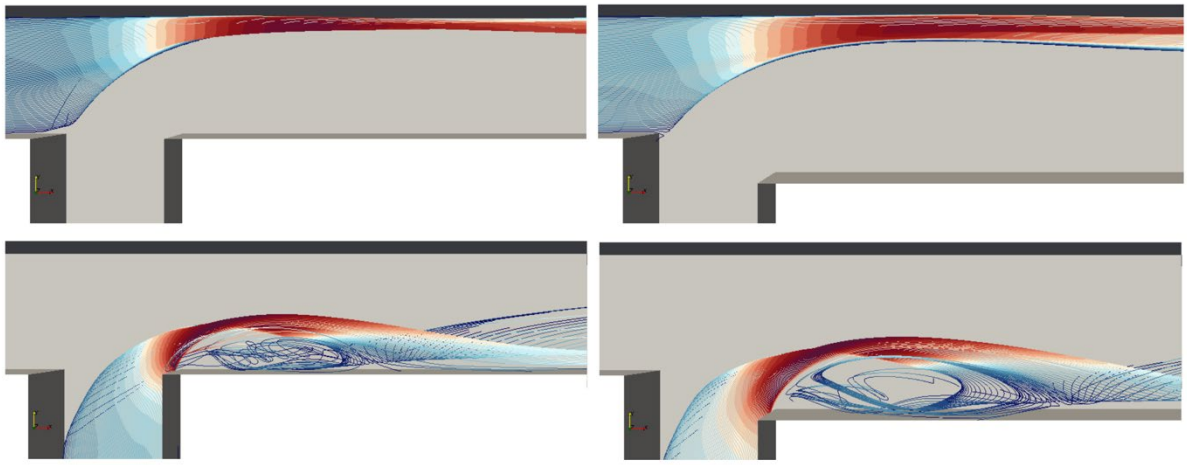

Figure 6. Streamlines of mean flow. Left panels: concordant width case (ω=0.75), right panels: discordant width case (ω=0.75). Top panels: streamlines originating from upstream main channel at an elevation of z/h_d=0.12. Bottom panels: streamlines originating from tributary channel at an elevation of z/h_d=0.12.

Turbulent flow

In Figure 7a, the cross-sectional distribution of the dimensionless TKE and dimensionless Reynolds shear stress ($\overline{u'v'}$), respectively, is presented in three different cross-sections. In every cross-section, a core of higher values persists over the flow depth. Note that the lateral position of those TKE and $\overline{u'v'}$ cores do not coincide.

The concordant width case shows higher values of the dimensionless TKE and $\overline{u'v'}$ (Figure 7b) of the abovementioned cores. The results also show a more pronounced distortion of those cores over the water depth, in the discordant width case. This happens already quite upstream ($1/4<x/W_d<1$). This higher degree of tilting may be linked to the reduced dimensions of the mean flow recirculation zone (RZ) in the near bed zone.

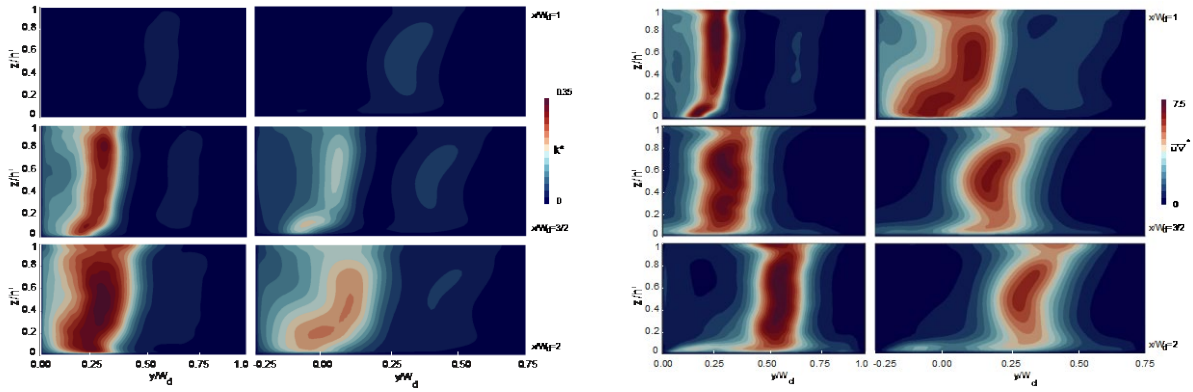

Figure 7. a. (left) Cross-sectional distribution of dimensionless TKE ($k^*=TKE/U_d^2$) for the concordant (ω=1.00, left) and discordant (ω=0.75, right) width cases in three cross-sections (x/W_d=1;3/2;2) of the downstream channel; b. (right) Cross-sectional distribution of dimensionless (with respect to 10^6 x U_d^2) Reynolds shear stress ($\overline{u'v'}$) for the concordant (ω=1.00, left) and discordant (ω=0.75, right) width cases in three cross-sections (x/W_d=1/2;3/2;2) of the downstream channel.

DISCUSSION AND CONCLUSIONS

The effects onto the confluence hydrodynamics of a discordance between the width of the downstream channel and the width of the confluent channels were investigated numerically, for one flow situation (i.e. one flow ratio q and downstream Froude number Fr_d). The widening of the downstream channel was shown to reduce the backwater effects, the flow contraction and the associated water surface depression. Moreover, the width and length of the RZ in the lowest third of the water column were reduced. This seems to be related to a complex mean flow field, including important upwelling motions. To some extent, the foregoing observations are comparable to what was found in confluences with discordant bed elevation, in which the tributary is shallower than the main channel (Biron et al., 1996; Ramos et al., 2019b). In the latter case, however, the RZ was found to be fed by mean flow coming from both the tributary and the upstream main channel (Best and Roy, 1991; Ramos et al., 2019b), whereas in the present case, only the tributary mean flow contributes. With respect to the dimensionless TKE and Reynolds shear stress, the widening of the downstream channel was shown to reduce the peak values in the respective cores of these turbulent quantities. Moreover, the shape of those cores was found to be more distorted, especially in the near bed zone. In future research, it is worth investigating whether the aforementioned observations induce a distortion of the mixing layer between the merging flows, as suggested by Biron et al. (1996) in the context of discordant bed confluences. In addition to this, the possible intermittent and/or periodic character of the flow features discerned in the time-averaged flow (Bradbrook et al., 2000; Parsons, 2003; Yoshimura et al., 2016) should be studied. Finally, the dependency of the effects of width discordance on the flow ratio needs to be investigated. To this end, the developed numerical model for the discordant width flume of Yuan et al. (2016) will be further validated at different flow ratios, based on the experimental data reported in Yuan et al. (2016) and Tang et al. (2018).

ACKNOWLEDGEMENTS

This work was performed using the computational facilities of the HPC infrastructure of Ghent University.

REFERENCES

Best, J. L. and Roy, A. G. (1991). Mixing-layer distortion at the confluence of channels of different depth. Nature, 350(6317), 411. doi.org/10.1038/350411a0.

Best, J.L. (1987). Flow dynamics at river channel confluences: implications for sediment transport and bed morphology. In: Ethridge, F.G. Flores, R.M. Harvey, M.D. (Eds.), Recent developments in

fluvial sedimentology. Spec. Publ. Soc. Sediment. Geol. SEPM 39, 27-35. doi.org/10.2110/pec.87.39.0027.

Birjukova-Canelas, O., Ferreira, R. M., Guillén-Ludeña, S., Alegria, F. C. and Cardoso, A. H. (2019). Three-dimensional flow structure at fixed 70° open-channel confluence with bed discordance. Journal of Hydraulic Research, 1-13. doi.org/10.1080/00221686.2019.1596988

Biron, P., Best, J.L. and Roy, A.G. (1996). Effects of bed discordance on flow dynamics at open channel confluences. Journal of Hydraulic Engineering, ASCE, Vol. 122(12), 676-682. doi.org/10.1061/(ASCE)0733-9429(1996)122:12(676).

Boyer, C., Roy, A. G. and Best, J. L. (2006) Dynamics of a river channel confluence with discordant beds: Flow turbulence, bed load sediment transport and bed morphology. Journal of Geophysical Research: Earth Surface, 111(F4). doi.org/10.1029/2005JF000458.

Bradbrook, K.F., Lane, S.N., Richards, K.S., Biron, P.M. and Roy, A.G. (2000). Large Eddy Simulation of periodic flow characteristics at river channel confluences. Journal of Hydraulic Research, 38(3), 207-215. doi.org/10.1080/00221680009498338.

Constantinescu, G., Miyawaki, S., Rhoads, B., Sukhodolov, A. and Kirkil, G. (2011). Structure of turbulent flow at a river confluence with momentum and velocity ratios close to 1: Insight provided by an eddy-resolving numerical simulation. Water Resources Research, 47(5).

Cushman-Roisin, B. and Constantinescu, G.S. (2019). Dynamical adjustment of two streams past their confluence. Journal of Hydraulic Research, 1-9. doi.org/full/10.1080/00221686.2019.1573765.

De Serres, B., Roy, A. G., Biron, P. M. and Best, J. (1999) Three-dimensional structure of flow at a confluence of river channels with discordant beds. Geomorphology, 26(4), 313-335. doi.org/10.1016/S0169-555X(98)00064-6.

Đorđević, D. (2013) Numerical study of 3D flow at right-angled confluences with and without upstream planform curvature. Journal of Hydroinformatics, 15(4), 1073-1088. doi.org/10.2166/hydro.2012.150.

Yoshimura, H., Fujita, I., Ichiro Moriguchi, R. (2016) Numerical and experimental investigations of unsteady separation zone generated at a right-angled confluence. RiverFlow16, doi.org/10.1201/9781315644479-251.

Huang, J., Weber, L.J. and Lai, Y.G. (2002) Three-dimensional numerical study of flows in open-channel junctions. Journal of Hydraulic Engineering, 128(3), 268-280.

Parsons, D. R. (2003). Discussion of "Three-dimensional numerical study of flows in open-channel junctions" by Jianchun Huang, Larry J. Weber, and Yong G. Lai. Journal of Hydraulic Engineering, 129(10), 822-823.

Penna, N., De Marchis, M., Canelas, O. B., Napoli, E., Cardoso, A. H. and Gaudio, R. (2018) Effect of the junction angle on turbulent flow at a hydraulic confluence. Water 10(4), 469-491.

Qing-Yuan, Y., Xian-Ye, W., Wei-Zhen, L., & Xie-Kang, W. (2009). Experimental study on characteristics of separation zone in confluence zones in rivers. Journal of Hydrologic Engineering, 14(2), 166-171.

Rameshwaran, P. and Naden, P. S. (2004) Three-dimensional modelling of free-surface variation in a meandering channel. Journal of Hydraulic Research, 42, 603–615.

Ramos, P.X., Schindfessel, L., Pêgo, J.P. and De Mulder, T. (2019a) Flat vs. curved rigid-lid LES computations of an open-channel confluence. Journal of Hydroinformatics, 21, no.2: 318-334. doi.org/10.2166/hydro.2019.109

Ramos, P.X., Schindfessel, L., Pêgo, J.P. and De Mulder, T. (2019b) Rigid-lid LES predictions of secondary ow in an open-channel confluence with concordant and discordant beds. 38th IAHR World Congress, Panama.

Rice, S., Roy, A., & Rhoads, B. (2008). River confluences, tributaries and the fluvial network. John Wiley & Sons.

Rodi, W., Constantinescu, G. and Stoesser, T. (2013). Large-eddy simulation in hydraulics. CRC Press.

Schindfessel, L., Creëlle, S. and De Mulder, T. (2015). Flow patterns in an open channel confluence with increasingly dominant tributary inflow. Water, 7(9), 4724-4751. doi.org/10.3390/w7094724.

Tang, H., Zhang, H. and Yuan, S. (2018). Hydrodynamics and contaminant transport on a degraded bed at a 90-degree channel confluence. Environmental Fluid Mechanics, 18(5), 1293-1295. http://dx.doi.org/10.1007/s10652-018-9612-x

Talebpour, M. and Liu, X., 2019. Numerical investigation on the suitability of a fourth-order nonlinear k-ω model for secondary current of second type in open-channels. Journal of Hydraulic Research, 57(1), pp.1-12.

Weber, L. J., Schumate, E. D. and Mawer, N. (2001) Experiments on flow at a 90° open-channel junction. Journal of Hydraulic Engineering, 127(5), 340-350. doi.org/10.1061/(ASCE)0733-9429(2001)127:5(340).

Winant, C. D., and Browand, F. K. (1974). "Vortex pairing: The mechanism of turbulent mixing layer growth at moderate Reynolds number," Journal of Fluid Mechanics, 63, 237-255.

Yang, Q. Y., Liu, T. H., Lu, W. Z. and Wang, X. K. (2013) Numerical simulation of confluence flow in open channel with dynamic meshes techniques. Adv. Mech. Eng., 5, 860431.

Yuan, S., Tang, H., Xiao, Y., Qiu, X., Zhang, H. and Yu, D. (2016) Turbulent flow structure at a 90-degree open channel confluence: accounting for the distortion of the shear layer. Journal of Hydroenvironmental Research, 12, 130-147.

7th International Junior Researcher and Engineer Workshop on Hydraulic Structures, IJREWHS'19, B. HEINER and B. TULLIS (Eds), Report 4, U.S. Bureau of Reclamation, Denver, CO, USA - ISBN 978-0-578-69809-0
https://doi.org/10.26077/rz1a-bh18

SPILLWAY DEBRIS PHYSICAL MODEL STUDY MORNING-GLORY SPILLWAY

Melissa SHINBEIN
TSC- Engineering & Laboratory Services Division, United States Bureau of Reclamation, USA,
mshinbein@usbr.gov

Abstract: In this 1:18 Froude scale physical hydraulic model study, woody debris was introduced into a reservoir upstream of a morning-glory spillway at different flow rates causing jams. The purpose of this study is to ascertain the frequency of woody debris clogs in the crest, mouth, transition, or a combination of the three in the morning-glory spillway over varying flow rates. Because of the random nature of debris loading into reservoirs (flux, density, species, length, diameter, branch complexity, etc.), a variety of woody species were used to represent prototype lengths of 10 feet to 35 feet and diameters of 0.5 feet to 4 feet. Flow rates in prototype ranged from approximately 500 to over 3000 cubic feet per second. Flow rate can also play an integral part in where the jam occurs, especially in the transition from weir to orifice flow into the spillway. As the flow transitions from crest control into full pipe control, the water surface elevation (WSE) becomes high enough that debris does not naturally pass through the spillway. The location of the jam can impact the degree of change in water surface elevation, causing changes of up to 25 feet prototype, or approximately a 780% increase, over the range of flow rates tested.

Keywords: Reservoir Debris, Dam Safety, Morning-Glory Spillway, Change in WSE

INTRODUCTION

The US Bureau of Reclamation (Reclamation) is responsible for over 360 high and significant hazard storage dams and dikes in the western portion of the United States (US Bureau of Reclamation). Debris entering Reclamation's reservoirs can result in clogged spillways, which reduce discharge capacity and create higher water surface elevation/s (WSE) in the reservoir. In the event of dam overtopping due to reduced spillway capacity, risk estimators elicit values for spillway capacity reduction. Prior to this research, there were no studies on the impacts to reservoirs created by debris jams in morning-glory spillway structures.

Literature Review

Morning-glory type spillways were first noted in use around 1896, making this a relatively new spillway type (Bradley, 1952). Morning-glories are typically used on sites with restricted space or where downstream flow from a reservoir needs to be restricted. Currently, morning-glories are less

https://doi.org/10.26077/rz1a-bh18

utilized than other forms of flow control due to concern around air entrainment and flow control. Specifically, while morning-glories are designed to control flow over the crest in weir flow, once the flow regime transitions into orifice control where the crest is submerged, the original discharge curves cannot be interpolated. This would result in two rating curves, one for unsubmerged weir flow and a separate curve for submerged flow, increasing the difficulty of managing the outflow of water (ACOE, 2012). Furthermore, once debris enters the throat of the control structure, it cannot be removed until flow subsides.

To understand the best configuration for utilizing piers or vortex-breakers and maximizing the coefficient of discharge over the crest Musavi-Jahromi, et al. tested 17 configurations by varying the number of vortex-breakers and the angle of the blade. The most efficient configuration was found to be six piers at an angle of 45°, increasing the discharge coefficient by approximately 545%. Furthermore, piers impact the flow at which the transition between weir to orifice flow occurs. Similarly, this hydraulic physical model based on the prototype of Foss dam in Oklahoma has six piers.

Additional literature concerning the relationship between debris loading and WSE can be seen in the previous iteration of the physical hydraulic model utilized in this study. The previous study investigated debris clogging with various openings of a radial gated ogee crest spillway (Walker, 2018). To test clogging caused by woody debris, debris pieces of various sizes were introduced to the ogee crest spillway at varying flow rates. According to this study, the woody debris caused a maximum discharge reduction of 33% with a WSE increase of 4.5 feet prototype for jams that formed under natural processes. Observations of the original tests indicated that jams with higher density are likely to occur because of the restructuring of debris pieces by wind, waves and other surface disturbances in a prototype reservoir. To provide an estimate of the upper range of debris jam impacts, after the original jam was formed, the debris pieces were manually compacted to create a very dense jam. Artificial debris jams were found to have up to a 9 foot change in WSE and a discharge reduction of 48%.

METHODS

A morning-glory spillway, seen in plan view in Figure 1 and profile view in Figure 2, also referred to as a drop inlet or bell-mouth spillway, is an inverted bell-shape that allows surface water to enter the spillway by weir-flow. After flow passes the crest of the morning glory, it then enters the bell-shaped mouth leading into a transition section that allows the flow to converge and is redirected into the conduit that passes through the foundation of the dam. Potential jams may form in the crest, mouth, transition, or any combination of the three. This physical hydraulic model is of Reclamation's Foss Dam in Oklahoma.

https://doi.org/10.26077/rz1a-bh18

Fig. 1 – Morning-glory spillway in 1:18 Froude scale physical model, plan view.

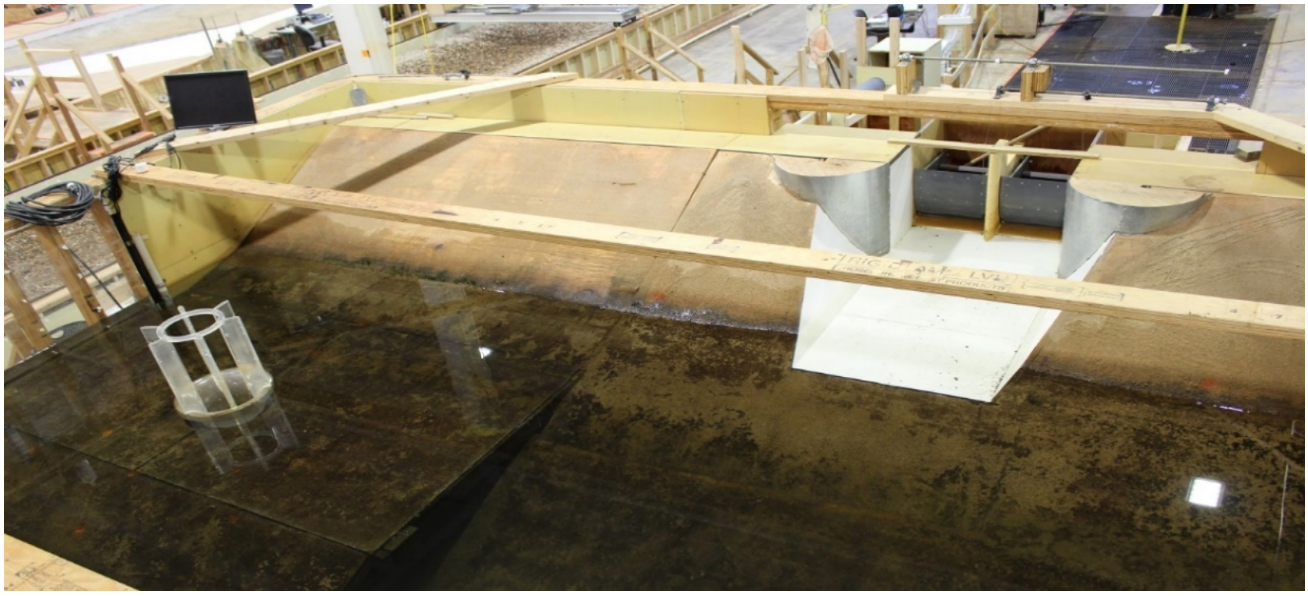

Fig. 2 – Morning-glory spillway in 1:18 Froude scale physical model, profile view.

To allow testing of debris jams with various spillway structures, a 1:18 Froude scale physical hydraulic model was constructed in Reclamation's Denver hydraulics laboratory. This included a 20-ft-wide by 20-ft-long model dimension box and a rock baffle to smooth the incoming from the laboratory pump system. The morning-glory had a model diameter of 1.35ft, with piers of 1.33ft. Model validity was established during clearwater (without debris) testing. The model afforded accurate representations of WSE, flow rates, head loss, velocities, and turbulence in prototype (Hydraulic Lab Techniques, p39). Thus, an increase in WSE caused by debris clogging is relative to the clearwater rating curve.

https://doi.org/10.26077/rz1a-bh18

Debris observed in reservoirs is variable and can include naturally occurring woody species as well as docks, boats, and debris from other structures. Variables for woody species of debris can include, but are not limited to: flux, density, species, length, diameter, and branch complexity. To represent the range of expected flood debris in the physical model, pieces used for modelling included sapling conifer trees, natural sticks, dowel rods, and simulated trees created by placing a rootball on the end of a dowel rod. The range in prototype lengths of debris was 10 to 35 feet while diameters ranged from 0.5 to 4 feet. In all, approximately 300 assorted debris samples were utilized per test.

Tested flow rates for the morning-glory physical model, given in prototype, spanned a range of 500 cubic feet per second (cfs) to 2500cfs for equilibrium tests and up to 3500cfs for the rating curve development. This represents a range of flows from crest control and into pipe control on the morning glory rating curve. Above 2500cfs, the crest of the morning-glory spillway was below the water surface, thus no debris was observed being pulled underwater into the spillway even when debris pieces were fully saturated.

The testing matrix included: generating a rating curve utilizing clearwater (debris-free water) for the morning-glory spillway (Fig. 3), debris loading a minimum of ten tests per flow rate at equilibrium, performing a simulated flood loading with a stepped hydrograph and debris addition, and loading the model with pre-formed clusters. A test for a given flow rate at equilibrium adhered to the following procedure: 1) wait for the clearwater to stabilize, 2) insert the primary log in the transition of the morning-glory spillway, 3) subject the model to randomly dispersed logs, 4) record where the original jam formed, and 5) record WSE and other parameters after the WSE stabilized with the clog.

Fig. 3- Clear water rating curve.

https://doi.org/10.26077/rz1a-bh18

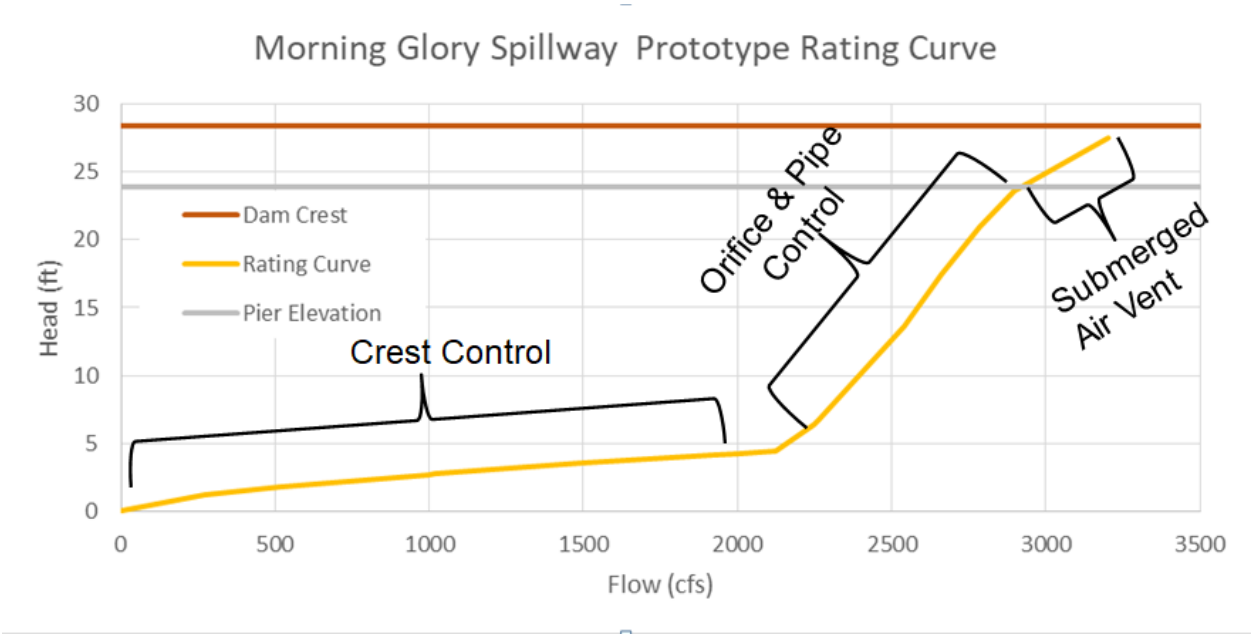

The primary log was a 22 inch long and 3/8th inch diameter dowel that was the only piece of debris designed to be too large to pass through the morning-glory when introduced individually (Fig. 4). The primary log was used to show how jams can recruit and build after a single piece of debris obstructs the passage of water. During a risk assessment, an inventory of the watershed can determine if logs are long enough to jam with the geometry of the existing morning glory. To account for the fact that the primary log ensured a jam formed, pre-constructed jam tests were also run, without the primary log, to ascertain if clogs were as likely to occur within the morning-glory. These pre-constructed jams posed a high risk of being too large to fit through the spillway. Additionally, for all tests random dispersion of the logs entailed individually placing the logs in the model at unsystematic points in an arbitrary sequence.

Fig. 4- Schematic of primary log clogging the transition.

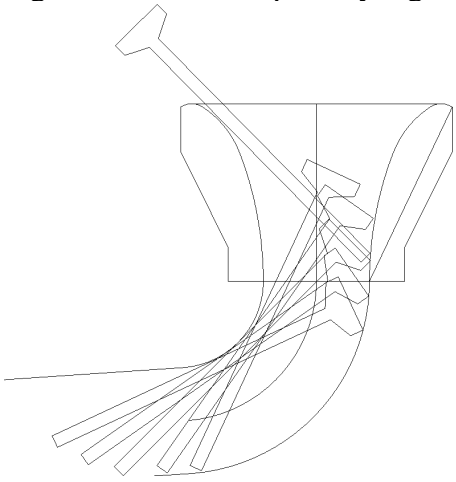

https://doi.org/10.26077/rz1a-bh18

RESULTS

Equilibrium Test

After the introduction of debris into the model, clogs in the morning-glory spillway were grouped into four primary categories: crest, mouth, transition, or a combination of the previous three. Figure 5 exhibits how these jams can potentially obstruct flow, causing an increase in WSE. Since there was a fixed flow rate into the model, the resulting change in WSE post-jam can be used to determine the corresponding flow rate on the rating curve. Then the reduction in discharge can be calculated by comparing the expected flow rate to the calculated flow rate from the rating curve. Therefore, the WSE is inversely related to the discharge capacity. Tests at a given flow rate were repeated approximately ten times or until it became apparent that clogs were occurring at only one location in the morning-glory (i.e.- crest clogs for orifice flow conditions).

Fig. 5 – Photograph of debris jamming in crest, mouth, and transition from left to right images.

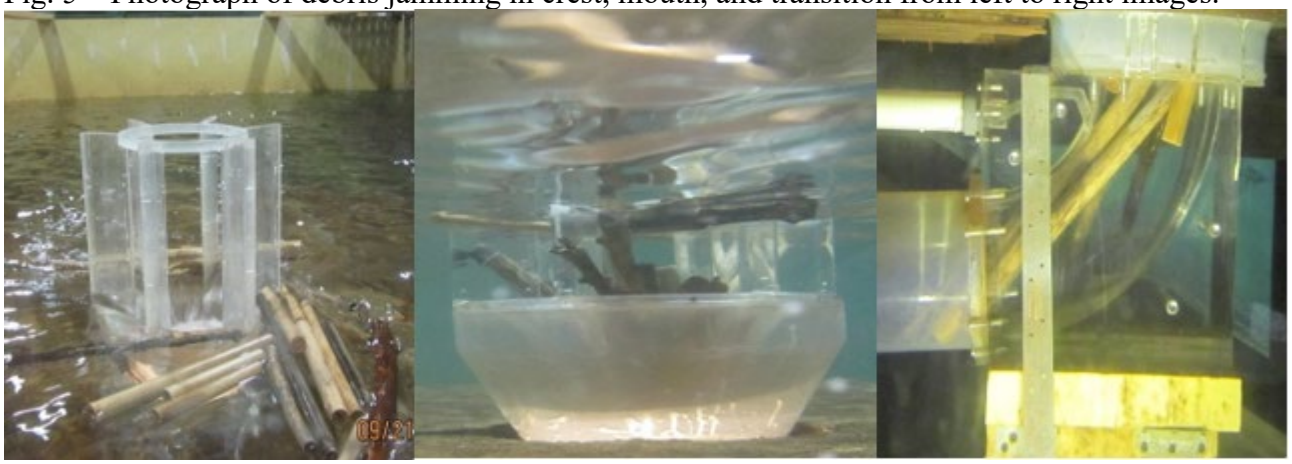

Crest clogs, or jams in the piers, occurred at all flow rates for at least some of the trials and was nearly the exclusive location of jams once the morning-glory spillway entered orifice flow (Table 1). The transition to orifice flow began at approximately 2240cfs and became fully submerged at 2400cfs. Once the flow was in orifice control, the raised WSE resulted in jams having minimal impact on the WSE, if jams would occur at all (Fig. 6). Thus, the increased WSE allowed the debris to float above the morning-glory inlet in the space between the crest without getting pulled down by the water.

When in weir-flow, debris blockages tended to cause a much larger impact on WSE. This is likely because weir-flow is more efficient than orifice flow. This resulted in a larger proportion of clogs occurring in the transition and mouth portion of the morning-glory during weir flow as a higher debris load was approaching the spillway. Conversely, pier jams still occurred during weir-flow, however they were less likely because the velocity vectors diverged around a pier and allowed debris to orient into clear flow unless the debris piece formed a jam between two piers. This high passing efficiency over the morning-glory spillway contributed to the lack of combination jams at the lower flow rates.

https://doi.org/10.26077/rz1a-bh18

Table 1 – Average change in WSE at different jam locations in prototype for equilibrium test. The number below WSE in parenthesis denotes frequency of occurrence.

Flow Rate (cfs)	Crest (ft)	Mouth (ft)	Transition (ft)	Combination (ft)	Total Average (ft)	WSE Change (%)
500	0.954 (2)	1.278 (5)	1.128 (3)	0 (0)	1.168	69.92
1020	1.314 (4)	0 (0)	2.106 (6)	0 (0)	1.789	67.93
1250	1.701 (2)	3.87 (4)	4.5 (2)	0 (0)	3.485	115.93
1510	8.073 (2)	10.666 (6)	0 (0)	3.186 (3)	5.481	162.83
1730	2.617 (5)	13.122 (1)	10.539 (2)	7.488 (2)	5.745	154.19
1910	0.756 (3)	10.692 (2)	15.453 (2)	13.914 (3)	10.816	272.88
2060	5.13 (2)	16.608 (3)	16.44 (3)	18.09 (2)	14.764	356.00
2130	5.814 (3)	17.917 (5)	18.243 (2)	0 (0)	14.286	336.58
2200	1.458 (4)	10.179 (4)	0 (0)	16.443 (2)	6.183	122.20
2240 (Orifice flow)	6.709 (7)	0 (0)	0 (0)	5.667 (3)	6.084	95.48
2270	0.627 (7)	0 (0)	2.277 (2)	2.268 (1)	1.309	19.88
2300	0.237 (5)	0 (0)	0 (0)	0 (0)	0.237	2.86
2500	0.037 (4)	0 (0)	0 (0)	0 (0)	0.0675	0.54
Overall Average	2.774 (45)	6.024 (30)	5.049 (22)	5.229 (16)	5.386	136.71

Fig. 6 - Average change in WSE for all jam locations at varying flows.

https://doi.org/10.26077/rz1a-bh18

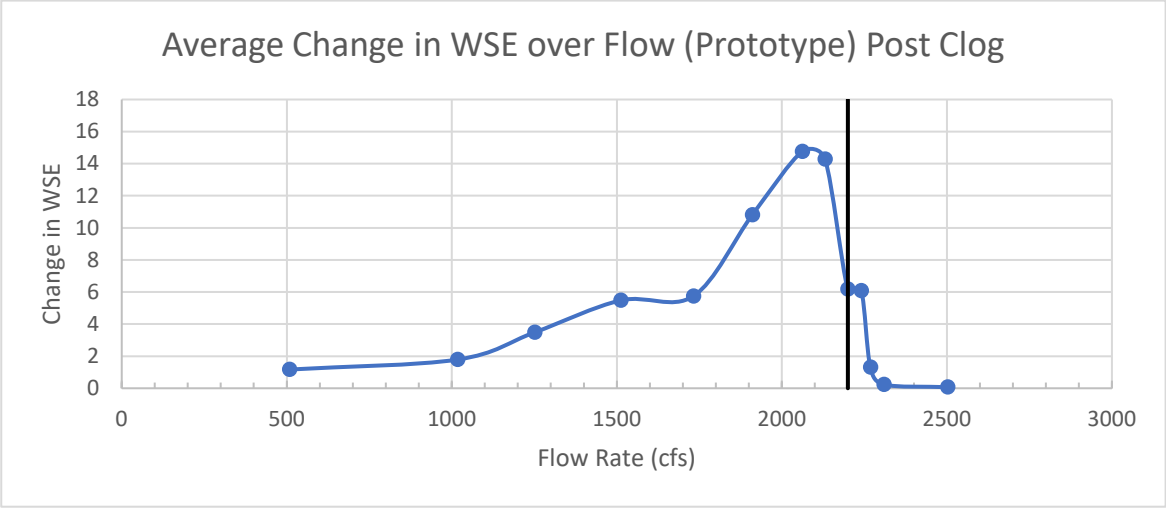

Cluster Test

For the pre-formed cluster tests, nearly all the clusters were broken apart by the piers. Two sets of tests were utilized with pre-formed clusters. During the first test, a pre-formed cluster was introduced into the model and allowed to stabilize to ascertain the final change in WSE (Table 2, Columns 2). Out of the flow rates tested, only two clusters were able to pass the crest and form jams in the mouth or transition, highlighted in red in Table 2. When the pre-formed clusters passed the crest, flow was greatly obstructed resulting in a 200 to 300 percent increase in WSE compared to that of clusters restricted to forming jams in the crest.

The second "rapid" set of tests introduced 20 clusters per flow rate. During this test, clusters were introduced, formed a jam either at the crest, mouth, transition, or a combination of the three, and then removed from the model before being allowed to stabilize (Table 2, Columns 3-4). This test was devised to establish the frequency with which the jams would occur at the aforementioned locations. As observed in the previous pre-formed cluster test, jams were most likely to form around the piers. In both tests, the piers prevented large clusters from entering the spillway in two ways. Predominantly, piers broke apart the clusters on impact, allowing smaller pieces of debris to pass through the mouth and transition without getting lodged. Secondly, the piers restrained the larger clusters from entering the spillway. Therefore, in pre-formed clusters, risk of major changes to WSE is relatively low unless individual pieces of debris that break off from the cluster are longer than the critical dimension of the morning-glory design.

Table 2 – Average change in WSE in Prototype for cluster test. Red font denotes transition jams, black font denotes debris remained in piers.

https://doi.org/10.26077/rz1a-bh18

Flow Rate (cfs)	Average Change (ft)	Number of Jams in the Crest	Number of Jams in the Transition	Percent Change in WSE
(1)	(2)	(3)	(4)	(5)
1020	1.638	20	0	64.54
1374	25.506	19	1	782.87
1910	1.332	20	0	33.94
2130	16.938	19	1	400.43
2200	2.664	20	0	61.41

CONCLUSION AND FUTURE WORK

The purpose of this study was to ascertain the risk debris clogging poses to morning-glory spillways over a range of flow rates. Furthermore, the relationship between the location of the clog and the change to WSE in the reservoir was assessed.

As changes to WSE were greatest for transition jams in pre-clustered tests and mouth jams for equilibrium tests, it can thus be concluded that debris clogs within the mouth or transition area of the morning-glory are the most restrictive to all flow rates. These jams are most likely to occur in peak efficiency of the morning-glory spillway, resulting in the largest change to WSE. Because of the proximity of the mouth and the transition, combination jams are likely to occur at both locations. Therefore, combination jams follow a similar pattern with clogs tending to occur in weir flow. Mouth jams were more likely to occur than transition jams because debris was designed to pass through the transition of the morning-glory when introduced individually. Multiple pieces of debris would need to pass simultaneously to cause a transition jam.

Current analysis suggests morning-glory spillways with piers were able to divide pre-formed clusters or prevent larger debris from entering the mouth or transition. If the jam can remain confined to the crest, this can greatly limit impacts to WSE. This is especially vital in weir-flow conditions where higher velocities will carry the debris into the mouth or transition of the morning-glory. Once the spillway enters orifice flow, debris is not as capable of entering the spillway due to the buoyancy of the debris pieces combined with higher WSE resisting the downpull of the flow velocity entering the morning glory spillway.

https://doi.org/10.26077/rz1a-bh18

As every flow rate tested exhibited at least one pier jam, future testing will entail removing the piers surrounding the morning-glory and monitoring if the clogs occur in different locations at the same flow rates under regular and pre-formed cluster conditions.

ACKNOWLEDGMENTS

This paper wishes to acknowledge Kent Walker, who originally designed and began implementation of testing.

REFERENCES

Army Corps of Engineers with U.S. Bureau of Reclamation. "Best Practices and Risk Methodology: Chapter 31. Drum Gates and Other Gates". 9 Oct. 2012, https://www.usbr.gov/ssle/damsafety/risk/methodology.html

Bradley, JN. "Prototype Behavior of Morning-Glory Shaft Spillways." Summer Convention, ASCE .Denver, USA, June 1952.

Musavi-Jahromi, Seyed Habib, et al. "Discharge Coefficient in the Morning Glory Spillways Due to Longitudinal Angles of Vortex Breakers." Bulletin of Environment, Pharmacology and Life Sciences, vol. 5, Apr. 2016, pp. 34–41., http://www.bepls.com.

U.S. Bureau of Reclamation. "Security, Safety and Law Enforcement Office - Dam Safety." Dam Safety Office- Security, Safety and Law Enforcement Office, Bureau of Reclamation, US Bureau of Reclamation, 15 Feb. 2017, www.Reclamation.gov/ssle/damsafety/risk/index.html.

U.S. Department of the Interior, Bureau of Reclamation. Hydraulic Laboratory Techniques. United States Government Printing Office, 1980.

Walker, Kent (2018). "Spillway Debris Physical Model Study. First configuration, radial gated ogee crest spillway structure." *Dam Safety Technology Development Program*, Denver, USA, July, 50 pages.

7th International Junior Researcher and Engineer Workshop on Hydraulic Structures, IJREWHS'19, B. HEINER and B. TULLIS (Eds), Report 5, U.S. Bureau of Reclamation, Denver, CO, USA - ISBN 978-0-578-69809-0
https://doi.org/10.26077/w24f-0c17

STREAMFLOW REGIME CHANGE IN THE DELAWARE RIVER BASIN

Travis SHOEMAKER
Schnabel Engineering, USA, tshoemaker@schnabel-eng.com
Madhav BISTA
M.Sc. Environmental Technology & Engineering, IHE Delft Institute for Water Education, Netherlands, madhavbista.1@gmail.com
David BRANDES, PhD
Lafayette College, Civil and Environmental Engineering Dept., USA

Abstract: The combined impacts of hydroclimatic change and land development are widely expected to increase the frequency and magnitude of flooding in the northeast United States, with potential implications to floodplain infrastructure and mapping, hydraulic structures, land management, and flood losses. Additionally, shifting flow regimes pose a challenge for engineers and regulators of stormwater management, dams, and levees because design storms are commonly based on historical data, with the stationarity assumption that the future flow regime will mimic the past. Here, we examine selected long-term (40 to 114 years of data) streamflow records from watersheds of varying size in the upper Delaware River basin to assess changes in streamflow regimes. A structural breakpoint analysis of the streamflow records indicated a break in time-series around the year 2000. Hypothesis testing comparing pre- and post-2000 streamflow metrics (annual peak, median, and 7-day low flows) confirmed a statistically significant shift around the year 2000. For example, median flows across the two time periods were statistically different with over 90% confidence for 14 of 28 gauges considered.

Keywords: Delaware River Basin, streamflow, regime change, hypothesis testing

INTRODUCTION

The combined impacts of hydroclimatic change and land development are widely expected to increase the frequency and magnitude of flooding in the northeast United States, with potential implications to floodplain infrastructure and mapping, hydraulic structures, land management, and flood losses (ASCE, 2015; USGCRP, 2014; EASTERLING et al., 2017). Additionally, shifting flow regimes pose a challenge for engineers and regulators of stormwater management, wastewater management, dams, and levees because design storms are commonly based on historical data. For example, NOAA Atlas 14 precipitation volumes, which are frequently used for peak flow design of storm-water management and dam and levees, are based on a stationary annual maximum series, assuming historical data represent present and future conditions. Additionally, low flows statistical methods, such as the Q7-10 statistic which is commonly used for wastewater effluent regulation, also assumes stationarity, or

"the idea that natural systems fluctuate within an unchanging envelope of variability" (MILLY et al., 2008).

With these approaches to water resources engineering and infrastructure management, uncertainty in hydrologic and hydraulic modelling decreases as time progresses because more observations are made each year. However, there have been numerous studies indicating that changes in land use and climate may invalidate the stationarity assumption for practical purposes. For example, MILLY et al. (2008) and WAGENER et al. (2010) assert that water-resource risk assessment and planning can no longer entertain stationarity as a default assumption because of anthropogenic disturbances in a river basin. IPPC (2007) and LALL et al. (2018) indicate that anthropogenic climate change alters means and extremes of precipitation, evapotranspiration, and rates of river discharges that should be taken into account to examine frequency of floods. Hence, models need to incorporate anticipated changes in flood risk due to both watershed change (e.g., land-use) and climate change (STEDINGER and GRIFFIS, 2011).

Here, we provide an assessment of streamflow regime change by examining selected long-term streamflow records from watersheds of varying size in the upper Delaware River Basin. This basin was selected as it is close to the urban centers of the northeast and has reportedly experienced an increase in precipitation over the past 60 years which may result in a corresponding increase in streamflow (USGCRP, 2009; KUNKEL et al., 2013; USGCRP, 2014). This study uses the most recent published streamflow datasets. Unlike land use change mapping and rain gauge data, stream gauge data directly considers the primary design, management, and regulation criteria: flow. Additionally, the streamflow gauges studied here are generally more spatially distributed and represent a longer history than land use maps and rain gauges. The assessment of streamflow regime change provided here will (1) statistically assess stream flow regime change in the upper Delaware Watershed and (2) stand as a case study of the validity of the stationarity assumption.

METHODOLOGY

This assessment of the probability of streamflow change in the upper Delaware River Basin involved the following steps:

- Select long term stream gauges
- Calculate annual statistics for each gauge
- Perform structural breakpoint analyses in time-series for each gauge
- Perform hypothesis testing for average flow change in pre- and post-breakpoint datasets

Each step of the process is explained in greater detail below.

Selection of stream gauges

Stream gauges were selected to (1) obtain full spatial coverage of the river basin, (2) obtain long continuous temporal coverage, (3) exclude the impacts of flow regulation, and (4) include sub-basins

undergoing urbanization. Although the specific numerical selection for some criteria, such as 10-km outside of the watershed, were chosen arbitrarily, all criteria were applied uniformly to all gauges. The following list of criteria was used for selecting stream gauges:

- Minimum of 40 years of data
- No data gaps greater than 1 year
- Gauge in operation until 2016 or later
- Within a 10-km buffer of the upper watershed
- Not more than 50 missing days of data per year used in the analysis
- Hydrologic Disturbance Index not greater than 20
- Density of major upstream dams not greater than 1.2 per 100 km^2

For this work, the upper Delaware watershed has been defined as the basin contributing to the Delaware River at Riegelsville, Pennsylvania. Riegelsville was chosen as the cut off between the upper and lower watershed as a balance between including major upstream tributaries, such as the confluence of the Lehigh and Delaware rivers 7-miles upstream of Riegelsville, and excluding the tidal effects of the Delaware Bay which extend to Trenton, New Jersey, approximately 35 miles downstream of Riegelsville. The watershed was delineated using USGS's StreamStats (Ver 3) application and was cross checked against an ArcMap produced delineation using 30-meter USGS quadrangle digital elevation models (DEMs). A 10-km buffer around the upper watershed was taken as the study bounds. This definition allows for inclusion of additional gauges in the most upper sub-basins of bordering watersheds, which may have similar hydrologic properties to the Delaware Watershed.

A key limitation of stream gauge data when studying hydroclimatic change and land development effects is the effect of direct streamflow regulation. This includes releases, diversions, and storages from dams, levees, mining operations, power plants, water treatment plants, wastewater treatment plants, etc. Therefore, limits on Hydrologic Disturbance Index (HDI) as defined by FALCONE et al. (2010) and density of major upstream dams have been set. The upper Delaware Watershed is an opportune basin to perform this study because the Delaware River is the longest free-flowing river in the Eastern United States; however, it must be recognized that there is some level of flow regulation within the watershed.

Figure 1 provides a map of the total 28 selected stream gauges, the study limits, and relevant dams. Table 1 provides a list of the selected gauges with relevant watershed data. For the selected gauges, the average HDI and density of major upstream dams were 14 and 0.1 per 100 km^2. The watershed area ranged from 29 km^2 to 850 km^2 with an average of 250 km^2.

7th International Junior Researcher and Engineer Workshop on Hydraulic Structures, IJREWHS'19, B. HEINER and B. TULLIS (Eds), Report 5, U.S. Bureau of Reclamation, Denver, CO, USA - ISBN 978-0-578-69809-0
https://doi.org/10.26077/w24f-0c17

Fig. 1 – Map of Selected Gauges

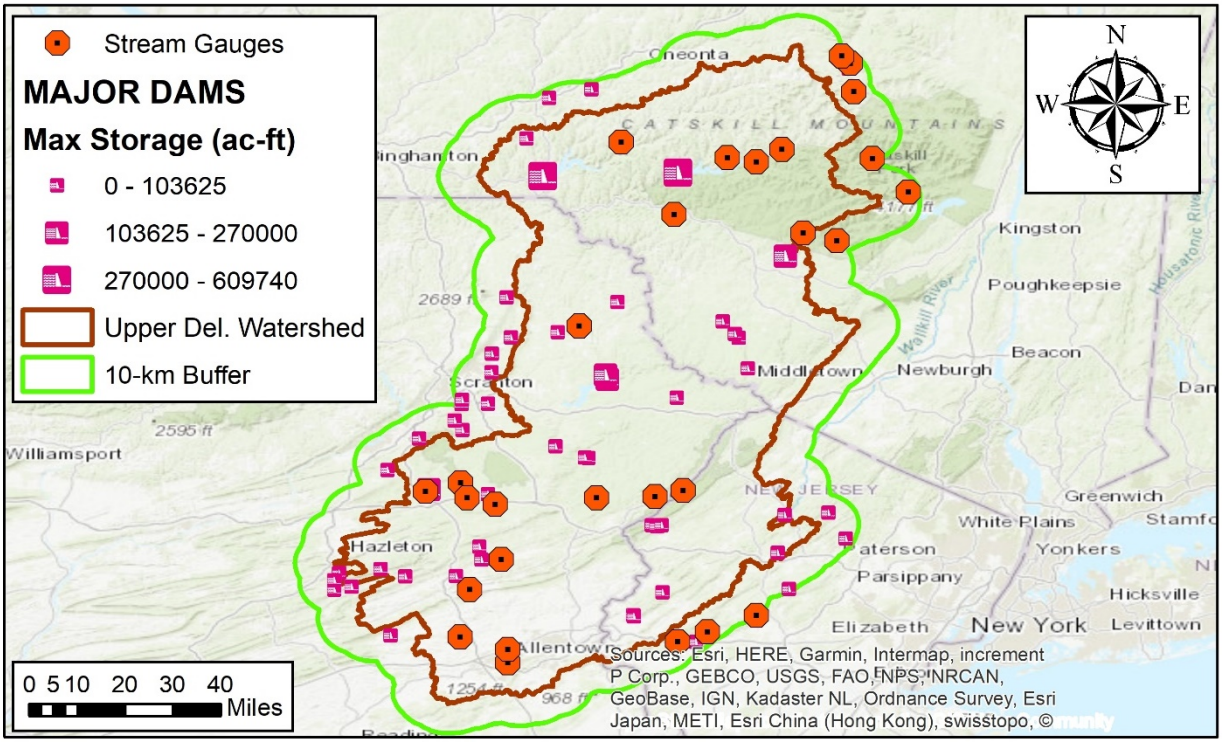

Table 1 – Selected Gauges and Relevant Watershed Data

Station ID	Station Name	Watershed Area (km^2)	Hydrologic Disturbance Index (HDI)	Major Dam Density (Number per 100 km^2)	Starting Water Year	Ending Water Year	Watershed 2006 % Impervious
01350000	Schoharie Creek At Prattsville, NY	613	17	0.49	1904	2017	0.3%
01350120	Platter Kill At Gilboa, NY	29	12	0.00	1976	2016	0.3%
01350140	Mine Kill Near North Blenheim, NY	44	15	0.00	1976	2017	0.2%
01362200	Esopus Creek At Allaben, NY	169	15	0.00	1964	2016	0.2%
01362500	Esopus Creek At Coldbrook, NY	493	13	0.00	1932	2017	0.2%
01365000	Rondout Creek Near Lowes Corners, NY	100	8	0.00	1938	2016	0.0%
01396500	South Branch Raritan River Near High Bridge, NJ	163	15	0.00	1919	2017	3.2%
01396660	Mulhockaway Creek At Van Syckel, NJ	30	14	0.00	1978	2017	2.7%
01399500	Lamington (Black) River Near Pottersville, NJ	83	17	0.00	1922	2017	4.1%
01413500	East Br Delaware R At Margaretville, NY	424	11	0.00	1938	2017	0.2%
01414500	Mill Brook Near Dunraven, NY	64	9	0.00	1938	2017	0.0%
01415000	Tremper Kill Near Andes, NY	86	15	0.00	1938	2017	0.2%
01420500	Beaver Kill At Cooks Falls, NY	627	19	0.00	1914	2016	0.2%
01423000	West Branch Delaware River At Walton, NY	860	16	0.00	1951	2017	0.4%
01429500	Dyberry Creek Near Honesdale, PA	167	17	0.60	1944	2017	0.3%
01435000	Neversink River Near Claryville, NY	172	13	0.00	1939	2016	0.0%
01439500	Bush Kill At Shoemakers, PA	306	9	0.00	1909	2017	0.3%
01440000	Flat Brook Near Flatbrookville, NJ	168	11	0.00	1924	2017	0.2%
01440400	Brodhead Creek Near Analomink, PA	175	17	1.14	1958	2017	0.4%
01447500	Lehigh River At Stoddartsville, PA	240	13	0.00	1944	2017	0.5%
01447680	Tunkhannock Creek Near Long Pond, PA	52	9	0.00	1966	2017	0.6%
01447720	Tobyhanna Creek Near Blakeslee, PA	308	18	0.32	1962	2017	1.9%
01447800	Lehigh R Bl Francis E Walter Res Nr White Haven, PA	753	18	0.27	1958	2017	1.0%
01449360	Pohopoco Creek At Kresgeville, PA	129	14	0.00	1967	2017	2.5%
01450500	Aquashicola Creek At Palmerton, PA	198	20	0.00	1940	2017	1.7%
01451500	Little Lehigh Creek Near Allentown, PA	212	15	0.00	1946	2017	10.1%
01451800	Jordan Creek Near Schnecksville, PA	136	14	0.00	1967	2017	1.7%
01452000	Jordan Creek At Allentown, PA	197	20	0.00	1945	2017	3.8%

Calculate annual statistics

Peak annual, median annual, and 7-day low annual flows were selected to represent the entire streamflow regime: high to low flows. Median and 7-day low flows were calculated from USGS historical surface water daily reported flows. 7-day low flow was defined as the lowest average flow in a 7-day period for a given water year. Daily data disrupted by ice flows were excluded from the analysis and included in the missing days requirement. Peak annual flows were taken directly from the USGS database and represent the maximum flow recorded for each water year.

Structural breakpoint analysis

The statistical programming and computing language R (Version 3.4.1) and the package "strucchange" were used to perform Bai-Perron (BP) tests to detect structural breaks and choose a particular year in a time-series to allow for the comparison of pre and post breakpoint flow statistics. For each gauge, all flow types (7-day low, median, peak) were analyzed individually as well as combined. As criteria for performing BP tests, the following two main assumptions about time-series were made:

1. Independent and identically distributed data: Because the time-series is composed of annual flow data, we can assume non-dependence and same probability distribution of the values.

2. No serial autocorrelation between the data: This was validated by flow-time plots for each time-series.

A BP test is comprised of two separate and independent parts. First, it sequentially locates breaks (one, two, and so on) in a time-series, regardless of statistical significance, based on the minimization of sum of square residuals (SSR) corresponding to the breaks. Second, it tests the significance of the existence of the identified breaks by the comparison (e.g., F-test) of SSR (BAI and PERRON, 1998; ANTOSHIN et al., 2008). For the purpose of this study, the second part was ignored. The BP tests were performed only to provide a mathematical rationale for choosing a certain break year. Even though breakpoints were highly significant (>95% confidence) in case of some gauges, the significance of a particular (break) year in general was not considered as important as the idea that streamflow change may have possibly occurred somewhere around that year. It is for this reason and for the practical purpose that gauges with breaks within +/- 5 years were assigned the same breakpoint. For example, the year 2000 was assigned to a gauge with a breakpoint belonging to the set (1995, 1996, …, 2005). Based on the greatest frequency across the gauges, the year 2000 was determined to be the most likely major breakpoint followed by 1970. Table 2 shows the frequency of the breakpoints. Figure 2 shows the R plots to illustrate the individual-flow (gauge 01362200) and combined-flow (gauge 01447800) analyses.

7th International Junior Researcher and Engineer Workshop on Hydraulic Structures, IJREWHS'19, B. HEINER and B. TULLIS (Eds), Report 5, U.S. Bureau of Reclamation, Denver, CO, USA - ISBN 978-0-578-69809-0
https://doi.org/10.26077/w24f-0c17

Table 2 – Breakpoint frequency

Flow statistics	No. of gauges with breakpoint	
	Year 2000	Year 1970
7-day low	20	16
Median	19	21
Peak	16	11
All three together	22	16

Fig. 2 - (a) Plot of 7-day low flow against time for the gauge 01362200. The BP test shows 1999 as a breakpoint with 95% confidence interval (1981, 2008). (b) Combined plot of 7-day low, median, and peak flow against time for the gauge 01447800. The BP test shows 2002 as a breakpoint with 95% confidence interval (1969, 2008).

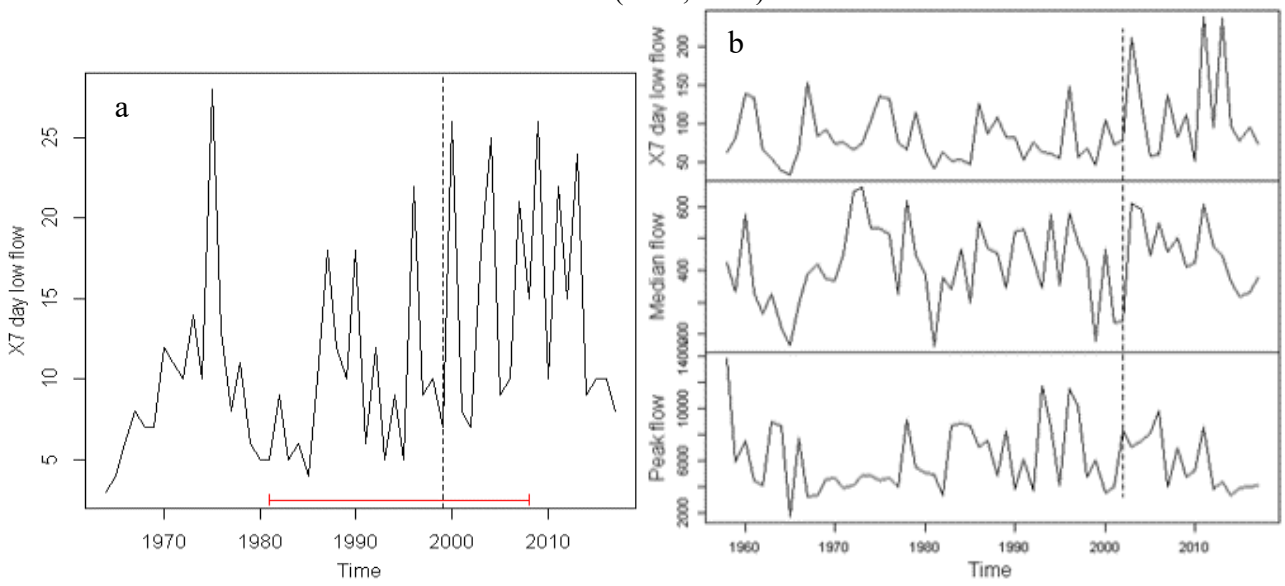

For all the gauges in the basin, the breakpoint 2000 was chosen for further streamflow analysis because: (1) 2000 was the most frequent breakpoint across the gauges, and (2) although 1970 was also frequent, it was the secondary break which showed up together with 2000 for most of the gauges. Figure 3 shows a histogram showing the frequency of first and secondary breaks for all gauges.

Fig. 3 – Histogram of First and Secondary BP Breakpoints

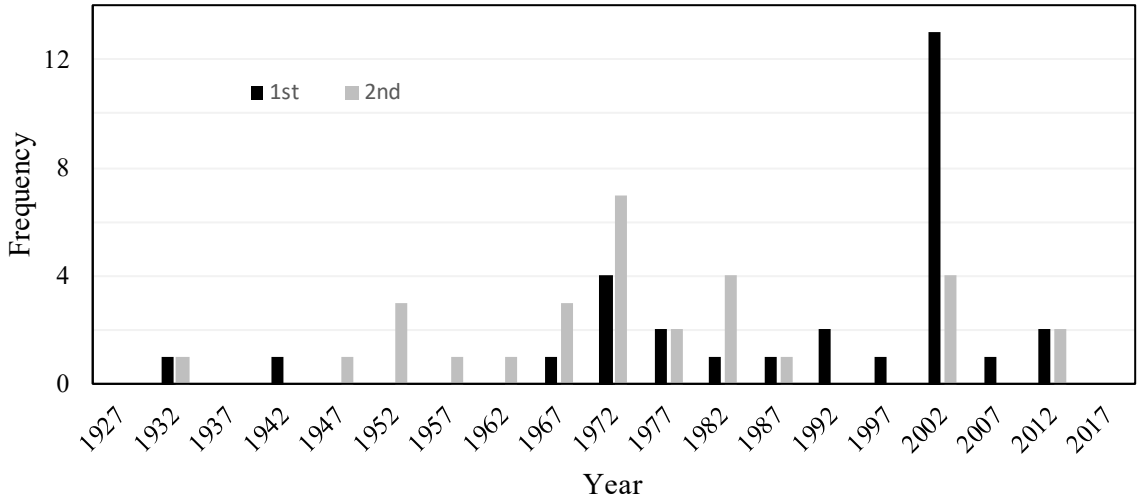

Hypothesis testing

The BP test shows breaks in a time-series based on analysis of structure and distribution of data. However, it does not conjecture on factors such as nature of the data before and after a break. Hence, hypothesis testing was done to evaluate if the change in average of the annual statistics occurred significantly before and after the breakpoint. For each time-series (for all 28 gauges), null and alternative hypotheses were formulated as follows:

Null hypothesis (H0): $\bar{X}1 - \bar{X}2 = 0$

Alternate hypothesis (HA): $\bar{X}1 - \bar{X}2 \neq 0$

where $\bar{X}1$ and $\bar{X}2$ are the average pre and post breakpoint year 2000 streamflow (cfs).

RESULTS

The results of the hypothesis testing indicate statistical change for low and median flows for many gauges. However, no stream gauges exhibited significant (95% confidence) change in peak flow. This may be attributed to two phenomena: (1) flow regulation from dams has prevented any significant change in peak flow, or (2) peak flows have high variability such that an assessment of change with statistical significance is not feasible. The authors have not attempted to quantify the impact of these two phenomena. The results of hypothesis testing are shown in Table 3.

Low frequency events, such as the 100-yr flood and Q7-10, guide the majority of decisions for water resource infrastructure design, management, and regulation. To put the results of this study into the context of water resource practice, estimates of Q7-10, 5-yr, and 25-yr flows have been calculated using the Log-Pearson III distribution with station skew and no outlier adjustment. Changes in these flows in addition to the 7-day low, median and peak flows are summarized in Table 4.

Table 3 - Summary of hypothesis testing results showing the number of gauges (out of 28) with streamflow change about the breakpoint year 2000

Flow statistics	No. of gauges with average streamflow change	
	95% confidence	90% confidence

Average 7-day low	14	16
Average Median	11	14
Average Peak	0	2

Table 4 - Changes in common statistics before and after the breakpoint year 2000

Flow statistics	No. of gauges with flow increase after 2000	Max flow increase	Max flow decrease	Average flow change
Average 7-day low	24	+109%	-18%	+33%
Average Median	24	+35%	-7%	+15%
Average peak	21	+61%	-29%	+12%
Q7-10	23	+216%	-23%	+32%
5-yr flow	22	+69%	-26%	+16%
25-yr flow	22	+133%	-55%	+28%

DISCUSSION AND CONCLUSIONS

Results of the hypothesis testing comparing streamflow before and after the year 2000 breakpoint indicated that statistically significant streamflow change has occurred for low flow and median flow for the majority of the selected gauges. However, peak flows did not exhibit statistically significant change. Changes in the average median streamflows range from 35% increase to 7% decrease. Although the changes varied significantly from gauge to gauge for each statistic, the majority of gauges exhibited an increase in flow, which aligns with past observations that this geographic area has experienced an increase in precipitation over the past 60 years (USGCRP, 2009; KUNKEL et al., 2013; USGCRP, 2014, EASTERLING et al., 2017). The Catskill Mountain (see Fig. 1) region's land use and development is strictly regulated, and this region has exhibited streamflow regime trends consistent with the rest of the study area. Additionally, changes in observed median streamflows were not correlated to watershed imperviousness. Consequently, the authors believe that the streamflow regime change is not solely a result of land use change; however, no attempt has been made to decouple the effects of hydroclimatic change (precipitation/evapotranspiration) and land use, and therefore, the authors recommend further research in this topic.

Results indicating statistically significant change pose a challenge to traditional engineering and management practice, which assumes a stationary streamflow regime. Engineers, operators, and regulators of water resources infrastructure should perform site specific analyses to access the validity of the stationarity assumption. In the context of risk studies, consideration should be made to assess risk over the life of the asset - not only risk in its current state. Considering gauge 01420500 as an example, the 5-yr streamflow calculated with the entire range of historical data (1914-2017) is 19,100 cfs and the streamflow calculated for the post-2000 data (2000-2017) is 29,300 cfs. Put differently, 19,100 cfs corresponds to a 20% probability (5 year turn period) when considering the life of the gauge; however, 19,100 cfs corresponds to a 63% probability (~2.7 year turn period) when considering only the post 2000 data. As risk analyses become increasing popular, land use change continues, and hydroclimatic change progresses, practitioners are encouraged to further study the

impact of the stationarity assumption and consider streamflow regimes as dynamic.

SYMBOLS

$\bar{X}1$ - Average streamflow (cfs) before the breakpoint year 2000

$\bar{X}2$ - Average streamflow (cfs) after the breakpoint year 2000

REFERENCES

ANTOSHIN, S., BERG., A., and SOUTO, M. (2008). "Testing for Structural Breaks in Small Samples." International Monetary Fund (IMF) Working Paper, 29 pages.

ASCE. (2015). "Adapting Infrastructure and Civil Engineering Practice to a Changing Climate". American Society of Civil Engineers, Virginia, United States, J.R. OLSEN Editor, 93 pages.

BAI, J. and PERRON, P. (1998). "Estimating and Testing Linear Models with Multiple Structural Changes." *Econometrica*, Vol. 66, No. 1, pp. 47-78.

EASTERLING, D.R., KUNKEL, K.E., ARNOLD, J.R., KNUTSON, T., LEGRANDE, A.N., LEUNG, L.R., VOSE, R.S., WALISER, D.E., and WEHNER, M.F. (2017). "Precipitation Change in the United States". U.S. Global Change Research Program, Washington, D.C., USA, WUEBBLES, D.J., FAHEY, D.W., HIBBARD, K.A., DOKKEN, D.J., STEWART, B.C., and MAYCOCK, T.K., Editors, pp. 207-230.FALCONE, J.A., CARLISLE D.M., and WEBER, L.C. (2010). "Quantifying Human Disturbance in Watersheds: Variable Selection and Performance of a GIS-based Disturbance Index for Predicting the Biological Condition of Perennial Streams." *Ecological Indicators*, Vol. 10, Iss. 2, pp. 264–273.

IPPC. (2007). "Climate Change 2007 - Impacts, Adaptation and Vulnerability, Contribution of Working Group II to the Fourth Assessment Report of IPPC". Cambridge University Press, New York, United States, M.L. PARRY, O. CANDZIANI, J. PALUTIKOF, P. VAN DER LINDEN and C. HANSON Editors, pp. 1-16.

KUNKEL, K.E., KARL, T.R., BROOKS, H., KOSSIN, J., LAWRIMORE, J.H., ARNDT, D., BOSART, L., CHANGNON, D., CUTTER, S.L., DOESKEN, N., EMANUEL, K., GROISMAN, P.Y., KATZ, R.W., KNUTSON, T., OBRIEN, J., PACIOREK, C.J., PETERSON, T.C., REDMOND, K., ROBINSON, D., TRAPP, J., VOSE, R., WEAVER, S., WEHNER, M., WOLTER, K., and WUEBBLES, D. (2013). "Monitoring and Understanding Trends in Extreme Storms: State of Knowledge." *Bull. Amer. Meteor. Soc.*, Vol. 94, No. 4, pp. 499-514.

LALL, U., JOHNSON, T., COLOHAN, P., AGHAKOUCHAK, A., BROWN, C., MCCABE, G., PULWARTY, R., and SANKARASUBRAMANIAN, A. (2018). "Water. In Impacts, Risks, and Adaptation in the United States: Fourth National Climate Assessment, Volume II". U.S. Global Change Research Program, Washington, D.C., United States, D.R. REIDMILLER, C.W. AVERY, D.R. EASTERLING, K.E. KUNKEL, K.L.M. LEWIS, T.K. MAYCOCK, and B.C. STEWART Editors, pp. 145–173.

MILLY, P.C.D., BETANCOURT, J., FALKENMARK, M., HIRSCH, R.M., KUNDZEWICZ, Z.W.,

LETTENMAIER, D.P., and STOUFFER, R.J. (2008). "Stationarity is Dead: Whither Water Management?" *Science*, Vol. 319, pp. 573-574.

STEDINGER J.R., and GRIFFIS, V.W. (2011). "Getting From Here to Where? Flood Frequency Analysis and Climate." *Jl Amer. Water Resou. Assoc.*, Vol. 47, No. 3, pp. 506-513.

USGCRP. (2009). "Global Climate Change Impacts in the United States." Cambridge University Press, New York, United States, T.R. KARL, J.T. MELILLO and T.C. Peterson Editors, 189 pages.

USGCRP. (2014). "Climate Change Impacts in the United States: The Third National Climate Assessment." U.S. Government Printing Office, Washington, United States, J.M. MELILLO, T.C. RICHMOND and G.W. YOHE Editors, 841 pages.

WAGENER, T., SIVAPALAN M., TROCH, P.A., MCGLYNN, B.L., HARMAN, C.J., GUPTA, H.V., KUMAR, P., RAO S.C., BASU, N.B., and WILSON, J.S. (2010). "The Future of Hydrology: An Evolving Science for a Changing World." *Water Resour. Res.*, Vol. 46, Iss. W05301, pp. 6-7.

7th International Junior Researcher and Engineer Workshop on Hydraulic Structures, IJREWHS'19, B. HEINER and B. TULLIS (Eds), Report 6, U.S. Bureau of Reclamation, Denver, CO, USA - ISBN 978-0-578-69809-0
https://doi.org/10.26077/0vhy-fb17

NUMERICAL STUDY OF FROUDE NUMBER AND SUBMERGENCE RATIO AND THEIR AFFECT ON HYDRAULIC JUMP FLOW PATTERNS FOR A BACKWARD FACING STEP

Kurt Smithgall
S2O Design & Engineering, United States, krsmithgall@gmail.com

Abstract: The surface recirculation region (SRR), or roller of a conventional hydraulic jump, can pose a safety hazard to recreational river users. In contrast, for an undular hydraulic jump (UHJ), the recirculation region lies submerged on the channel bed and does not pose the same risk. For a river engineer designing whitewater parks, it is crucial to know the conditions of undular hydraulic jump formation at instream structures; it can mean the difference between life and death for recreational river users. However, most existing literature has established conditions of UHJ formation only for the case of a plain bed rectangular channel, which is a situation that does not realistically represent whitewater park situations. Thus, there is a need to determine conditions of UHJ formation for instream structures commonly used in whitewater park design. This work utilizes computational fluid dynamics (CFD) to explore conditions of undular hydraulic jump formation where an instream structure is represented as a backward facing step. The CFD toolbox OpenFOAM was used with the interFOAM Volume of Fluid (VOF) solver, and different Reynolds Averaged Navier Stokes (RANS) turbulence models. This research studied the relationship between upstream Froude number and submergence ratio to systematically investigate the limits of undular hydraulic jump formation and to identify zones that produce each of the 5 subtypes of hydraulic jumps, focusing on those that are most desirable for whitewater parks.

Keywords: Undular Hydraulic Jumps, Recreational Hydraulics, Computational Fluid Dynamics.

INTRODUCTION

Recreational river usage has been steadily increasing since 1998 (RPI CONSULTING INC 2006). In 2014, over 20 million users participated in some form of recreational paddlesport (THE OUTDOOR FOUNDATION 2015). Of the larger paddlesport group, 5.6 million users participate in either whitewater kayaking or rafting (THE OUTDOOR FOUNDATION 2015). Economic impact analyses have shown that there is a significant return on investment for the construction of a whitewater park near urban areas. Colorado is the state leading the way with the largest number of constructed whitewater parks (BRAAK 2012; PODOLAK 2012; RPI CONSULTING INC 2006). The primary attraction of any whitewater park is the hydraulic jumps created for the river users. The design engineer's task is to create a hydraulic structure that for a range of flows creates a hydraulic

jump of recreational value without being dangerous. Little literature exists about guidelines for safe recreational hydraulic jumps. One example, from URBAN DRAINAGE AND FLOOD CONTROL DISTRICT (2016), is overly restrictive stating that the incoming Froude number (Fr) must be less than 1.5 at the toe and the slope of the structure must be less than 0.1.

For large, constructed recreation channel projects such as Olympic venues, physical modeling is the preferred method used to evaluate the hydraulic design (GOODMAN AND PARR 1994). Advancements in computing power allow the use of numerical methods (CAISLEY ET AL. 1999). On a smaller scale, typically hydraulic structures are designed for energy dissipation where a large, SRR is desired. However, large SRR's can create conditions that "trap" swimmers or even river users in their boats, similar to conditions at a low head dam. Therefore, it is useful to know when hydraulic jumps occur that do not produce a roller specifically when a hydraulic jump is either in an undular (wave train) or maximum wave (W jump) form (OHTSU AND YASUDA 1991).
Numerous hydraulic studies have been performed where flume experiments are used to classify distinct subtypes of hydraulic jumps based on their hydraulic properties. (CHOW 1959) used incoming Froude number to discretize five different types: undular ($1< Fr < 1.7$), weak ($1.7 < Fr < 2.5$), oscillating ($2.5 < Fr < 4.5$), steady ($4.5 < Fr < 9.0$), and strong hydraulic jumps ($Fr > 9.0$). (RAJARATNAM 1966) categorized different types of hydraulic jumps in sloping channels based on recirculation region and conjugate depth. RYABENKO (1990) studied different undular jump profiles and conditions for existence. CHANSON (1993, 1996) has performed multiple studies on conditions of UHJ formation and categorized specific subtypes of UHJ's (CHANSON AND MONTES 1995). KAWAGOSHI AND HAGER (1990), OHTSU AND YASUDA (1991) and MOSSA ET AL. (2002) studied hydraulic jumps at abrupt drops, also referred to as backward facing steps. Where KAWAGOSHI AND HAGER (1990) focused on wave type flow. OHTSU AND YASUDA (1991) studied the effect of step height. MOSSA ET AL. (2002) studied the effect of tailwater height on the type of hydraulic jump and showed hydraulic jumps exist on a continuous spectrum and at certain flow conditions can oscillate between two types.

While most of the research on hydraulic jump flow patterns and characteristics have utilized physical modeling, numerical methods are becoming more popular. Advances in computing power, allow the use of numerical models to predict time-averaged properties of hydraulic jumps accurately. Both commercial and open-source models exist and agree well with physical model results (BAYON-BARRACHINA AND LOPEZ-JIMENEZ 2015; BAYON ET AL. 2016). However, even numerical models have difficulty predicting some hydraulic jump features such as aeration and recirculation length (MURZYN AND CHANSON 2009). Despite limitations, numerical models currently offer the lowest barrier to entry to studying hydraulic jumps.

Even though 2D and 3D numerical hydraulic modeling are becoming more accessible and accepted. For general river engineering projects, 1D numerical hydraulic models are still the common standard. Of all the possible factors that influence the flow pattern and corresponding subtype of hydraulic jumps, it is believed that incoming Froude number and relative tailwater level

7th International Junior Researcher and Engineer Workshop on Hydraulic Structures, IJREWHS'19, B. HEINER and B. TULLIS (Eds), Report 6, U.S. Bureau of Reclamation, Denver, CO, USA - ISBN 978-0-578-69809-0
https://doi.org/10.26077/0vhy-fb17

are the most important. By studying a range of Froude numbers and submergence ratios it would be possible to categorize types of hydraulic jumps as well as estimate characteristics of what a hydraulic jump might look like using outputs from a less complex 1D numerical model. This study aims to use computational fluid dynamics (CFD) tools to perform a detailed study of how the Fr and depth ratio affect the flow patterns of hydraulic jumps, specifically which subtypes occur for certain values of Fr and h_1/h_0.

METHODOLOGY

Geometry

A backward facing step was used as a simplified drop structure geometry. In this manner, supercritical flow enters the domain at the inlet, flows across the flat step, which represents the plane of the downstream crest of the drop structure. The water level at the outlet forces a return to subcritical flow. For a real drop structure, the structure forces subcritical flow from the inlet to backwater until water beings flowing down the structure accelerating to supercritical flow before abruptly transitioning into the subcritical pool below. Choosing the backward facing step geometry removes the need for the water to accelerate down the structure to attain supercritical conditions, a supercritical inlet can be specified. By using a horizontal flat bottom on the step, it is easier to force a specific Froude number at the inlet since the fluid does not accelerate further due to gravity. This configuration allows the step width to be increased to move the location of the hydraulic jump further away from the inlet to minimize boundary effects on the hydraulic jump.

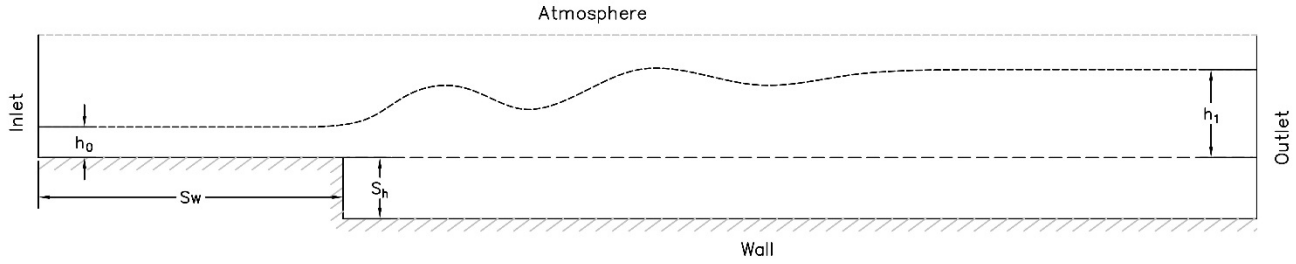

Figure 1: Simulation Schematic

Numerical Tools

For the numerical model, the freely-available open source platform OpenFOAM Version 6 was selected. A hydraulic jump is an incompressible, multi-phase, turbulent problem and selected solver must reflect that. Within the OpenFOAM framework the interFOAM solver was selected since it is capable of resolving transient, incompressible multiphase flow (MARIĆ ET AL. 2014). While a variety of turbulence models can be used with the interFOAM solver, this work will utilize Reynolds-Averaged Navier-Stokes (RANS) turbulence models. OpenFOAM/interFOAM are gaining popularity for multi-phase simulations. Bayon et al. (2016) compared OpenFOAM to FLOW3D, a commercial CFD code, and found that OpenFOAM is better at reproducing the flow

structure of a hydraulic jump.

Boundary Conditions

Table 1 summarizes the boundary conditions used for the model.

Table 1: Boundary Conditions Summary

	Alpha	U	P_rgh	K	Omega
Inlet	Fixed value	Fixed Value	Fixed Flux Pressure	Fixed value	Fixed Value
Outlet	Inlet Outlet	Inlet Outlet	Total pressure	Inlet Outlet	Inlet Outlet
Wall	Zero Gradient	No-slip	Fixed Flux Pressure	Wall Function	Wall Function
Atmosphere	Inlet Outlet	Pressure Inlet Outlet Velocity	Total Pressure	Inlet Outlet	Inlet Outlet

Fixed values for velocity and turbulence are imposed at the inlet to force supercritical conditions. A total pressure boundary is imposed on the outlet forcing hydrostatic pressure. The total pressure boundary at the outlet allows the volume of fluid in the domain to adjust rather than specifying a velocity outlet. Turbulent wall functions were used and will be discussed further in the next section.

Mesh & Sensitivity Analysis

A uniform, structured mesh where all mesh elements are orthogonal tetrahedrals was used since the block structure of a backward facing step is easy to produce with a structured mesh. A mesh refinement study was performed to minimize discretization error for the main simulation set. All meshes are uniform structured meshes where dy = dz. To reduce computation time, all simulations are 2D where the X direction is not computed. Seven mesh sizes in meters were studied: [0.18, 0.065, 0.039, 0.023, 0.014, 0.008, 0.005]. As the mesh size decreases, the resolution of the free water surface increases, but so does simulation time due to increasing the number of cells. The smaller cells require a smaller time step to satisfy the Courant condition. Table 2 summarizes the mesh sensitivity results.

Table 2: Mesh Sensitivity Analysis

Δx	Total Cells	Number of Vertical Cells	y+
0.3	569	2	6419
0.18	1,470	3	4770
0.065	11,396	8	1997
0.039	31,168	13	2056
0.023	89,947	22	1465
0.014	242,760	36	926
0.008	741,250	62	545
0.005	1,900,000	100	339

Figure 2 plots the resulting water surface elevation profile for each mesh resolution. For turbulent, high Reynolds number flows, there are high velocity gradients and viscous effects are important near the wall (POPE 2000). Certain turbulence models are only valid in regions of fully developed turbulence, and do not perform well close to the wall where viscous contributions are important. Rather than refine the mesh to adequately capture the viscous sublayer, wall functions can be implemented to reduce the computational cost of resolving near wall effects. Wall functions rely on the universal law of the wall, or log-law

relations, where the first computational grid cell next to the wall boundary must fall in the log-law region (POPE 2000). The non-dimensional distance to the wall, or y+, is used to see what flow region computational cells fall in. For RANS turbulence models the log-law region falls between

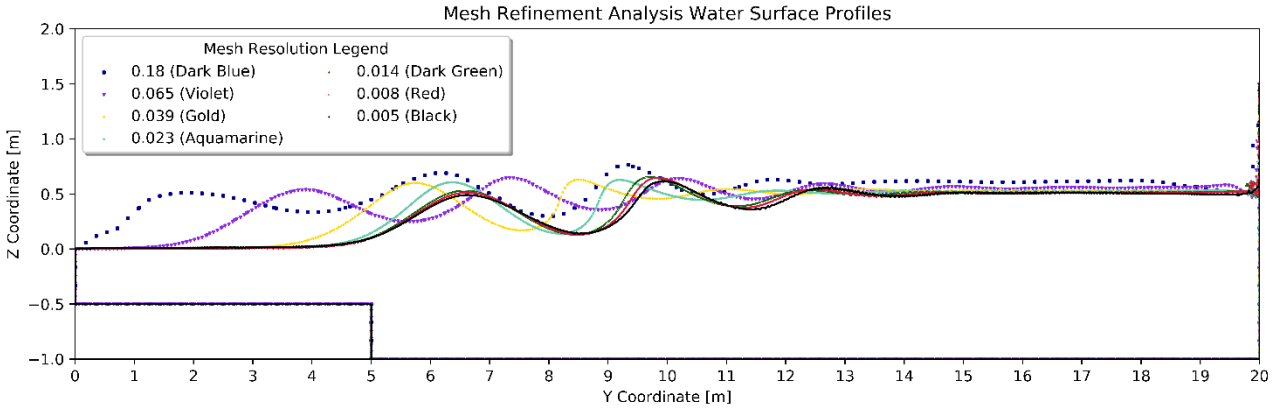

Figure 2: Mesh Refinement Analysis

$30 < y+ < 500$ (VERSTEEG AND MALALASEKERA 2007). Due to computational cost and simulation time, a uniform mesh size of 0.014m was used since figure 2 shows the water surface elevations converging to a common profile. The implications of using this mesh size and y+ will be revisited in the validation section of the results.

Resolving Turbulence

Due to uncertainties with turbulence parameter estimation and specific weaknesses inherent to turbulence models an uncertainty analysis was performed for both turbulence models and turbulence parameters to see how each impacted the resulting water surface profile. A base case of Fr= 1.75 was used and different turbulent model and turbulent parameter combinations were simulated. Only RANS models were used because of widespread use in industrial problems and reduced computation time. The k-ε, RNG k-ε, k-ω and k-ω-SST were the turbulence models selected for this study. Initial turbulence variables were calculated from equations 1 thru 3 (MARIC ET AL. 2014). Where k is the turbulent energy [m^2/s^2], U is mean flow velocity [m/s], I is the turbulence intensity [%], ε is the turbulent dissipation rate [m^2/s^3], Cμ is a turbulent model constant, l is the turbulent length scale [m], and ω is the specific turbulence dissipation rate [1/s]. A mixing length of 0.001m, a turbulent intensity of 5%, and a turbulent model constant of 0.09 was assumed.

$$k = \frac{3}{2}(UI)^2 \quad (1)$$

$$\varepsilon = C_\mu \frac{k^{\frac{2}{3}}}{l} \quad (2)$$

$$\omega = \frac{\sqrt{k}}{l} \quad (3)$$

Additionally, the turbulence parameters were varied one order of magnitude greater and less than the initial calculated value to yield the following sets of parameters: k [0.0055, 0.055, 0.55], ε [0.118, 1.18, 11.8], and ω [23.57, 235.7, 2357]. The results of the turbulent sensitivity analysis showed little differences between the k-ε, k-ω, and k-ω-SST turbulence models. The RNG k-ε model did predict a small SRR. Variation in turbulence variables had little effect on the resulting

water profile. Based on the results of the turbulence sensitivity analysis, the k-ω-SST turbulence model was used moving forward, primarily to avoid known deficiencies of k-ε based models resolving curvature and adverse pressure gradients near the wall as mentioned by POPE (2000).

Computational Resources

The numerical simulations were computed on a 2 x 16 core AMD EPYC 7301 with a clock speed of 2.2 GHz and 128GB of RAM. The total computational cost varied due to use of adaptive time stepping. The Fr=3.0 required both a larger domain and smaller time step than the Fr=1.2. Total computational cost varied from approximately 1756.8 core*hours to 2316.9 core*hours. Since the simulation was run in parallel with 32 subdomains, the real computation time varies from 54.9 to 72.4 hours.

7th International Junior Researcher and Engineer Workshop on Hydraulic Structures, IJREWHS'19, B. HEINER and B. TULLIS (Eds), Report 6, U.S. Bureau of Reclamation, Denver, CO, USA - ISBN 978-0-578-69809-0
https://doi.org/10.26077/0vhy-fb17

Classification of subtypes

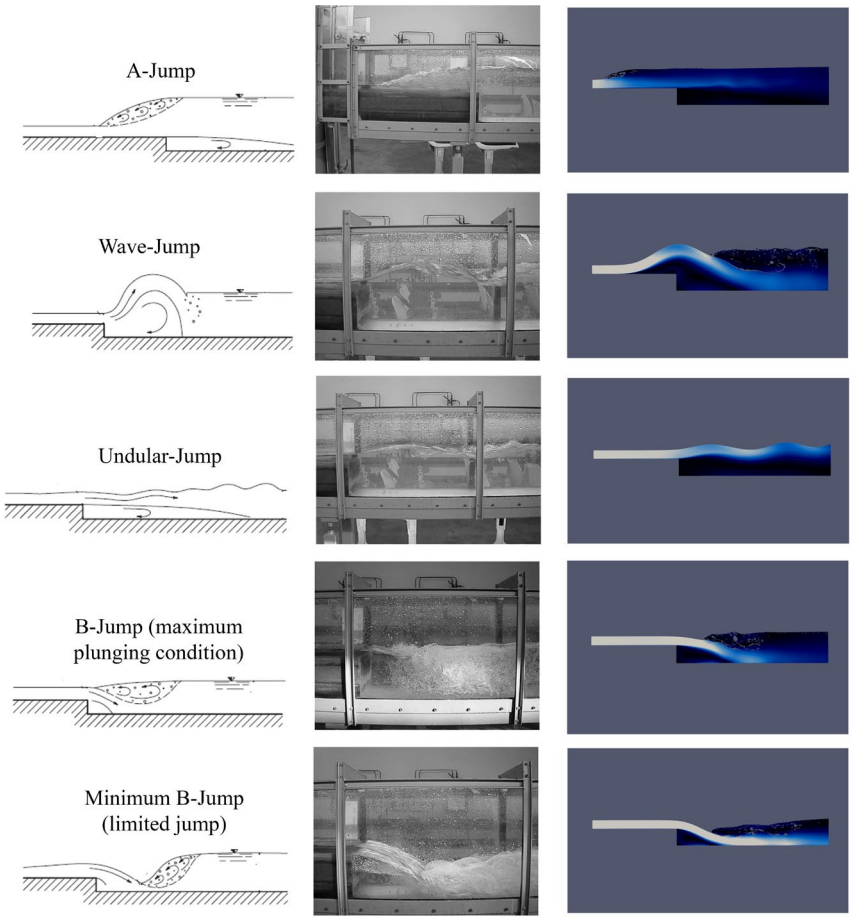

Figure 3: Types of Hydraulics Jumps. Left schematic source (OHTSU AND YASUDA 1991). Center flume study source (MOSSA ET AL. 2002). Right CFD profile from this study

Figure 3, to the left, summarizes different subtypes of hydraulic jumps where sketches, flume study images and CFD simulation data distinguish each subtype. The schematic images in the left column came from (OHTSU AND YASUDA 1991). The center column flume study images came from (MOSSA ET AL. 2002). The right column images came from this study, where the most representative image was selected from the range of simulations. From these classifications, qualitative flow features were identified that are unique to each subtype of hydraulic jump. Table 3 below summarizes the qualitative flow features used to categorize each subtype of hydraulic jump.

Table 3: Qualitative Flow Feature Summary

	Tailwater Height	Horizontal Location of Hydraulic Jump	High Velocity Jet	Recirculation Region
A Jump	Greater than incoming flow	Upstream of step	Jet is deflected upward and diffused by aerated recirculation region	Primary hydraulic jump is an aerated SRR
Wave Jump	Greater than incoming flow	Centered on step	Jet persists past primary hydraulic (wave) and is dissipated by the aerated recirculation region of the secondary hydraulic jump	Large submerged recirculation region under the primary hydraulic jump (wave). Secondary hydraulic jump is a large aerated SRR
Undular Jump	Greater than incoming flow	Downstream of step	Jet persists downstream undulating on the surface, until gradually dissipated	No SRR, submerged recirculation region located under supercritical jet

B Jump	Less than or greater than incoming flow	Downstream of step	Jet plunges downward off the step and is dissipated by the aeration recirculation region	Primary hydraulic jump is a large, aerated SRR
B Jump Limited	Less than or greater than incoming flow	Downstream of step	Jet plunges downward off the step but persists and travels horizontally along the bed, under the aerated recirculation region before being dissipated	Primary hydraulic jump is a large, aerated SRR

RESULTS AND DISCUSSION

Validation

A validation case was created from experimental data collected from KAWAGOSHI AND HAGER (1990). Test series B, case ID 3-2 was selected because it had the thickest flow depth to reduce scale effects. The incoming Froude number is 3.02 and the step height ratio (S_h/h_0) is 3.2. The first validation run featured the uniform mesh size of 0.014m. The resulting wave crest and plunge point significantly differed from experimental measurements so the wall treatment was revisited. For Fr=3.02, and a uniform mesh, the average y+ on the step was found to be 950. A second simulation was created where boundary layers were added to the step surface to increase the near wall resolution. The addition of the boundary layers in the mesh decreased the y+ to 49 and the predicted wave crest and plunge point better match the experimental data as seen in Figure 3. The revised mesh under predicted the horizontal location of the wave crest by 4.3% and over predicted the crest height by 5.9%. The horizontal location of the plunge point was under predicted

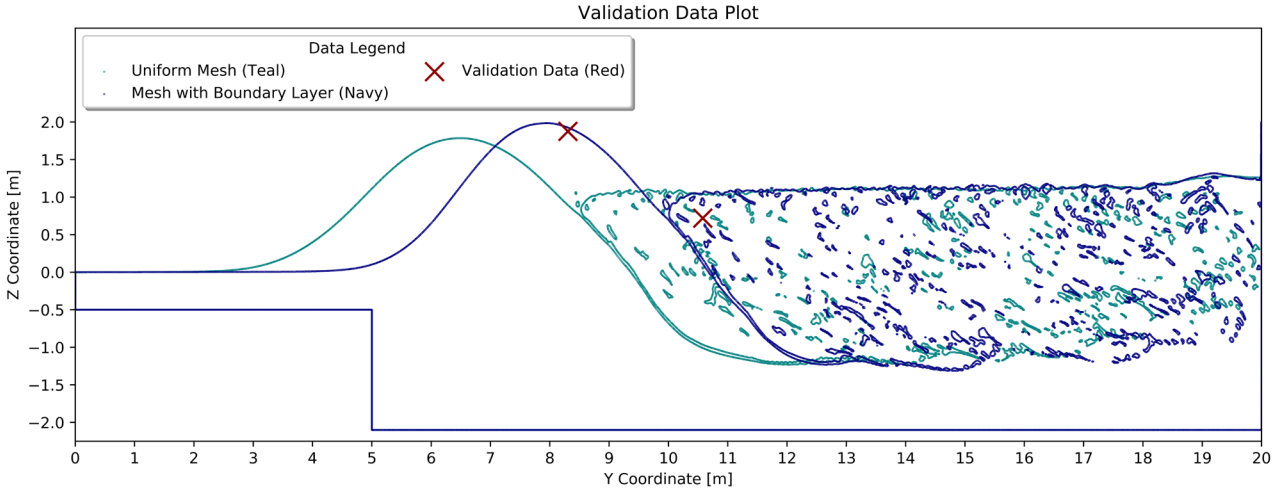

Figure 3: Validation Profile

by 5.9% and over predicted the plunge point elevation by 2.2%. Despite differences between properly resolved boundary layers for predicting wave crest location, there were no differences in the resulting subtype of hydraulic jump for each submergence ratio for a given Froude number.

7th International Junior Researcher and Engineer Workshop on Hydraulic Structures, IJREWHS'19, B. HEINER and B. TULLIS (Eds), Report 6, U.S. Bureau of Reclamation, Denver, CO, USA - ISBN 978-0-578-69809-0
https://doi.org/10.26077/0vhy-fb17

Froude Number and Submergence Ratio Simulations

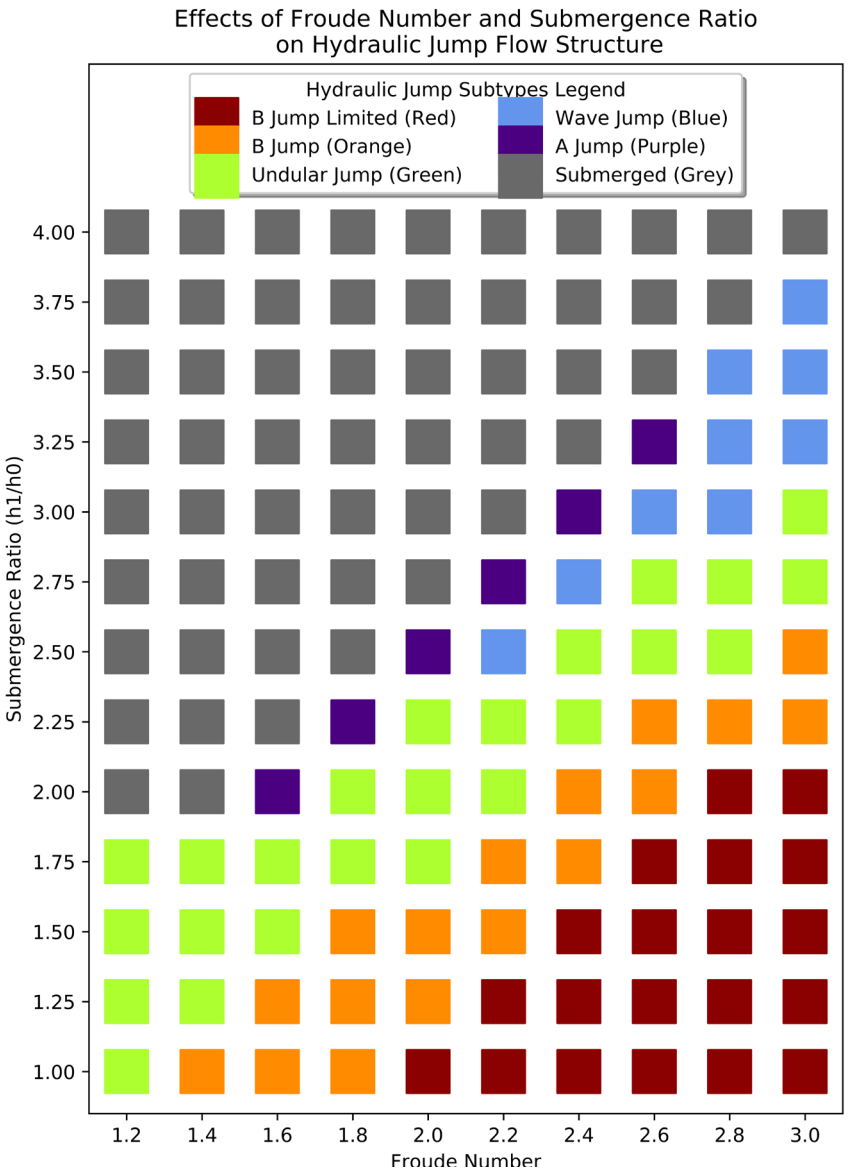

Figure 4: Froude Number and Submergence Ratio Summary

For the primary Froude number and tailwater analysis, a submergence ratio (SR) calculated, h_1 / h_0 was used to separate the step height from the tailwater height. To do this, the elevation of the top of the step is used as the datum (see Figure 1). For all simulations a step height ratio (S_h/h_0) of 2.0 was used, which differs from the validation case. For the study, the following SR's were studied [1.25, 1.5, 1.75, 2.0, 2.25, 2.5, 2.75, 3.0 3.25 3.5 3.75 4.0]. These submergence ratios were simulated for each of the following Froude numbers [1.2, 1.4, 1.6, 1.8, 2.0, 2.2, 2.4, 2.6, 2.8, 3.0]. Figure 4 shows the results of the Froude number and SR analysis where for each unique combination of Froude number and SR the hydraulic jump subtype has been identified according to the characteristics described in Table 3. From Figure 4 two trends can be observed. The first is the general progression of hydraulic jump subtypes as the SR is increased. It is seen that hydraulic jumps transition from B limited jump > B jump > undular jump > wave jump > A jump as the SR increases. The figure also shows how as Froude number increases, the SR for which a give subtype transitions increases as well. When looking at the data in Figure 4, it should be noted that these are discrete points and the exact boundary between two different subtypes of hydraulic jumps is not explicitly known. Also of note is the tendency for hydraulic jumps to oscillate between two different types as observed by MOSSA ET AL. (2002), it's unknown how accurate CFD is at capturing the transition region between two subtypes.

CONCLUSIONS

This study shows that CFD is capable of resolving five different subtypes of hydraulic jumps that form at a backward facing step. A wave type jump simulation was validated with experimental data from KAWAGOSHI AND HAGER (1990). With a properly resolved y+, numerical simulations accurately predict wave crest and plunge point with < 6% error. As predicted, Froude number and submergence ratio are significant factors in determining the type of hydraulic jump that form. Unique combinations of each are able to form different subtypes of jumps. As the submergence ratio increases for a given Froude number, the hydraulic jumps transition from a B limited jump > B jump > undular jump > wave jump > A jump until becoming submerged. These jumps correspond to types identified in laboratory flume tests. As incoming Froude number increases, the submergence ratio that produces each type of hydraulic jump increases as well.

For recreational considerations, the undular and wave jumps are safe hydraulic jumps because they do not have a primary surface recirculation region. Not to say that all hydraulic jumps with a SRR are dangerous, there may be cases with low Froude numbers where a SRR is beneficial for recreation. There are large uncertainties regarding the use of CFD to predict recirculation regions. At the present time, it is not possible to determine safety using CFD alone.

NOMENCLATURE

CFD	Computational Fluid Dynamics
RANS	Reynolds-Averaged Navier-Stokes
RNG	Re-Normalization Group
SR	Submergence Ratio
SRR	Surface recirculation region
SST	Shear Stress Transport
UHJ	Undular hydraulic jump
VOF	Volume of Fluid
k	Turbulent Kinetic Energy
ε	Dissipation rate of turbulent kinetic energy
ω	Specific dissipation rate of turbulent kinetic energy
h_0	Inlet water depth
h_1	Outlet water depth
Fr	Froude number
S_w	Step width
S_h	Step height
$y+$	Dimensionless wall distance

ACKNOWLEDGEMENTS

I thank the anonymous reviewers whose comments have greatly improved this paper

REFERENCES

BAYON-BARRACHINA, A., & LOPEZ-JIMENEZ, P. A. (2015). Numerical analysis of hydraulic jumps using OpenFOAM. *Journal of Hydroinformatics*, *17*(4), 662–678.

BAYON, A., VALERO, D., GARCÍA-BARTUAL, R., VALLÉS-MORÁN, F. J., & LÓPEZ-JIMÉNEZ, P. A. (2016). Performance assessment of OpenFOAM and FLOW-3D in the numerical modeling of a low Reynolds number hydraulic jump. *Environmental Modelling and Software*, *80*, 322–335.

BRAAK, W. (2012). "2011 Economic Impact of Kelly's Whitewater Park in Cascade , Idaho An overview of the park's second year in operation".

CAISLEY, M. E., BOMBARDELLI, F. A., & GARCIA, M. H. (1999). Hydraulic Model Study of a Canoe Chute for Low-Head Dams in Illinois, (UILU-ENG-99-2012).

CHANSON, H. (1993). "Characteristics of Undular Hydraulic Jumps".

CHANSON, H. (1996). Non-Breaking Undular Hydraulic Jump. *Journal of Hydraulic Research*, *34*(2), 279–287.

CHANSON, H., & MONTES, J. S. (1995). Characteristics of undular hydraulic jumps. experimental apparatus and flow patterns. *Journal of Hydraulic Engineering*, *121*(2), 129–144.

CHOW, V. (1959). "Open-Channel Hydraulics". McGraw Hill Book Company.

GOODMAN, F. R., & PARR, G. B. (1994). The Design of Artificial White Water Canoeing Courses. *Proceedings of the Institution of Civil Engineers - Municipal Engineer*, *103*(4), 191–202.

KAWAGOSHI, N., & HAGER, W. H. (1990). Wave type flow at abrupt drops. *Journal of Hydraulic Research*, *28*(2), 235–252.

MARIĆ, T. HÖPKEN, J. MOONEY, K. (2014). "The OpenFOAM Technology Primer". Sourceflux.

MONTES, J. S., & CHANSON, H. (1998). Characteristics of Undular Hydraulic Jumps: Experiments and Analysis. *Journal of Hydraulic Engineering*, *124*(2), 192–205.

MOSSA, M., PETRILLO, A., & CHANSON, H. (2002). Tailwater level effects on flow conditions at an abrupt drop. *Journal of Hydraulic Research*, *40*(4), 1–13.

MURZYN, F., & CHANSON, H. (2009). Two-phase gas-liquid flow properties in the hydraulic jump: Review and Perspectives. *Multiphase Flow Research* 497–542.

OHTSU, I., & YASUDA, Y. (1991). Transition from supercritical to subcritical flow at an abrupt drop. *Journal of Hydraulic Research*, *29*(3), 309–328.

OHTSU, I., YASUDA, Y., & GOTOH, H. (2001). Hydraulic Conditions for Undular-jump formations. *Journal of Hydraulic Research*, *39*(2), 203–209.

OHTSU, I., YASUDA, Y., & GOTOH, H. (2004). Flow Conditions of Undular Hydraulic Jumps in Horizontal Rectangular Channels, *129*(12), 948–955.

PODOLAK, K. N. (2012). "Multifunctional Riverscapes: Stream Restoration, Capability Brown's water features, and artifical whitewater". University of California Berkeley.

POPE, S. (2000). "Turbulent Flows". Cambridge University Press.

RAJARATNAM, N. (1966). The Hydraulic Jump in Sloping Channels. *Irrigation & Power: The Journal of the Central Board of Irrigation & Power*, *23*(2), 137–149.

RPI CONSULTING INC. (2006). "Economic Impacts of Whitewater Recreation".

RYABENKO, A. (1990). Conditions favorable to the existence of an undulating jump. *Hydrotechnical Construction*, *24*(12), 762–770.

THE OUTDOOR FOUNDATION. (2015). "2015 Special Report on Paddlesports".

URBAN DRAINAGE AND FLOOD CONTROL DISTRICT. (2016). "Urban Storm Drainage Criteria Manual: Volume 2 Structures, Storage, and Recreation".

VERSTEEG, H. MALALASEKERA, W. (2007). "An Introduction to Computational Fluid Dynamics, The Finite Volume Method". Pearson Education Limited.

7th International Junior Researcher and Engineer Workshop on Hydraulic Structures, IJREWHS'19, B. HEINER and B. TULLIS (Eds), Report 6, U.S. Bureau of Reclamation, Denver, CO, USA - ISBN 978-0-578-69809-0
https://doi.org/10.26077/0vhy-fb17

7th International Junior Researcher and Engineer Workshop on Hydraulic Structures, IJREWHS'19, B. HEINER and B. TULLIS (Eds), Report 7, U.S. Bureau of Reclamation, Denver, CO, USA - ISBN 978-0-578-69809-0
https://doi.org/10.26077/ef2d-rz76

COMPOSITE EXPERIMENTAL AND NUMERICAL MODELING OF ARCED LABYRINTH WEIRS

Seth THOMPSON
Civil and Environmental Engineering, Utah State University, USA, seth.d.thompson@gmail.com
Blake TULLIS, PhD
Civil and Environmental Engineering, Utah State University, USA, blake.tullis@usu.edu

Abstract: Arced labyrinth weirs are a viable option for existing spillway retrofit due to their increased flow capacity. This study supplies additional arced labyrinth weir hydraulic design empirical data and uses this data to validate a numerical model (utilized Flow-3D) of the same experimental setup. The dimensionless discharge coefficient relationship is presented for the physical model, potential errors due to physical model crest referencing are discussed, and the relative and absolute errors along with a grid convergence study are given for the numerical model.

Keywords: Arced Labyrinth Weirs, Spillway Hydraulics, CFD.

INTRODUCTION

Due to higher frequency in extreme flood event occurrence in recent years, estimates for design storm requirements (i.e. probable maximum flood (PMF), 500-year storm, etc.) have increased. Consequently, many reservoir systems no longer meet discharge requirements. Labyrinth weirs provide a feasible retrofit to existing, fixed-width spillways as the length and resultingly the discharge capacity of the spillway can increase with no change in spillway width. Tullis et al. (1995) state that a nonlinear weir, such as a labyrinth weir, can approximately double the discharge capacity relative to a linear weir.

In reservoir applications, arcing a labyrinth spillway can further improve hydraulic efficiency. When spillways are engaged, the approach flow tends to converge towards the spillway. By arcing the labyrinth weir, the inlet cycles are better oriented to the approach flow and the inlet cycle area increases; these factors help the spillway efficiently handle reservoir-type flow patterns.

Existing Arced Labyrinth Weir Research

Crookston (2010) conducted research on six arced labyrinth weirs and nine non-arced labyrinth weirs in a laboratory scaled headbox/reservoir at the Utah Water Research Laboratory (UWRL) at Utah State University. Each weir had 5 cycles (N=5), a half-round crest, and trapezoidal labyrinth geometry. The arced labyrinth weirs tested had sidewall angles (α) equal to 6° and 12° each at three different cycle arc angles (θ = 10°, 20°, and 30°). Christensen (2012) furthered this research by including α=20° and including N=7 and 10 for α=12°, and N=10 for α=20°.

Crookston (2010) found that arcing a labyrinth weir can increase hydraulic efficiency by ~5-11%

when compared to non-arced labyrinth weirs in reservoir applications. However, because of the increased inlet cycle area compared to the outlet cycle area, this increase in hydraulic efficiency exceeds the outlet free-flow capacity at smaller heads relative to the weir crest (H_T/P) when compared to non-arced labyrinth weirs. This causes arced labyrinth weirs to submerge sooner than non-arced weirs. Furthermore, Christensen (2012) found that increasing the cycle number has little effect on discharge efficiency, and linearly increases flow capacity with the increased weir length. Christensen (2012) also noted nappe behavior. Due to the increased flow capacity of the inlet cycles and decreased free flow capacity of the outlet cycles, the arced labyrinth weirs tested did not fully aerate; only partial, oscillating aeration was present until the weirs became drowned.

The empirical data of Crookston (2010) and Christensen (2012) represent the primary source used to predict hydraulic performance of prototype arced labyrinth weirs. Therefore, designers are forced to interpolate when prototype geometries do not exactly match the aforementioned geometries tested. This study was undertaken to reduce the level of uncertainty when using interpolated data by providing additional empirical reference data and using computational fluid dynamic (CFD) modeling in an effort to replicate the empirical data. This report focuses on the challenges, benefits, and results that are presented through composite modeling, in this case, physical and numerical.

Composite Modeling

Savage et al. (2016) extended the research of Crookston and Tullis (2013) by modeling a 4-cycle, α=15° non-arced labyrinth weir in a laboratory flume at $H_T/P > 1.0$ (where H_T/P is the dimensionless ratio of total head to weir height). This physical model was used to validate a numerical model, which simulated flow over two cycles of the same weir. All relative errors between the physical and numerical model were within ±3%. While it is common to attribute relative errors to the estimations and assumptions made in the numerical model, these relative errors also can be partially assigned to errors in physical modelling (i.e. errors in crest elevation reference, weir levelness, and individual point measurements).

Crookston et al. (2018) performed a similar study by comparing existing piano-key weir laboratory data (Anderson and Tullis 2013) to numerical models. The results of Anderson and Tullis (2013) were replicated with error bars between ~3-4%. Both Savage et al. (2016) and Crookston et al. (2018) sought to determine the effect of multiple numerical turbulence models on the discharge coefficient (C_d) solution. Savage et al. (2016) modeled the large eddy simulation (LES) and the renormalized group theory (RNG) turbulence models, while Crookston et al. (2018) studied the LES and the RNG k-ε models. Both studies concluded that turbulence model has little effect on C_d due to the non-turbulent nature of the flow upstream of the nonlinear weirs. Both studies also concluded that CFD modeling must be validated with empirical data or ideally a physical model of the proposed prototype.

Approach and Application

One arced labyrinth weir (α=16°, θ=30°) has been physically and numerically modeled. Initially the physical model was tested and then replicated numerically. This study presents the challenges and

7th International Junior Researcher and Engineer Workshop on Hydraulic Structures, IJREWHS'19, B. HEINER and B. TULLIS (Eds), Report 7, U.S. Bureau of Reclamation, Denver, CO, USA - ISBN 978-0-578-69809-0
https://doi.org/10.26077/ef2d-rz76

errors inherent in physical and numerical modeling such as: crest elevation referencing, and numerical mesh convergence. Finally, the results between the physical and numerical model are presented.

EXPERIMENTAL METHOD

Physical Modeling

Physical modeling of the α=16°, θ=30 arced labyrinth weir took place at the Utah Water Research Laboratory (UWRL) at Utah State University, Logan, UT. The weir was fabricated of 2.54-cm thick polyvinyl chloride sheeting (PVC). The weir was 20.5 cm tall (P=20.5 cm), 2.54 cm thick (t_w=2.54 cm), with a half-round crest shape; basic weir geometry is given in Fig. 1. The weir was tested in a reservoir/headbox (7.2 x 7.2 x 1.5 m deep) with flow converging from 180° to simulate reservoir approach flow conditions. The weir was installed, projecting into the reservoir on an acrylic platform/apron (2.8 x 1.2 m) 8.9 cm above the reservoir bed; the apron was level to within ±1.6 mm. Approach ramps sloped up from the reservoir floor at 0.073 m/m to the weir apron. The weir was installed and levelled using a survey level to within ± 0.794 mm (40 measurements taken). The average crest elevation was then referenced to a stilling well point gauge using the survey level.

Fig. 1 – α=16°, θ=30 arced labyrinth weir (a) and profile view of labyrinth weir hydraulic parameters (b).

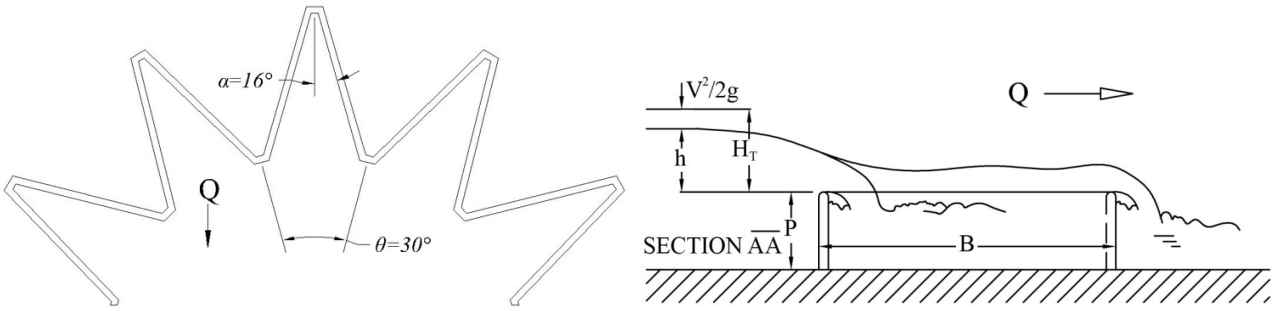

(a) (b)

Flow was measured via calibrated electromagnetic meters installed in 15.2 cm (6 in.) and 50.8 cm (20 in.) diameter supply lines. Flow measurements were made under steady state conditions at 22 Hz and averaged over 5 min. Two 5 min averages were taken for each data point. Piezometric head (h) was measured using a precision point gauge (± 0.152 mm accuracy) placed in a stilling well; the stilling well was hydraulically connected to the reservoir through a piezometer tap located 4.9 m upstream from the downstream edge of the weir apron. Piezometric head measurements were also made twice at each datapoint, immediately after flow measurements were recorded. Approximately 30 points were measured between H_T/P=0.05 and 0.45. An acoustic dopple velocimeter was used to measure velocity head ($V^2/2g$) at the pressure tap at every 0.1 H_T/P.

Numerical Modeling

The CFD program used solves the Reynolds Averaged Navier Stokes (RANS) equations using a

finite-volume approximation, where the RANS equations are solved for each cell of the model domain. The RNG k-ε turbulence model was selected along with the split-Lagrangian volume of fluid (VOF) advection scheme to temporally and spatially track the free-surface (based on Crookston et al. 2018 and Savage et al. 2016). The solver was also set to solve the full momentum and continuity equations.

To model the arced labyrinth weir, three-dimensional drawings of the weir, apron, approach ramps, and reservoir were created that replicate the physical model setup. Prior to the simulation, the CFD solver uses a series of flat planes that intersect each grid cell to spatially render the solid. This algorithm is named the fractional area/volume obstacle representation (FAVOR); the FAVOR rendering of the geometry and initial fluid region are shown in Fig. 2. Due to the symmetry of the setup and observed flow conditions only half of the weir and headbox were modelled numerically (see Fig. 2).

Fig. 2 – Numerical Model extents, FAVOR rendering, and boundary conditions.

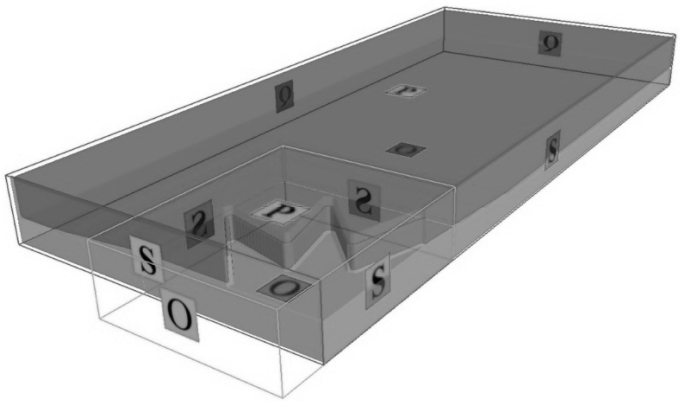

Two meshes were used to render the numerical domain; an upstream reservoir (coarser) mesh, and a nested, weir (finer) mesh. The reservoir mesh was held at a constant size (Δ) of 27.4 mm. Three weir mesh sizes were tested with sizes: 13.7, 9.14, and 6.86 mm and normalized by the weir thickness as Δ / t_w =0.54, 0.36, and 0.27, respectively. Due to the converging flow patterns, the upstream boundary conditions were set at a constant flowrate (Q) and a history probe was set at the location of the physical model's piezometer to measure h. Symmetry, or free slip, boundaries were placed between the inter-block mesh boundaries and the lateral boundary that splits the weir in half. Outflow boundaries were placed at the free discharging boundary, and atmospheric pressure boundaries at the maximum elevation extents. All boundary conditions are shown in Fig. 2 on their respective planes. Upon completion of the physical modeling, six datapoints were numerically modeled based on physical model discharges at H_T/P = 0.3 and 0.4 using each weir mesh size. The numerical data were then compared to the physical using the dimensionless discharge coefficient (C_d) from the standard weir equation (Eq. (1)) where Q is discharge, C_d is the discharge coefficient, L_c is the weir centerline length, g is the gravitational constant, and H_T is the total head relative to the weir crest.

$$Q = \frac{2}{3} C_d L_c \sqrt{2g}\, H_T^{\frac{3}{2}} \tag{1}$$

7th International Junior Researcher and Engineer Workshop on Hydraulic Structures, IJREWHS'19, B. HEINER and B. TULLIS (Eds), Report 7, U.S. Bureau of Reclamation, Denver, CO, USA - ISBN 978-0-578-69809-0
https://doi.org/10.26077/ef2d-rz76

EXPERIMENTAL RESULTS

Hydraulic Performance

In Eq. (1), H_T is defined as the piezometric head, due to the negligible effect of velocity head in the reservoir setting. Although this model represents an extreme case where velocity could be a large contributor towards driving head, due to very shallow approach depths (approximately 1.5P), velocity head was found to only be 0.06 – 0.23% of the total head. This error translates to a 0.08 – 0.35% error in C_d when velocity head is ignored. In prototype applications, velocity head is likely unknown and also negligible due to unknown reservoir bathymetry and deep approach geometries. Therefore, C_d has been determined to be a function of piezometric head, or $H_T = h$.

C_d represents a weir's discharge efficiency per-unit-length and is shown in Fig. 3 in terms of H_T/P for the α=16°, θ=30° arced labyrinth weir of this study and the α= 12° and 20°, θ=30° (Crookston 2010 and Christensen 2012) weirs tested previously. In Fig. 3, it is noted that little efficiency is lost from decreasing α from 20° to 16°. However, at the same downstream cycle width (w') opening. The α=16° has 20% more weir length, which linearly translates to ~20% more discharge capacity given the similar C_d behavior. This also demonstrates the non-linear relationship in discharge efficiency and α; further research is being done to determine the relationship between discharge efficiency and α for 12° < α < 20°. When using these results in design, designers may calculate a rating curve (H_T vs. Q) by using Eq. 1 and the datasets in Fig. 3; interpolation between datasets may be used for other α. However, physical model verification is required for inclusion of site-specific influences not present in this study.

Fig. 3 – C_d vs. H_T/P for arced labyrinth weirs of α =12°, 16°, and 20° with θ =30°.

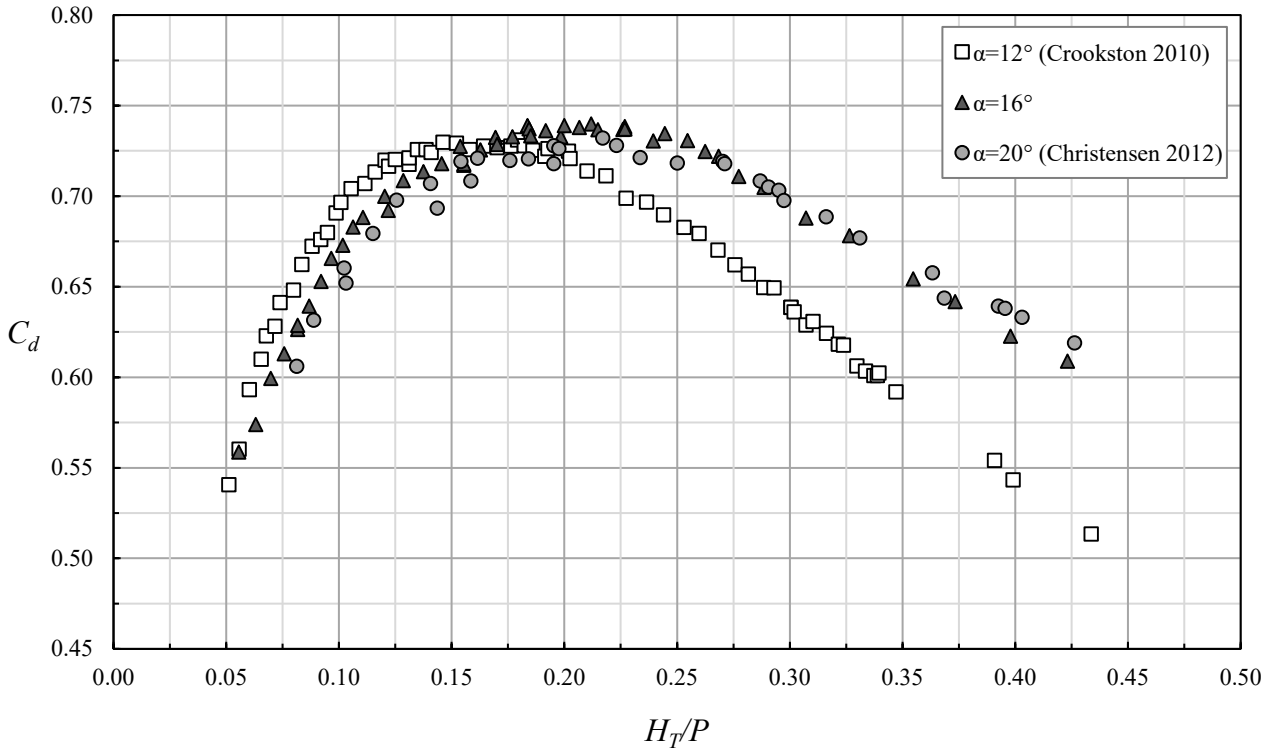

Sources of Error

Crest reference elevation measurements can cause large errors in C_d estimates and rating curve development. The crest reference is significant, because each head measurement is referenced to it and, at low heads, a minor error can be a significant portion of the actual h. At the lowest head measured, H_T/P=0.0556 or 11.39 mm, a 1 mm (0.488% of the weir height) error in crest reference elevation can cause an 8.78% error in h and 14.8% error in C_d. This relationship is shown in Fig. 4 with the absolute and relative errors (ε) in C_d shown. It should be noted that individual errors in head measurements can cause similar error propagation at a single point, but the crest reference error affects every head measurement taken.

Fig. 4 – Absolute and relative errors in C_d vs H_T/P based on a ±1 mm error in the crest reference.

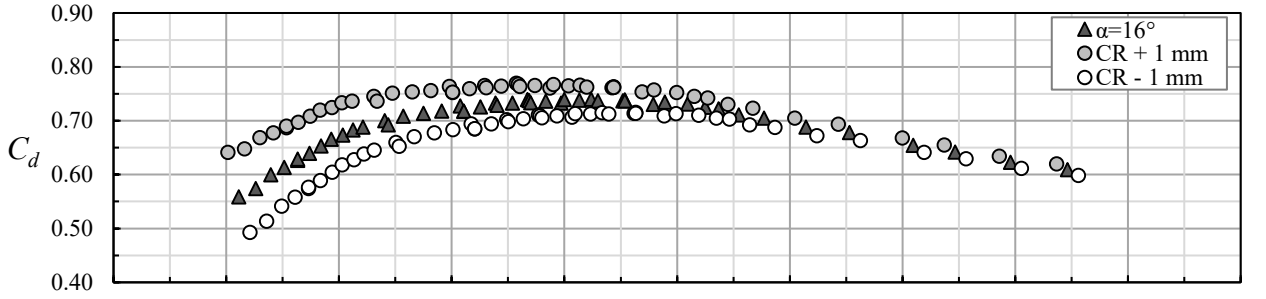

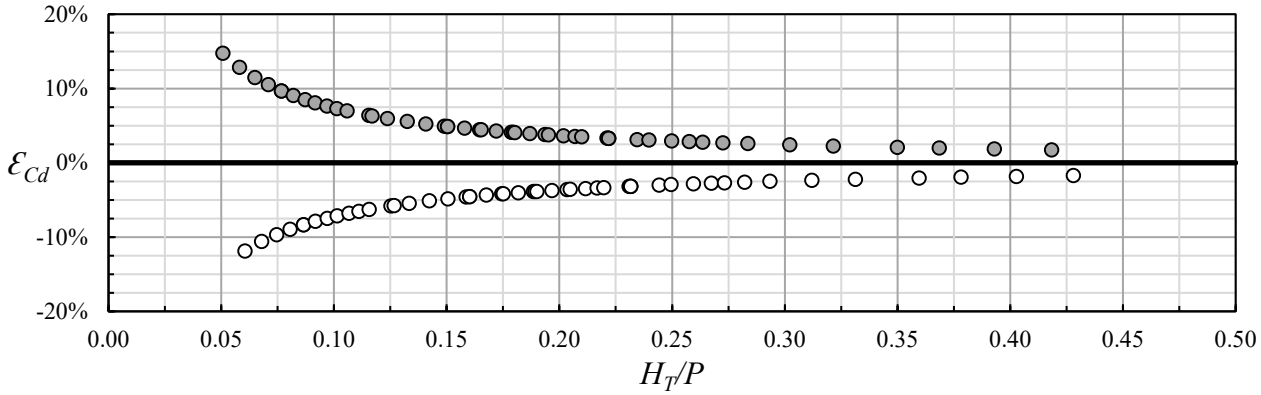

Based on the relationship shown, care must be taken to ensure accurate referencing of the crest elevation to the head measurement device. With the increased length of non-linear weirs, such as arced labyrinths, this poses a great challenge. As mentioned in the experimental setup, the weir for this study was leveled to within ± 0.794 mm; 40 points (8 per cycle) across the weir's length were measured, any point that exceeded the bounds was re-levelled and measured. A survey level and rod, accurate to the ± 0.794 mm threshold was used. Therefore, the instrumentation was a limiting factor. Once the weir was level, an average of the 40 points was taken and used as the representative crest elevation and referenced to the point gauge in the stilling well using the same survey level and rod. This process was repeated several times until a repeatable crest reference value was obtained. With these precautions taken, data collectors can more confidently report head-discharge data to be used in engineering design with sound engineering judgement.

Numerical Results

In order to obtain a mesh independent solution, the CFD solver simulated flow over the weir at each of the three weir meshes (Δ/t_w =0.54, 0.36, 0.27) at both H_T/P=0.3 and 0.4.The grid convergence index (GCI) was then calculated as per ASCE (2009). The GCI allows for self-validation of the model based on the desired solution (f_i), the grid refinement ratio ($r=\Delta_2/\Delta_1$), the order of convergence (p) and an empirically based safety factor (F_s); typically, F_s=1.25 for three mesh studies. Using these parameters, the GCI is defined in Eq. (2):

$$GCI = F_s\,|(f_2 - f_1)/f_1|/(r^p - 1) \tag{2}$$

Where f_2 denotes the coarser of the two meshes. For this study C_d was selected as f. The GCI for each mesh and both H_T/P=0.3 and 0.4 is shown in Table 1. While the GCI does not guarantee solution accuracy, it does give a level of confidence that the solution is approaching grid independency and is within the asymptotic range of the actual solution.

Table 1 – GCI calculations for H_T/P=0.3 and 0.4.

F_s=1.25, p=2				
Δ/t_w	r (Δ_2/Δ_1)	C_d	relative error ($\lvert f_2\text{-}f_1\rvert/f_1$)	GCI (%)

H_T/P=0.3	0.54	–	0.763	–	–
	0.36	1.50	0.711	0.0739	7.39%
	0.27	1.33	0.704	0.0103	1.66%
H_T/P=0.4	0.54	–	0.654	–	–
	0.36	1.50	0.643	0.0173	1.73%
	0.27	1.33	0.644	0.0008	0.13%

Upon completion of the physical and numerical modeling, the numerical model results were compared to a curve-fitted approximation of the physical model results (see Fig. 4) with generally good agreement. At the finest mesh, Δ/t_w=0.27 the relative errors were 0.77 and 1.31% for H_T/P=0.3 and 0.4, respectively. These errors can be attributed to both numerical and physical modeling; however, the likely source for most errors can be attributed to the approximations/assumptions made in the CFD calculations of the fluid flow solver and weir geometry.

The good behavior of the CFD model suggests that both physical and numerical models are accurately representing the hydraulic behavior of the arc labyrinth weir geometry tested, and that CFD could be a useful tool for predicting hydraulic performance for other geometric variations of arced labyrinth weirs. The use of CFD modeling is recommended when designing arc labyrinth weirs due to its ability to implement site-specific conditions and give a level of assurance when using and interpolating between the available empirical data.

Fig. 4 – physical and numerical C_d (a) results and relative error (ε_{Cd}) (b).

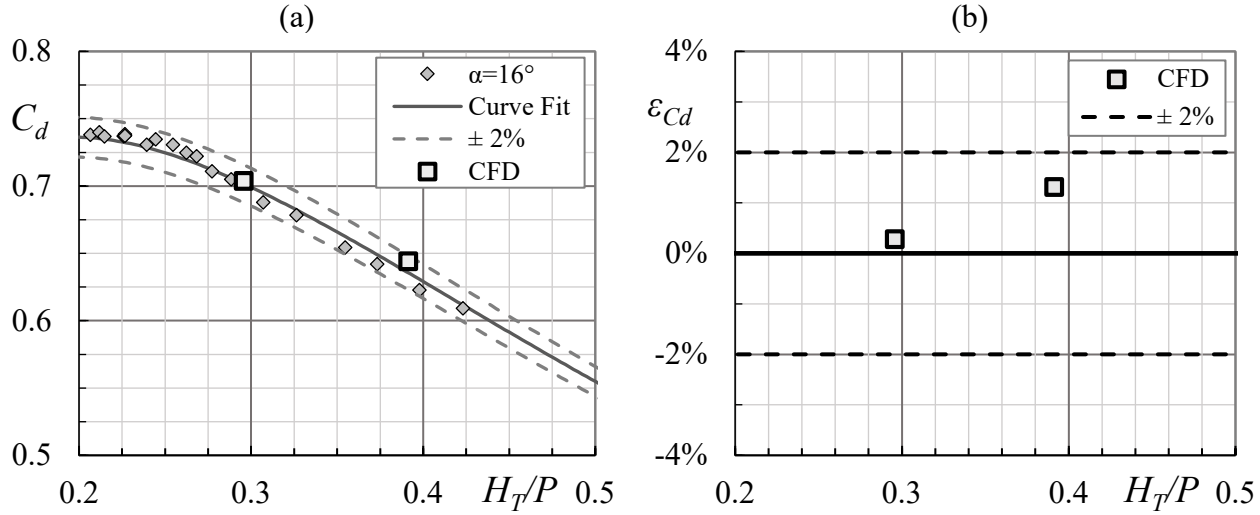

CONCLUSION

Arced labyrinth weirs pose a good solution as an existing spillway retrofit. The decrease in α from 20° to 16° causes little loss in discharge efficiency, but increases capacity, at the same *w'*, due to the increase in weir length. When modeling nonlinear weirs, the modeler must take extra precaution to level the weir and obtain a reliable crest reference otherwise significant errors can be present at all data points. CFD can be a useful to in predicting arced labyrinth weir discharge with errors < 2%. However, verification between empirical data or a physical model study, is recommended to ensure

that the CFD solution is converging towards the physical model. When modeling both physically and numerically, careful care in model construction and data collection must be taken in both models for good agreement to exist.

SYMBOLS

α	sidewall angle	C_d	dimensionless discharge coefficient from Eq. 1
Δ	characteristic cell size	ε_{Cd}	CFD relative error in C_d
f	representative CFD solution	F_s	factor of safety
g	gravitational constant	h	piezometric head
H_T	total head	L_c	weir centerline length
N	cycle number	P	weir height
p	CFD solver order of convergence	Q	discharge/flowrate
r	cell size ratio (Δ_2/Δ_1)	θ	cycle arc angle
t_w	weir sidewall thickness	V	upstream velocity at pressure tap
w'	cycle opening width		

ACKNOWLEDGMENTS

The authors would like to acknowledge the UWRL and Utah State University for funding this research and Brian Crookston and Nathan Christensen for their previous research on arced-labyrinth weirs, laying the groundwork for this study.

REFERENCES

ANDERSON, R. M., and TULLIS, B. P. (2013). "Piano Key Weir Hydraulics and Labyrinth Weir Comparison." *J. Irrig. Drain Eng.*, 139(3), 246–253.

ASCE. (2009). "CHAPTER 2 TERMINOLOGY AND BASIC METHODOLOGY." *Verification and Validation of 3D Free-Surface Flow Models*, 19–44.

CHRISTENSEN, N. A. (2012). "Flow Characteristics of Arced Labyrinth Weirs." MS thesis. Utah State University Library, Logan, Utah. 21–29.

CROOKSTON, B. M. (2010). "Labyrinth weirs." PhD dissertation. Utah State University Library, Logan, Utah. 44-66, 95-122.

CROOKSTON, B. M., ANDERSON, R. M., and TULLIS, B. P. (2018). "Free-flow discharge estimation method for Piano Key weir geometries." *Journal of Hydro-Environment Research*, Elsevier, 19(3), 160–167.

CROOKSTON, B. M., and TULLIS, B. P. (2013). "Hydraulic Design and Analysis of Labyrinth Weirs. I: Discharge Relationships." *Journal of Irrigation and Drainage Engineering*, 139(5), 363–370.

SAVAGE, B. M., CROOKSTON, B. M., and PAXSON, G. S. (2016). "Physical and Numerical Modeling of Large Headwater Ratios for a 15° Labyrinth Spillway." *Journal of Hydraulic Engineering*, 142(11), 04016046.

TULLIS, J. P., AMANIAN, N., and WALDRON, D. (1995). "Design of Labyrinth Spillways." *Journal of Hydraulic Engineering*, 121(3), 247–255.

7th International Junior Researcher and Engineer Workshop on Hydraulic Structures, IJREWHS'19, B. HEINER and B. TULLIS (Eds), Report 8, U.S. Bureau of Reclamation, Denver, CO, USA - ISBN 978-0-578-69809-0
https://doi.org/10.26077/85a1-fa31

Modeling of a Novel Submerged Oscillating Water Column (SOWC) Energy Harvester

Mohammadamin TORABI
Ph.D. candidate, Department of Civil and Environmental Engineering, Idaho State University, USA, toramoha@isu.edu
Bruce SAVAGE
Associate Professor, Department of Civil and Environmental Engineering, Idaho State University, USA, savabruc@isu.edu

Abstract: Wave energy converters (WEC) are hydraulic structures that are used to harvest energy from oceans. This research explores a new concept of a WEC termed a Submerged Oscillating Water Column (SOWC). Numerical simulations using the Computational Fluid Dynamics (CFD) code Flow-3D and physical model tests were carried out at Idaho State University to assess the validity and efficiency of the proposed device. The SOWC device consists of two submerged chambers that are connected to allow airflow between the two as waves pass; ideally spaced at half a wavelength. The results of the CFD modeling for seventeen different geometries with linear waves were investigated. The model was validated with experimental tests in a flume and the efficiency of the device calculated. The influence of four parameters: water depth, wave height, period and the size of SOWC were investigated. The numerical CFD modeling indicates the ratio of water elevation movement inside the chambers can be up to 80% of wave height. The numerical and physical models indicate that the concept of the SOWC works.
Keywords: Submerged oscillating water column(SOWC), wave tank, wave energy

INTRODUCTION

Due to potential shortages of fossil energy, many countries are interested in using renewable energy. Suitable renewable energy alternatives are required to maintain and even improve our standard of living. As more than 40% of the US population lives within 50 miles of a coastline, wave energy has the potential to provide a local renewable natural resource to a large share of the US population. There exists a significant amount of energy within waves that can be extracted (Jacobson et al. 2011).

Typical ocean waves are generated by wind interacting with the ocean surface. These wind-blown waves can travel large distances over deeper parts of oceans without a significant loss of energy. However, wave velocities slow down in nearshore regions due to bed friction and bottom

slope. This causes the wavelength to decrease and the height to increase that leads to breaking waves at certain locations when the ratio of wave height to wavelength is 1 to 7 (Cruz 2007). The total wave energy resource along the outer continental shelf estimated by EPRI is 2,640 TWh/yr (Washington, 2019). Considering that 1 TWh/yr can supply the power for approximately 93,850 U.S. homes annually (Jacobson et al. 2011), there is a significant potential for wave energy. Different Wave Energy Converters (WEC) have been invented to capture ocean wave energy in the last century. These devices are categorized by the installation location as shoreline, nearshore and offshore or the Power Take-Off (PTO) system. Also, most devices can be characterized as belonging to one of six types: Attenuator; Point Absorber; Oscillating Wave Surge Converter (OWSC); Oscillating Water Column (OWC); Overtopping Device and Submerged Pressure Differential (Figure 1). Alamian et al. 2014 outlines attenuators such as the Pelamis and the Anaconda. Point Absorbers are single floats on the surface absorbing energy from all directions generating 250 kW to 1MW. These include Columbia Power(CPT) (Rhinefrank et al. 2010; Brekken 2010), OPT- PB 500 (Dufera 2016), Finavera (Callaway 2007), Seabased/ Uppsala Univ., Archimedes Wave Swing, SeaRev (Ruellan et al. 2010) and Wavebob (Weber et al. 2009). OWSCs extract energy through an oscillating arm and OWCs are partially submerged devices that are open to the sea below the water surface and with a column of air that raises and lowers with the waves such as Wavegen and Oceanlinx with 500kw and 1.5 MW generated power respectively (Drew et al. 2009). Submerged pressure differential devices are typically located nearshore and attached to the seabed. The motion of the waves causes the sea level above the device to increase and decrease which leads to a pressure differential in the device. Archimedes Wave Swing is an example of this device (Valério et al. 2007). The proposed device has the benefit of minimizing the environmental and aesthetical impacts, ability to weather severe weather events. Also, it can develop a low cost, high-performance solution.

Figure 1: wave energy devices; left to right: Attenuator, point absorber, OWSC, OWC, Overtopping (Wave, 2019)

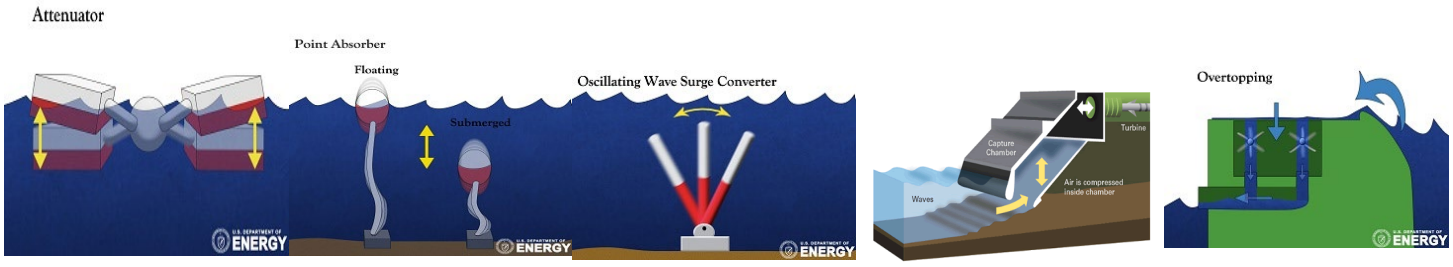

CONCEPTUAL SOWC

7th International Junior Researcher and Engineer Workshop on Hydraulic Structures, IJREWHS'19, B. HEINER and B. TULLIS (Eds), Report 8, U.S. Bureau of Reclamation, Denver, CO, USA - ISBN 978-0-578-69809-0
https://doi.org/10.26077/85a1-fa31

This study explores a novel submerged oscillating water column (SOWC), that combines the existing technology of point absorbers, and oscillating columns. The proposed SOWC is constructed by inverting a pipe, capping one end and embedding a float/buoy inside the cylinders connected in series as shown in Figure 2. The vertical pipe is attached to the seafloor and an air pocket is maintained at the top of the pipe creating an air/water surface for a float. This structure by itself would be useless. However, by linking the air reservoirs of multiple SOWCs, it allows a constant pressure to be maintained between the SOWCs. The pressure within the SOWC is similar to the wave surface with a constant pressure.

As waves move across the ocean surface, peaks and troughs create oscillating hydrostatic pressure differentials on the ocean floor. By placing SOWCs one-half of a wavelength apart, one SOWC experiences an increase in pressure, while the other SOWC sees a decrease in pressure. Connecting the air reservoir between the two SOWCs allows the air to move between the devices, with the increased pressure raising the water surface inside one column while the decreasing pressure lowers the water surface in the other column. As noted previously, a float inside the SOWC will use the principle of buoyancy to drive a shaft connected to a pump, converting wave energy to mechanical energy. Computational Fluid Dynamics (CFD) and a small-scale physical model in a one-foot flume were used for proof of concept. For the numerical model, a solid model was constructed using CAD and exported to a commercially available CFD code, Flow-3D®.

Figure 2. Linked Submerged Oscillating Water Column Concept

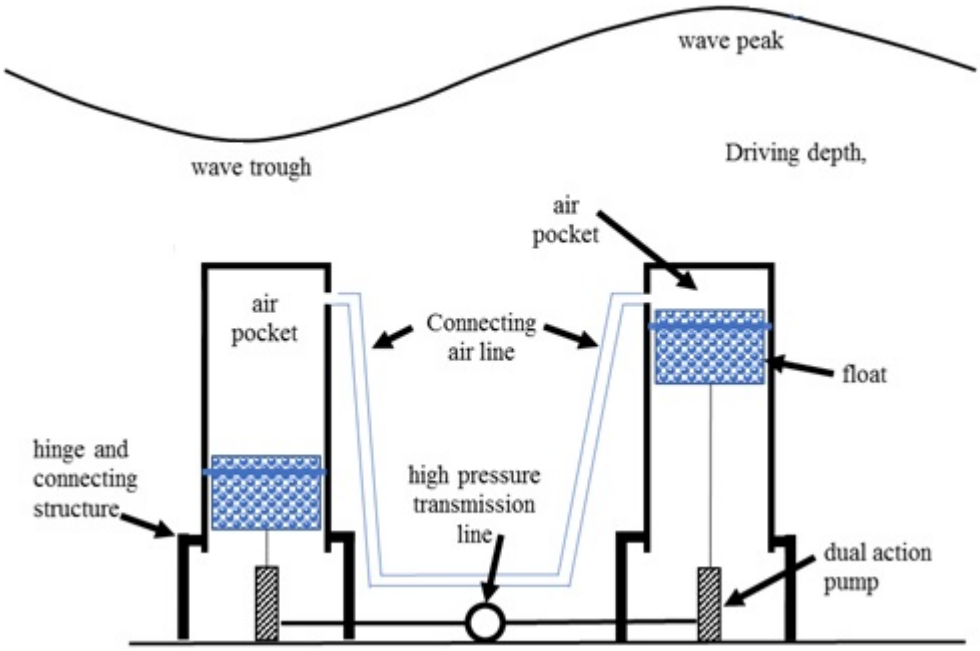

NUMERICAL MODELING

7th International Junior Researcher and Engineer Workshop on Hydraulic Structures, IJREWHS'19, B. HEINER and B. TULLIS (Eds), Report 8, U.S. Bureau of Reclamation, Denver, CO, USA - ISBN 978-0-578-69809-0
https://doi.org/10.26077/85a1-fa31

The numerical method in this study was based on solving the Reynolds-averaged Navier–Stokes (RANS) equations with a finite-volume method. CFD can solve and analyze fluid flow problems based on the Navier-Stokes equations. Continuity and momentum, equations (1) and (2), respectively, govern the motion of the fluid.

$$\frac{\partial}{\partial x}\left(uA_x\right)+\frac{\partial}{\partial y}\left(vA_y\right)+\frac{\partial}{\partial z}\left(wA_z\right)=0 \quad (1)$$

$$\frac{\partial U_i}{\partial t}+\frac{1}{V_F}\left(U_j A_j \frac{\partial U_i}{\partial x_j}\right)=-\frac{1}{\rho}\frac{\partial P'}{\partial x_i}+g_i+f_i \quad (2)$$

The variables *u, v* and *w* are velocities in the x, y, and z directions; V_F is the fluid volume fraction in each cell and can be empty, full, or partially filled with fluid that gives the value of zero, one or between zero and one. A_x, A_y, and A_z shows the fraction of open level in x, y, and z directions; ρ is the density; P' is the pressure, and g_i is the gravitational force. The variable f_i represents the Reynolds stresses (Savage and Johnson, 2001). Turbulence was modeled using the Renormalized Group (RNG) Theory. Since a volume of air is contained in the top region of the SOWSs, the air was modeled as a void region using an adiabatic bubble with an assigned void pressure rather than model it as a second fluid. In essence, Flow-3D treats the airflow as a confined adiabatic bubble. The bubble model evaluates the void region pressure based on the volume by using the isentropic model of expansion/compression in which PV^{γ} is constant.

The grid domain consisted of three linked and one embedded mesh blocks (Figure 3) with over 487,500 total cells. The motion of the floating buoys was modeled as a moving solid. The geometry was constructed from baffles and solids. The total flow domain was greater than four times the wavelength (4λ). Boundary conditions included sidewalls (y-direction) with symmetry boundaries; top boundary (z-max) as a pressure boundary with atmospheric pressure equal to 2116 lbf/ft^2; bottom boundary as a wall; left upstream inlet side (x-min) as a wave boundary; and the downstream (x-max) as an outflow with a non-moving wave absorbing layer (sponge layer) to prevent wave reflections back into the model. Figure 3 shows the solid model imported into the constructed numerical grid. The pipe between the two SOWC cylinders allows air motion as waves pass. The ideal distance between chambers is considered a half of a wavelength, placing the peak of one wave above one cylinder while the trough is simultaneously over the second cylinder. Seventeen different numerical simulations were completed by varying the cylinder height, h (two and three feet); water depth, d (four- eight ft); cylinder diameter, D (constant at 1 foot); wave period, T (1.75 s-3.0 s).; and wavelength, L. Configurations are shown in Table 1 with the results.

Figure 3: SOWC meshing

7th International Junior Researcher and Engineer Workshop on Hydraulic Structures, IJREWHS'19, B. HEINER and B. TULLIS (Eds), Report 8, U.S. Bureau of Reclamation, Denver, CO, USA - ISBN 978-0-578-69809-0
https://doi.org/10.26077/85a1-fa31

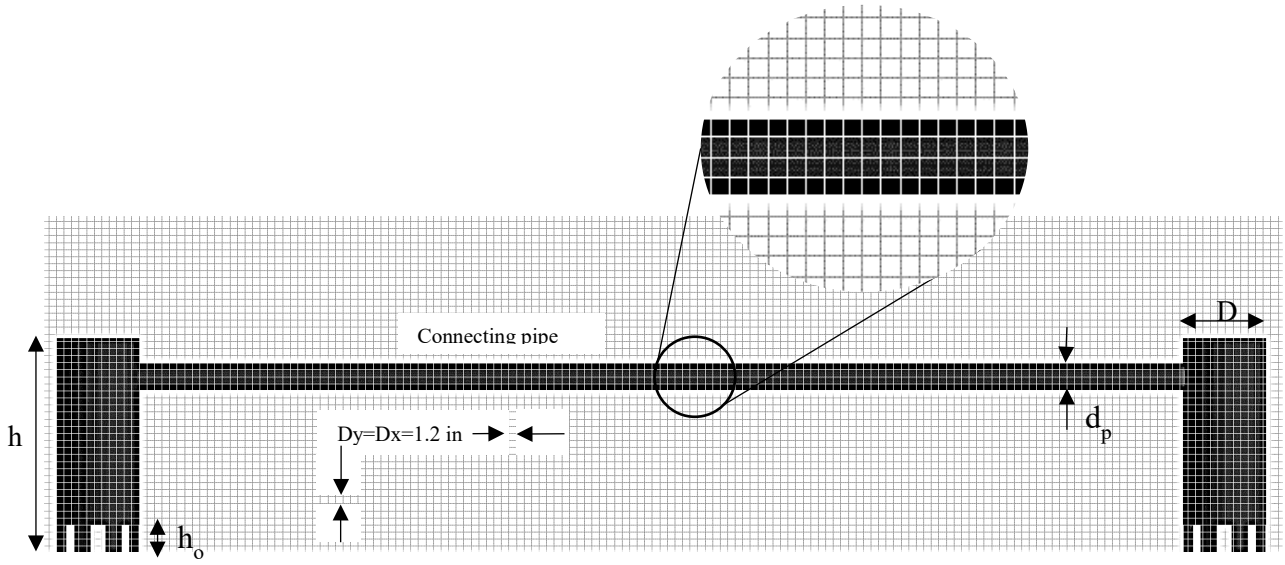

EXPERIMENTAL TESTS

In order to verify the numerical data, a simple physical model was also constructed. The experiments were completed in a one ft wide x 16ft long flume with a maximum depth of one foot. A sinusoidal wave generator is capable of making regular waves with different lengths and heights. To measure the oscillating water surface inside the chambers, a long thin rod was placed in a hole drill in the top of a closed three-inch diameter transparent pipe. A wood buoy was placed inside the cylinder to track the water motion inside as shown (Figure 4a). Two of the cylinders were placed approximately a half of the average wavelength apart and connected by a flexible three-eighth inch hose. The initial air pocket was placed in the SOWC using the flexible hose. The hose allowed air to travel between the SOWCs as the waves moved over the cylinders. Unfortunately, instrumentation for the flume/waves was limited and the results from this study were more qualitative than quantitative. Figure 4b shows one SOWC with the changing water surfaces.

Figure 4: (a) Single SOWC model; (b) water level inside the SOWC columns with waves.

https://doi.org/10.26077/85a1-fa31

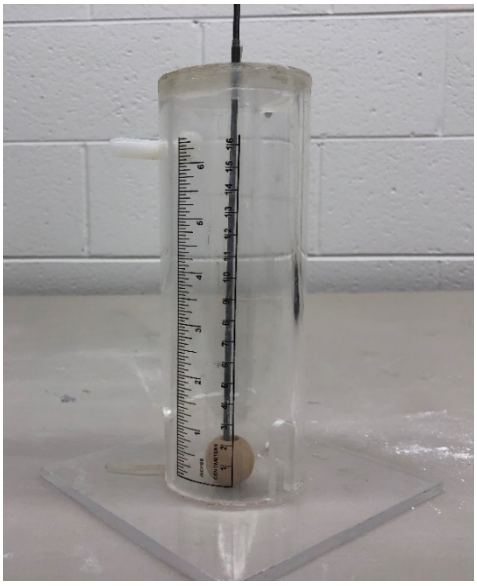

(a)

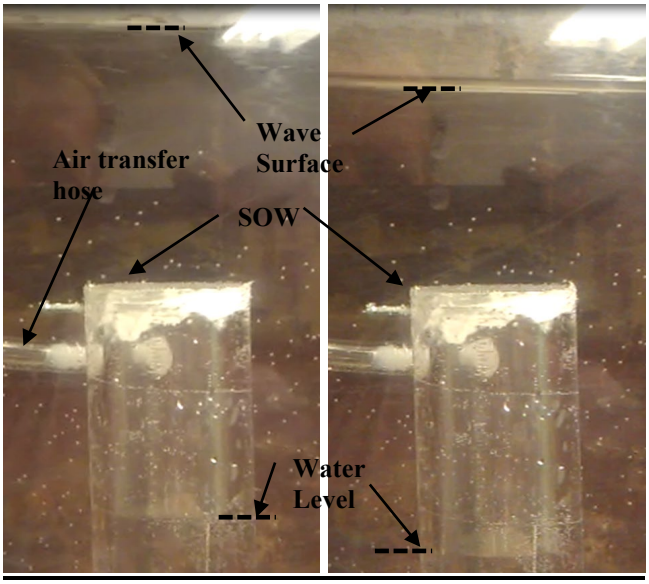

(b)

METHOD AND MATERIAL

In this study, Flow-3D was used for the numerical modeling. The dual 3.4 GHz quad-core computer had 64 GB RAM and took 6 to 24 hrs to complete 30s of simulated flow time. Floating buoys were placed inside and directly above each SOWC to track the water surface movement (Figure 5). The buoys were constrained to only move in the z-direction. After reaching quasi-steady state, the buoys' motion over time was exported and plotted (Figure 6). The difference between adjacent peaks and troughs were calculated and averaged and the efficiency is measured by dividing the relative movement of subsea buoys to floated buoys and defined as:

$$\varepsilon = \frac{a_c}{a_i}$$

where a_c is the amplitude of water surface inside the cylinders and a_i is the amplitude of incident waves. The dimensionless relative depth parameter $\frac{d}{gT^2}$ was calculated to find the relation with efficiency.

Figure 5: Simulated SOWC device

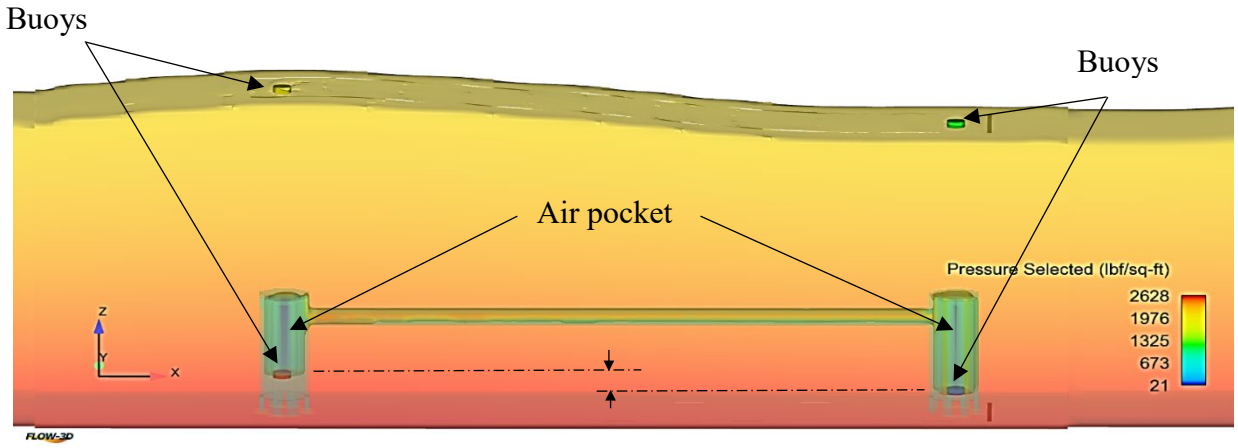

RESULTS AND DISCUSSION

The CFD modeling provided realistic results for the SOWC simulations. By increasing the relative movement of the water surface inside the cylinders to wave height, the efficiency of the device increases. Table 1 indicates generated wave parameters, dimensionless relative depth, and average efficiency of left and right subsea buoys and total average. The diameter of the cylinders was 1 ft and the height was 2 or 3 ft; mentioned in the table 1. Test No#6 in Table 1 has the highest efficiency of 82% and test no#11 has the lowest of 30%. The reason is the relative depth; by increasing the depth the efficiency would decrease which is observable in *Figure 7*. The graph in *Figure 7* indicates the relative depth and total average efficiency of the buoys. It shows a correlation of R^2=0.96 between relative depth and efficiency in the intermediate water depth. According to the definition, 0.05<d/L<0.5 is a intermediate water depth (Sorensen, 2005). The results of Table 1 indicate that the SOWC device is in an intermediate water depth.

Figure 6: Analysis of buoy motion to water surface motion

7th International Junior Researcher and Engineer Workshop on Hydraulic Structures, IJREWHS'19, B. HEINER and B. TULLIS (Eds), Report 8, U.S. Bureau of Reclamation, Denver, CO, USA - ISBN 978-0-578-69809-0
https://doi.org/10.26077/85a1-fa31

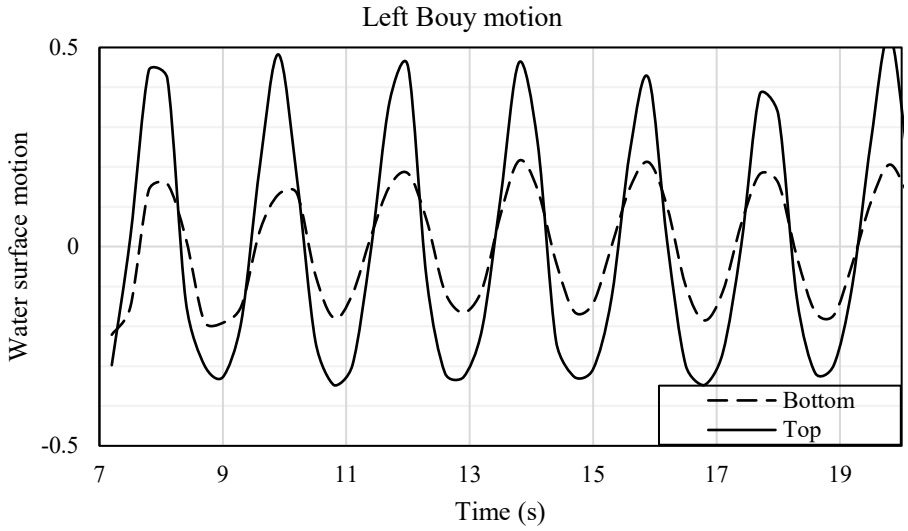

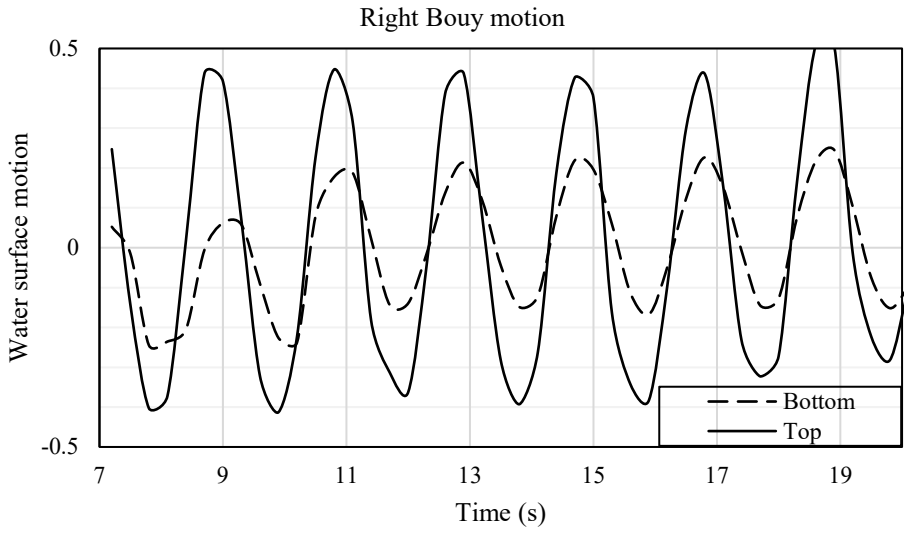

Table 1: Numerical result analysis of the tests

Test No	h	d	T	L (ft)	d/L	d/gT^2	Left Buoy	Right Buoy	ave
1	2	4	1.75	14.69	0.272	0.041	55.3%	58.6%	57.0%
2	2	4	2.00	18.09	0.221	0.031	61.4%	65.2%	63.3%
3	2	4	2.25	21.41	0.187	0.025	65.9%	70.7%	68.3%
4	2	4	2.50	24.64	0.162	0.020	74.6%	75.5%	75.0%
5	2	4	2.75	27.81	0.144	0.016	80.0%	75.6%	77.8%
6	2	4	3.00	30.93	0.129	0.014	85.1%	79.0%	82.1%
7	2	5	2.00	19.03	0.263	0.039	47.6%	51.0%	49.3%
8	2	6	2.00	19.63	0.306	0.047	42.6%	42.5%	42.5%

9	2	7	2.00	19.99	0.350	0.054	39.6%	40.2%	39.9%
10	2	8	2.00	20.21	0.396	0.062	32.8%	31.1%	32.0%
11	3	6	1.75	15.45	0.388	0.061	29.8%	30.2%	30.0%
12	3	6	2.00	19.63	0.306	0.047	41.0%	46.0%	43.5%
13	3	6	2.25	23.83	0.252	0.037	50.6%	53.4%	52.0%
14	3	6	2.50	27.96	0.215	0.030	63.0%	61.0%	62.0%
15	3	6	2.75	32.02	0.187	0.025	70.0%	74.0%	72.0%
16	3	6	3.00	35.99	0.167	0.021	78.0%	82%	80.0%
17	3	8	2.50	29.87	0.268	0.040	52.0%	48.0%	50.0%

Figure 7: Relative depth to efficiency graph

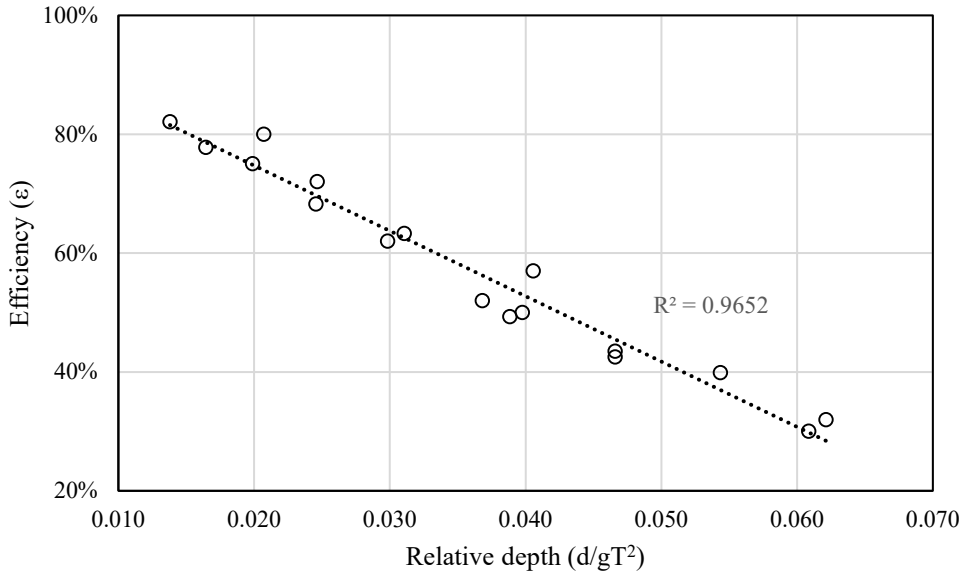

CONCLUSION

In this research, a new conceptual submerged device for capturing the ocean wave energy is proposed. The device consists of two cylinders placed half a wavelength apart to be more efficient. Numerical and experimental results indicated the validity of surface waves generating oscillating motion in SOWCs. Analyzing the numerical results showed that the interior motion can reach up to 80% of the surface motion. Also, the difference of efficiency in this submerged SOWC, is compensable by syncing several SOWC devices and connecting them together. The results show the efficiency in intermediate water depth has a good agreement with relative depth. By increasing the relative depth the efficiency decrease. Based on the analysis, the most efficient location for the device to have higher efficiency is when the relative depth is low and waves height are big, which means the location before waves break ($H/L \geq 1/7$).

Suggested future research would be the experimental tests of more than two SOWCs syncing together and compare the experimental and numerical results. With more than two SOWCs connected, the overall system efficiency, including pumps should be studied.

NOTATION

A_x	fraction of open level in x directions
A_y	fraction of open level in y directions
A_z	fraction of open level in z directions
a_c	amplitude of water surface inside the cylinders
a_i	amplitude of incident waves
d	Water depth
f_i	Reynolds stresses
g	gravity
h	Height of the cylinder
L	Wave length
P’	pressure
T	Wave period
V_F	fluid volume fraction
u	velocities in x direction
v	velocities in y direction
w	velocities in Z direction
ρ	density

REFERENCES

Alamian, R., Shafaghat, R., Miri, S. J., Yazdanshenas, N., & Shakeri, M. (2014). Evaluation of technologies for harvesting wave energy in Caspian Sea. *Renewable and Sustainable Energy Reviews*, *32*, 468-476.

Brekken, T. (2010). Fundamentals of ocean wave energy conversion, modeling, and control. In *2010 IEEE International Symposium on Industrial Electronics* (pp. 3921-3966). IEEE.

Callaway, E. (2007). Energy: to catch a wave. *Nature News*, *450*(7167), 156-159.

Cruz, J. (2007). *Ocean wave energy: current status and future perspectives*. Springer Science & Business Media.

Drew, B., Plummer, A. R., & Sahinkaya, M. N. (2009). A review of wave energy converter technology. Proceedings of the Institution of Mechanical Engineers, Part A: Journal of Power and Energy, 223(8), 887–902. https://doi.org/10.1243/09576509JPE782

Dufera, H. (2016). *PB500, 500 KW Utility-Scale Powerbuoy Project* (No. DOE-OPT-EE0003645). Ocean Power Technologies Inc., Pennington, NJ (United States).

Rhinefrank, K., Schacher, A., Prudell, J., Cruz, J., Jorge, N., Stillinger, C., ... & Yim, S. (2010). Numerical and experimental analysis of a novel wave energy converter. In *ASME 2010 29th International Conference on Ocean, Offshore and Arctic Engineering* (pp. 559-567). American Society of Mechanical Engineers.

Ruellan, M., BenAhmed, H., Multon, B., Josset, C., Babarit, A., & Clement, A. (2010). Design methodology for a SEAREV wave energy converter. *IEEE Transactions on Energy Conversion*, *25*(3), 760-767.

Sorensen, R. M. (2005). Basic coastal engineering (Vol. 10). Springer Science & Business Media.

Valério, D., Beirão, P., & da Costa, J. S. (2007). Optimization of wave energy extraction with the Archimedes Wave Swing. *Ocean Engineering*, *34*(17-18), 2330-2344.

Washington, F. (2019). WAVE ENERGY CONVERSION. The Military Engineer.

Wave, (2019, September 1). Capturing energy from waves with a point absorber buoy, surface attenuator, oscillating water column, or overtopping device. Retrieved from https://tethys.pnnl.gov/technology-type/wave.

Weber, J., Mouwen, F., Parish, A., & Robertson, D. (2009). Wavebob—research & development network and tools in the context of systems engineering. In *Proc. Eighth European Wave and Tidal Energy Conference, Uppsala, Sweden* (pp. 416-420).

7th International Junior Researcher and Engineer Workshop on Hydraulic Structures, IJREWHS'19, B. HEINER and B. TULLIS (Eds), Report 9, U.S. Bureau of Reclamation, Denver, CO, USA - ISBN 978-0-578-69809-0
https://doi.org/10.26077/fw3r-v253

BEYOND FLOODPLAIN ANALYSIS: A MODELER'S EXPERIENCE USING HEC-RAS 2D FOR SPILLWAY ASSESSMENTS AND DESIGNS

Yan WANG
Gannett Fleming, Inc., USA, ywang@gfnet.com
Amanda HESS
Gannett Fleming, Inc., USA, ahess@gfnet.com
Gregory RICHARDS
Gannett Fleming, Inc., USA, grichards@gfnet.com

Abstract: HEC-RAS 5.0 (2D) has been increasingly used by the dam safety community for performing dam breach and other hydraulic analyses since its debut in 2015. While this two-dimensional hydraulic modeling software has wide applications in dam breach analysis and urban flood simulation, its ability to analyze complex multidirectional flow problems can also be used as a design tool for spillways, overtopping protection, and other hydraulic structures. In this manuscript, the authors discussed their experience using HEC-RAS and other two-dimensional hydraulic models to design and assess various hydraulic structures. This includes: 1) sizing spillway outlet channels and assessing the hydraulic adequacy of training dikes, especially where non-linear or super-elevated flow conditions are anticipated; 2) using depth, velocity, and shear stress outputs to design erosion/overtopping protection for vegetated spillways, lined channels, and earthen embankments; 3) designing temporary diversions to facilitate construction within rivers, reservoirs, or other waterways; and 4) identifying and assessing potential failure modes (e.g. erosion and headcutting of vegetated spillways). Insights are shared to help the audience understand when a two-dimensional modeling approach is effective and appropriate.

Keywords: HEC-RAS, Two-dimensional, Hydraulic Models, Hydraulic Structures.

INTRODUCTION

Dam breach and flood inundation analyses have traditionally been performed using one-dimensional (1D) hydraulic models. When developing 1D models, modelers are required to identify the center line of the studied streams/flow area, and to create cross-sections that represent the bathymetry of the streams. One-dimensional models usually require minimal run-time and perform well in situations where the stream is well defined and the flow is mostly one dimensional. However, researchers are aware of 1D models' limitations in simulating flood events where complex terrain, un-defined flow paths, complex ineffective areas, and sharp turns are involved (NORDLÖF 2017, HORRITT and BATES 2002, TAYEFI et al. 2007, ANDERSSON and BATES 1993, TAYE et al.

2007, COOK and MERWADE 2009, VOJINOVIC and TUTULIC 2008). Application of a 1D model in these situations may result in under-estimation of friction losses, inundation extents, and may lead to inaccurate flood dynamics (TAYEFI et al. 2007). Another issue for 1D models is that the simplified kinematic wave method employed by 1D models is unable to account for the downstream backwater effect, especially at river confluences with mild stream slopes (HE at al. 2006, 2008, 2015). Two-dimensional (2D) hydraulic models are considered more suitable for these hydraulic situations.

The main drawbacks of 2D models are long simulation time and high input intensity. Thanks to rapid development of super computers and techniques such as Geographical Information System (GIS) and Light Detection And Ranging (LiDAR), 2D hydraulic models have become more popular. HEC-RAS (Hydraulic Engineering Center River Analysis System) is a hydraulic modeling tool developed by the US Army Corps of Engineers (USACE). The software has been used as the industry-standard in the United States for 1D river systems modeling, flood plain/floodway analyses, dam breach analyses, bridge and culvert analyses, and sediment transport modeling (BRUNNER, 2016). The capability of modeling 2D flow conditions has been incorporated into the HEC-RAS model since Version 5.0. Unlike other readily available 2D hydraulic modeling programs, HEC-RAS 5.0 employed a method that represents the topographical data on a sub-grid level, capturing important terrain features while keeping the computational grid large and computation time short (USACE 2015, CASULLI 2008). The sub-grid information was introduced into the model by developing a stage-volume relationship within each calculation cell and a stage-discharge relationship on each face of the calculation cell. Multiple research has concluded that the sub-grid representation can produce a better flood inundation extent than could be attained by using a non-sub-grid approach and calibrating using the roughness parameter (YU and LANE 2006, YU and LANE 2011, MCMILLAN and BRASINGTON 2007, and CASULLI 2008).

Since the debut of HEC-RAS 5.0, 2D hydraulic models have been widely applied to river system analyses for flood extents determination in various flood plain configurations under various flow conditions. The applications (NEAL et al. 2012, NORDLÖF 2017) mainly focus on dam breach analyses, urban flooding analyses, levee breach analyses, and other flood related topics. Application of HEC-RAS 2D in other fields is rare. HEC-RAS is able to analyze complex multidirectional flow problems and provide geo-spatial information on hydraulic parameters including depth, velocity, and shear stress everywhere within the inundation areas. It can also be used as a design tool for spillways and other hydraulic structures, as well as assisting in erosion control and overtopping protection. In this manuscript, applications of HEC-RAS for design and assessment of various hydraulic structures is discussed. Insights are shared for effective and appropriate application of 2D modeling in hydraulic structure design and assessment.

METHODOLOGY

Model Inputs

The input data required for running a 2D hydraulic model using HEC-RAS includes a terrain grid encapsulating the entire study area, Manning's surface roughness coefficients, boundary conditions, and hydrologic loading conditions such as precipitation/inflow hydrographs/stage hydrographs.

HEC-RAS uses terrain data in the form of a Geo-Tiff or a Grid raster file. Terrain data with various resolutions can be obtained from the USGS National Map Viewer. High resolution LiDAR data are not available in many areas but can be obtained from different State Agencies. High resolution terrain data can also be obtained from survey data. Since HEC-RAS applies the sub-grid terrain method, using high resolution terrain data does not compromise the simulation run time. It is recommended that terrain data with the highest resolution be used in a 2D HEC-RAS model.

Manning's roughness coefficients are assigned based on land cover data. Large scale land cover information can be obtained from the National Land Cover Database (NLCD). State/local government may have land cover data with higher resolutions. User-defined land cover divisions are allowed if more accurate data is available. HEC-RAS uses land cover data in the form of a Geo-Tiff or a Shape file. Manning's roughness coefficients are advised to be assigned according to CHOW's Open Channel (CHOW, 1987).

External boundary conditions applied in 2D HEC-RAS can be set as flow hydrograph, stage hydrograph, rating curve, and normal depth among others. Internal boundary condition lines can also be applied within the 2D calculation mesh and can be connected to one or more cells through the cell face points. Precipitation in the form of direct runoff can also be applied as a boundary condition in 2D HEC-RAS (USACE 2015).

Model Setup

Setting up a 2D HEC-RAS model requires a geometry file, an unsteady flow file, and a plan file. The geometry file needs to be associated with the terrain data and the Manning's Roughness layer. One or multiple 2D calculation areas can be defined in the geometry file as long as the 2D areas are entirely within the extents of the terrain data. Calculation cell sizes need to be defined for each of the defined 2D areas. Selection of cell size affects the accuracy of model results and the model run time. Smaller cell size can be defined within any 2D area where refined results are desired. Break lines can be created within the 2D areas. Calculation cells near the break lines can be enforced so that the cells are aligned with the break lines. Different calculation cell sizes along cells enforced near the break lines can be defined in order to provide a more refined analysis for the area. Boundary conditions are introduced into the model as unsteady flow data. A plan file is a master control file telling the program which geometry file and plan file to use. In a plan file, important 2D parameters include calculation interval, 2D modeling methods, and output controls (USACE 2015).

7th International Junior Researcher and Engineer Workshop on Hydraulic Structures, IJREWHS'19, B. HEINER and B. TULLIS (Eds), Report 9, U.S. Bureau of Reclamation, Denver, CO, USA - ISBN 978-0-578-69809-0
https://doi.org/10.26077/fw3r-v253

Model Outputs and Analysis

HEC-RAS provides multiple types of results which can be used in the design and assessment of hydraulic structures. Depth, velocity, shear stress, stream power, depth-velocity product, and other information for the entire flood inundation area can be obtained at their maximum values or at a specific time step. Time series data for depth and velocity at any point within the inundation area can be retrieved. Profile lines can be created within the 2D areas. Depth, water surface elevation, and velocity along the profile lines at any specific time step can be obtained. Flow hydrograph across the profile lines can also be obtained from the model output.

CASE STUDIES

Case 1

Dam A, located in Pennsylvania, USA, is currently classified as a high hazard structure and the Spillway Design Flood (SDF) is established as the 1/2 Probable Maximum Flood (PMF). The dam owner would like to reduce the hazard classification of Dam A by reducing the height of the structure and the storage volume retained by the structure by partially breaching the top of dam to the current sediment pool level. Aerial imagery of the existing dam is presented in Fig. 1. A two-dimensional HEC-RAS hydraulic model of the proposed dam was developed to evaluate embankment protection design. The simulated velocity field at the downstream face of the proposed dam embankment was used for riprap sizing.

Fig. 1 – Aerial Imagery of the Existing Dam A

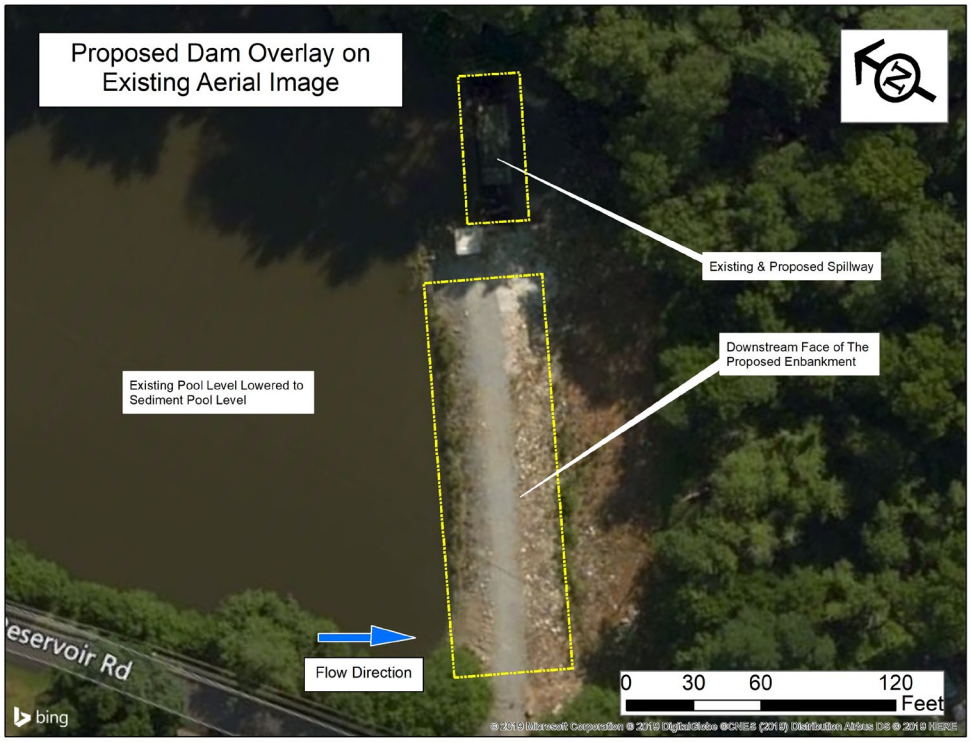

The proposed dam embankment was drafted in AutoCAD and brought in HEC-RAS as the proposed

2D surface. The roughness coefficients are defined as 0.03 for stream bed, 0.013 for the spillway, 0.06 for downstream slope of the dam embankment, and 0.045 for other parts of the 2D area. Other information regarding model setup is listed in Table 1.

The model results show that for the design flood, the velocity ranges from 4.0 feet per second (fps) to 11.7 fps at the downstream slope of the dam embankment. The natural high ground and the geometry of the reservoir result in a non-uniform velocity distribution along the length of the embankment. The velocity field of the entire two-dimensional hydraulic model is presented in Fig. 2. The simulated velocity field on the downstream slope of the embankment allowed a detailed analysis of the distribution and the percentage of area within each velocity range. A cost-effective design for riprap selection and layout was selected based on the 2D results.

Fig. 2 – Velocity Field of Embankment Downstream Slope

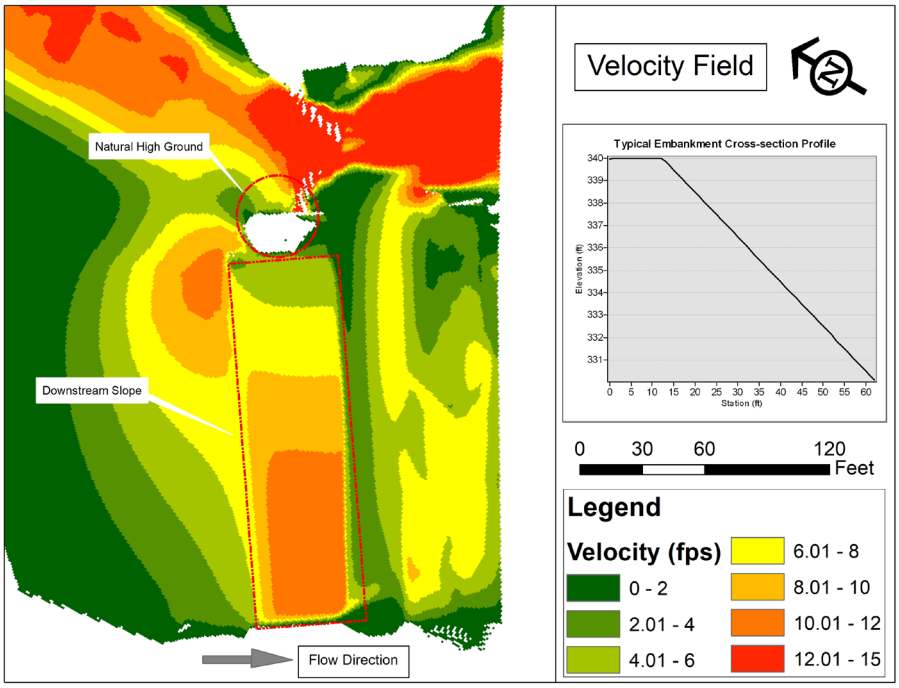

Case 2

Dam B is an earthen embankment dam with one riser structure and an auxiliary spillway located in Pennsylvania, USA. The auxiliary spillway consists of a horseshoe-shaped embankment/weir at the left dam abutment. The spillway channel has encountered significant erosion during large spillway flow events in 1975 and in 2011. Aerial imagery of the spillway exit channel is presented in Fig. 3.

Fig. 3 – Aerial Imagery of the Existing Dam B

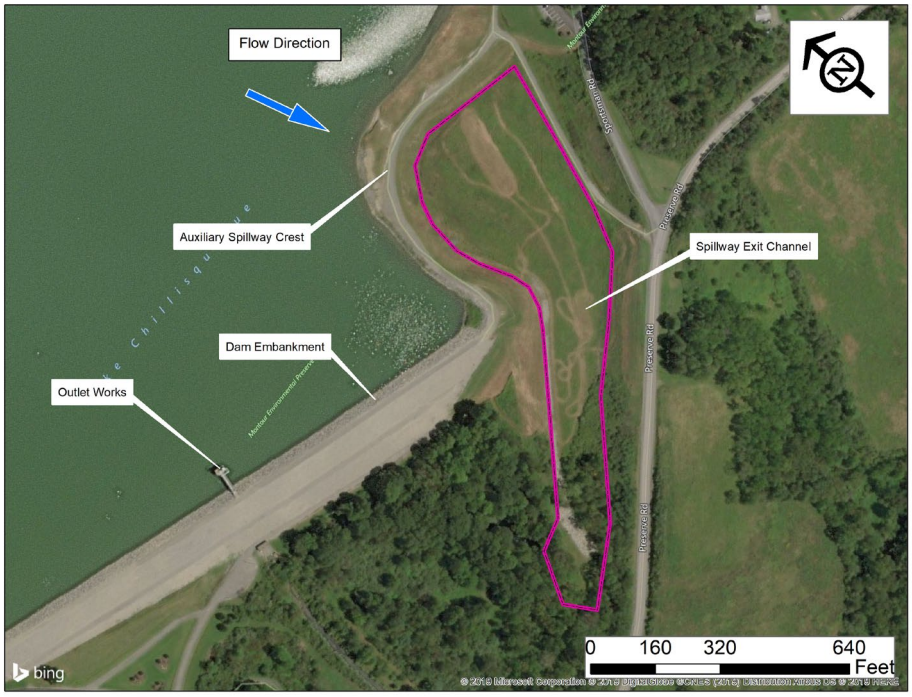

A 2D hydraulic model was developed to analyze the existing spillway and the exit channel and to assist in repair alternative selection. The model evaluated the velocity patterns in the spillway for a range of discharges up to the approximate spillway capacity discharge of 25,000 cfs. Detailed survey data was used to represent the 2D surface. The roughness coefficients are defined as 0.045 for the vegetated portion of the spillway exit channel, 0.055 for the rock-lined portion, 0.015 for paved areas, and 0.12 for forested areas. Break lines were added into the 2D extents to allow more refined cell sizes in desired areas. Other information regarding model setup is included in Table 1.

The model results indicate that the highest velocity was observed on the right edge of the spillway exit channel. The modeling results agree with the field observation of severe erosion near the same location after a large storm event. The simulated flow velocities within a large portion of the spillway exit channel exceed 17 fps, which indicates that the existing spillway channel is susceptible to severe erosion and that spillway improvement is needed to reduce/stop erosion. The velocity field of the entire 2D hydraulic model is presented in Fig. 4. The 2D modeling results show that significant velocity increases were caused by a flow contraction approximately 400 feet downstream of the spillway crest and an abrupt increase in channel slope approximately 2,000 feet downstream of the spillway crest. Due to steep channel slope, velocity within the exit channel is not likely to be affected by downstream backwater. The profile of the exit channel center line is also presented in Fig. 4. These findings suggest possibly moving the existing spillway to the flow contraction section and re-sloping the exit channel. Several spillway improvement alternatives were designed based on the results from the 2D analysis. Other factors such as cost were included in the final selection of repair design.

Fig. 4 – Velocity Field of Spillway Exit Channel

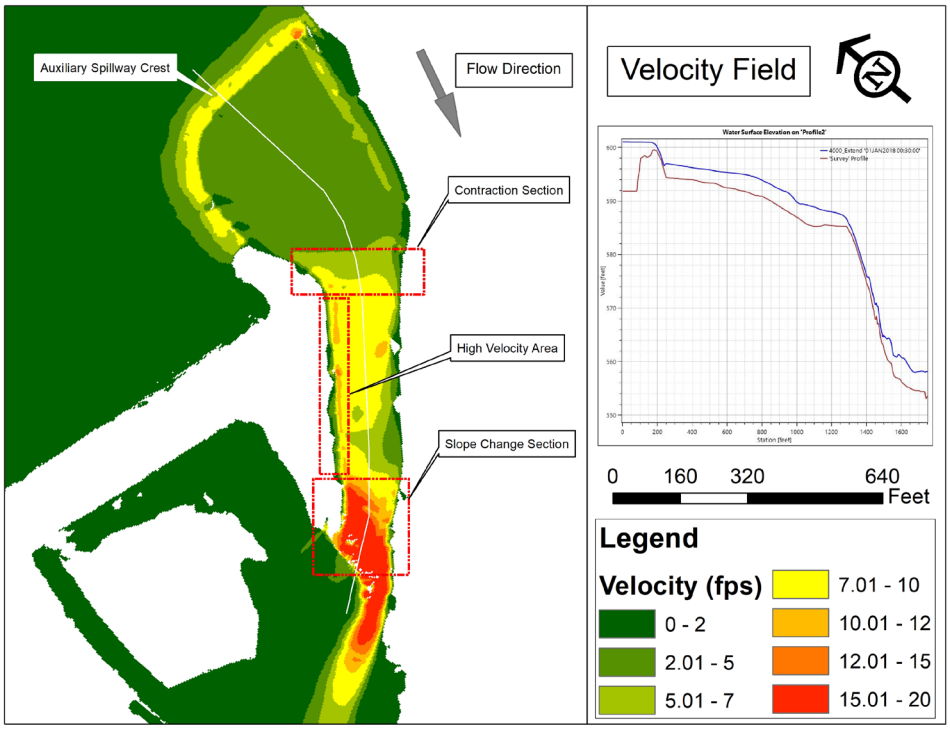

Case 3

A water company was planning to build a new water intake facility including intake, outfall, transition chamber, raw water and finished water pipeline, and other supporting facilities. In order to construct the facility, a cofferdam and a full-width causeway were proposed. The construction schedule indicated that the cofferdam would be used in phase 1 (summer), both the cofferdam and the causeway would be used in phase 2 (fall), and the cofferdam would be removed while the causeway remained in phase 3 (winter). Aerial imagery of the proposed project site is presented in Fig. 5. In order to determine erosion protection measures, a 2D hydraulic model of the project site was created to analyze the reasonably anticipated impact of the temporary causeway and cofferdam on river flow conditions.

Fig. 5 – Aerial Imagery of Project Site for Case 3

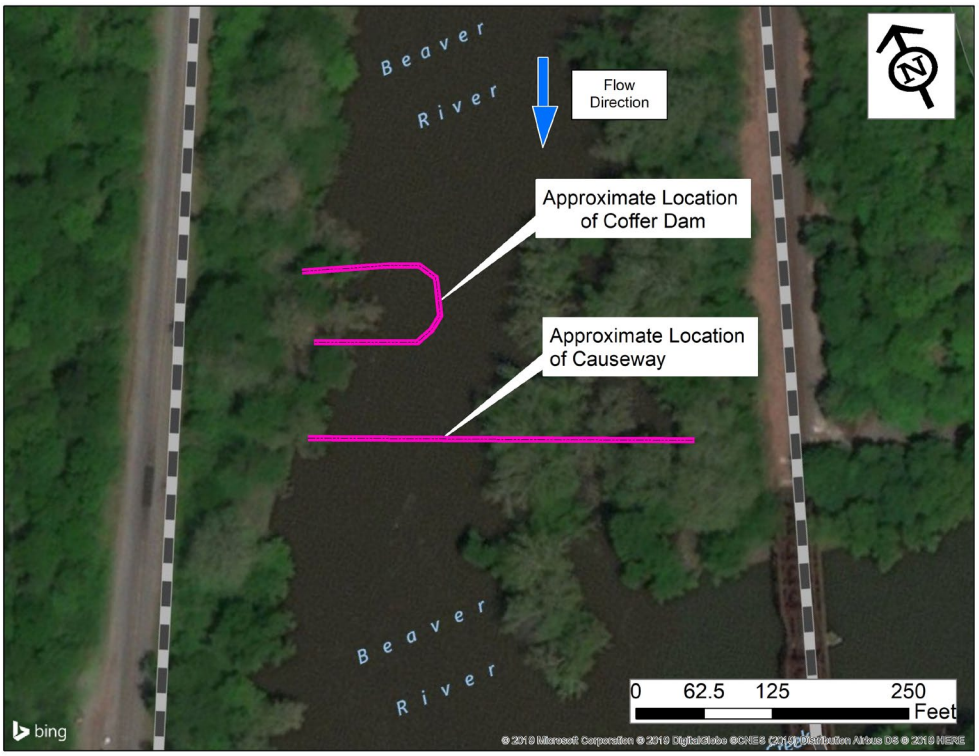

Both the cofferdam and the causeway were modeled as internal connections. Four different scenarios were analyzed: existing condition, coffer dam only, causeway only, and cofferdam and causeway. Average seasonal flow conditions were estimated and were applied to different scenarios according to the construction timeline. The roughness coefficients are defined as 0.03 for stream bed and 0.1 for forested areas. Other information regarding model setup is listed in Table 1.

Simulation results indicated that the most severe riverbed and bank scour potential was observed when both the causeway and cofferdam are installed in the river. The highest water surface velocities within the main river channel, adjacent to the cofferdam structure, are approximately 13 fps. The velocity fields simulated under the four scenarios are presented in Fig. 6. Scour protection was selected based on the highest modeled velocity and was installed in the form of cable concrete mats over the high flow velocity areas identified in the model.

Fig. 6 – Velocity Field of River Diversion Flows

7th International Junior Researcher and Engineer Workshop on Hydraulic Structures, IJREWHS'19, B. HEINER and B. TULLIS (Eds), Report 9, U.S. Bureau of Reclamation, Denver, CO, USA - ISBN 978-0-578-69809-0
https://doi.org/10.26077/fw3r-v253

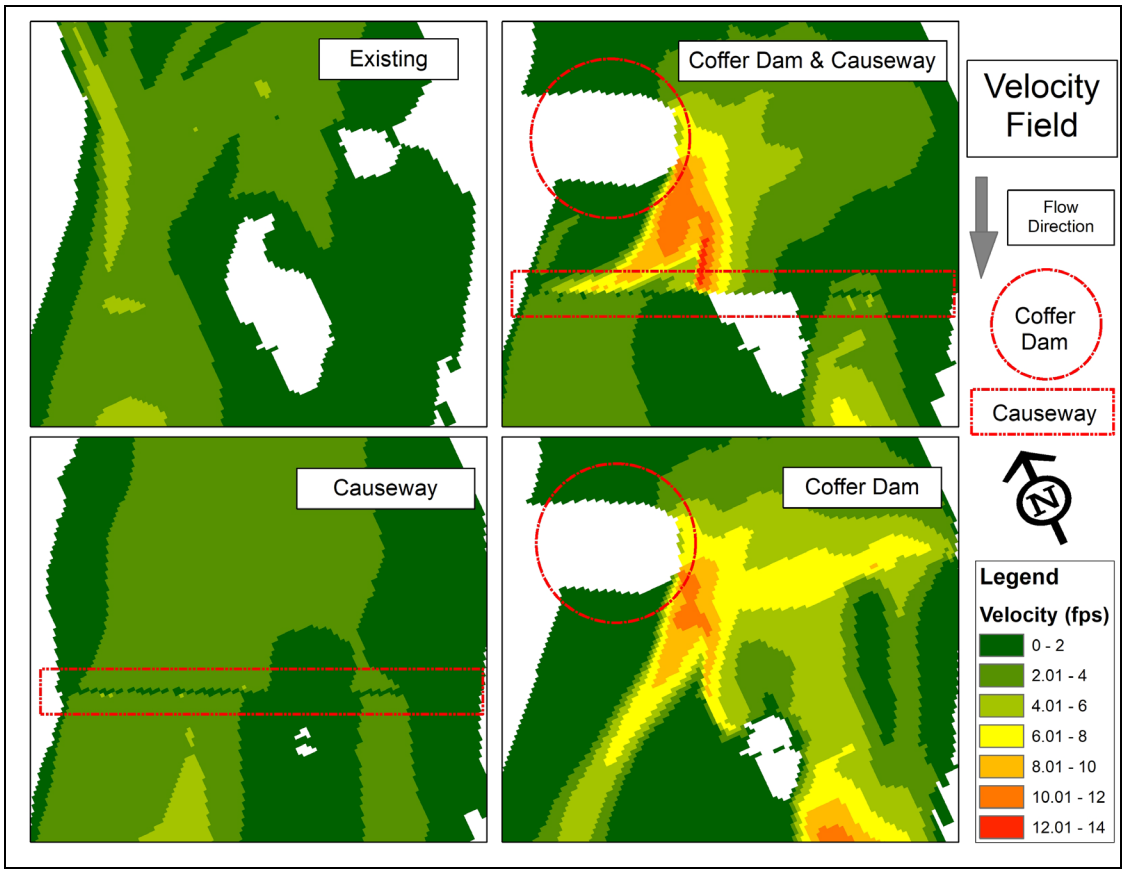

Table 1 – Two-Dimensional Hydraulic Model Setup

Case	Terrain Resolution (feet)	2D Grid Resolution (feet)	Computation Interval (s)	Hydrologic Loading
(1)	(2)	(3)	(4)	(5)
Case 1	1.5	1.5	0.1	100-year
Case 2	1.0	2.0 & 4.0	0.5-varied	A range of flows
Case 3	6.0	3.0	0.2	A range of flows

DISCUSSION

As described in this manuscript, the authors used 2D hydraulic models to evaluate various hydraulic structures. With the help of the simulated velocity and depth grids from a 2D model: 1) slope protection measures were determined; 2) existing spillway deficiencies in terms of capacity and erodibility were identified; and 3) hydraulic performance, overtopping flood event, and erosion control measures of temporary in-stream structures were evaluated and analyzed.

Most of these analyses can be done using a 1D model. However, there are several advantages of using a 2D model in these applications.

- 2D models use a digital terrain model that captures all available details in ground elevation. 1D models use cross-sections to represent the channel geometry. The longer the distance between two cross-sections, the more terrain information loss is expected. In cases where the

spillway channel surface is not uniform and smooth, losing terrain details may significantly affect model results.

- 2D models can more accurately simulate eddies, vortices, super elevation, and other complex flow conditions. It is known that 1D models are not good at simulating channels with bends and sudden changes in cross-section geometries. Using a 2D model can provide more accurate results in channels with irregular shapes.
- 2D models are more efficient in simulating in-stream structures that have irregular shape and orientation. With care, in-stream structures can be simulated as in-line structures in 1D models, but with 2D models, in-stream structures can be included within the 2D calculation area regardless of the shape and orientation.
- 2D models generate result fields, meaning the results are available at every cell within the flooded area. With output presented in such detail, it is easier to identify possible hotspots in small local areas and ensure that the design meets the requirement of the worst-case scenario.

Ideally, flow over a structure with a three-dimensional (3D) configuration is best simulated using a 3D computational fluid dynamics (CFD) model. However, CFD models are usually more expensive and the model run time is significant compared to 2D models. CFD is definitely needed for analyzing flow conditions where vertical movement of water is severe, such as flow over a labyrinth weir or a stepped spillway. However, in cases where the vertical movement of water flow is significantly less prominent than the horizontal movement, a 2D model can be used as an alternative. A comparison of flow simulation was not performed between a 2D and 3D model in this study. More analyses and comparison with physical models are needed to quantify performances of a 2D model in simulating flow conditions for 3D hydraulic structures.

REFERENCES

ANDERSSON, M. and BATES, P. (1993). "A Two-Dimensional Finite-Element Model for River Flow Inundation." Proceedings: Mathematical and Physical Sciences, 440(1909):481-491.

BETSHOLTZ, A., and NORDLÖF, B. (2017). "Potentials and limitations of 1D, 2D and coupled 1D-2D flood modelling in HEC-RAS." Master Thesis. Division of Water Resources Engineering, Department of Building and Environmental Technology, Lund University.

BRUNNER, G. W. (2016). "HEC-RAS River Analysis System : User's Manual." (February).

CASULLI, V. (2008). "A high-resolution wetting and drying algorithm for free-surface hydrodynamics." (August 2008):391-408.

CHOW, V. T. (1959). "Open-Channel Hydraulics." McGraw Hill.

COOK, A. and MERWADE, V. (2009). “Effect of topographic data, geometric configuration and modeling approach on flood inundation mapping." Journal of Hydrology, 377(1-2):131-142.

HE, H., YU, Q., ZHOU, J., TIAN, Y. Q., & CHEN, R. F. (2008). “Modelling complex flood flow evolution

in the middle Yellow River basin, China." Journal of hydrology, *353*(1-2), 76-92.

HE, H., ZHOU, J., YU, Q., TIAN, Y. Q., & CHEN, R. F. (2007). "Flood frequency and routing processes at a confluence of the middle Yellow River in China." River Research and Applications, *23*(4), 407-427.

HE, H., TIAN, Y. Q., MU, X., ZHOU, J., Li, Z., CHENG, N., ... & OEURNG, C. (2015). "Confluent flow impacts of flood extremes in the middle Yellow River." Quaternary international, 380, 382-390.

HORRITT, M. and BATES, P. (2002). "Evaluation of 1D and 2D numerical models for predicting river flood inundation." Journal of Hydrology, 268(1-4):87-99.

MCMILLAN, H. K. and BRASINGTON, J. (2007). "Reduced complexity strategies for modelling urban floodplain inundation." Geomorphology, 90(3-4):226-243.

NEAL, J., SCHUMANN, G., and BATES, P. (2012). "A subgrid channel model for simulating river hydraulics and floodplain inundation over large and data sparse areas. " Water Resources Research, 48(11):1-16.

TAYEFI, V., LANE, S., HARDY, R., and YU, D. (2007). "A comparison of one- and two-dimensional approaches to modeling flood inundation over complex upland floodplain." Hydrological Processes, 21(May 2007):3190-3202.

USACE (2015). "HEC-RAS River Analysis System 2D Modeling User ' s Manual." (April).

USACE (2016). "HEC-RAS 5.0.6 Release Notes."

VOJINOVIC, Z. and TUTULIC, D. (2008). "On the use of 1D and coupled 1D-2D modeling approaches for assessment of flood damage in urban areas." Urban Water Journal, 6(3, September 2009):183-199.

YU, D. (2005). "Diffusion-based modelling of flood inundation over complex floodplains. "

YU, D. and LANE, S. N. (2006). "Urban fluvial flood modelling using a two-dimensional diffusion-wave treatment, part 1: Mesh resolution effects." Hydrological Processes, 20(7):1541-1565.

YU, D. and LANE, S. N. (2011). "Interactions between subgrid-scale resolution, feature representation and grid-scale resolution in flood inundation modelling." Hydrological Processes, 25(1):36-53.

7th International Junior Researcher and Engineer Workshop on Hydraulic Structures, IJREWHS'19, B. HEINER and B. TULLIS (Eds), Report 10, U.S. Bureau of Reclamation, Denver, CO, USA - ISBN 978-0-578-69809-0
https://doi.org/10.26077/rhjg-qj31

COMPARISON OF MODELLING APPROACHES FOR DEVELOPMENT OF DISCHARGE RATING CURVES FOR SPILLWAY/BRIDGE COMBINATIONS

Nathan Young, E.I.T.
Schnabel Engineering, USA, nyoung@schnabel-eng.com

ABSTRACT

When estimating spillway discharge rating curves, engineers can use a variety of methods such as empirical equations, one- (1D) or two-dimensional (2D) hydraulic computer models, or a combination thereof; however, conservative assumptions are often applied to such methods. The use of three-dimensional (3D) computational fluid dynamics (CFD) models is an alternative modelling approach that can often better estimate spillway discharge rating curves, especially for complex flow situations. In this study, the results of 3D CFD models are compared to estimates of spillway discharge rating curves developed with a combination of empirical equations and other hydraulic computer models for spillway/bridge combinations. It is shown that results typically agree for lower order methods that share approximations whereas higher order models can produce significantly different results. It is recommended that careful consideration be given to governing equations and effectiveness of representing site geometries when selecting which method(s) to use to develop a discharge rating curve, especially when complex site conditions may be better captured with a higher order model.

Keywords: Spillway, modelling, rating curve, CFD

INTRODUCTION

Knowledge of a dam's spillway capacity – the maximum discharge a spillway can pass with the reservoir at its maximum level – is of great importance to the practicing hydraulic engineer. The associated stage and discharge relationship leading to the spillway capacity and beyond comprises the spillway discharge rating curve and is necessary when estimating reservoir levels for various hydrologic events. A variety of methods are available to develop a discharge rating curve such as empirical equations (e.g., unsubmerged/submerged weir equation), one- (1D) or two-dimensional (2D) hydraulic computer models based on conservation of energy and momentum equations (e.g., Federal Highway Administration's HY-8 Culvert Analysis Program, United States Army Corps of Engineers Hydrologic Engineering Center River Analysis System [HEC-RAS]), or a combination thereof. These methods may not always accurately reflect site-specific geometry or complex hydraulic conditions, such as a spillway in close proximity to a bridge with confining openings. To account for uncertainty with these methods, conservative assumptions are often applied such as selecting a reduced discharge coefficient or an increased tailwater elevation. The use of detailed, three-dimensional (3D) computational fluid dynamics (CFD) models (e.g., Flow 3D) is becoming

more common and can provide an alternate approach to better estimate discharge rating curves for spillways while reducing uncertainty for complex situations, such as converging channels, spillways combined with bridges or culverts, or submergence.

While much research has been conducted on comparing various modelling techniques, little information was found regarding modelling of the type of spillways common in Delaware that are often subject to tailwater submergence and are in close proximity to bridges. Therefore, several modelling techniques, including empirical equations and hydraulic computer models, were used to develop and compare spillway discharge rating curves for multiple spillways in Delaware. Based on these comparisons, recommendations are made as to when it may be appropriate to employ a more complex modelling approach.

BACKGROUND

The COLORADO WATER CONSERVATION BOARD (2006) (CWCB) provided an overview of 2D hydraulic computer modelling in which it stated that the defining assumption for 1D models – that only streamwise forces, velocities, and variations are significant while those in the transverse direction are negligible – does not apply to 2D models. Rather, 2D modelling includes computation of transverse components, therefore providing advantages compared to 1D models. The CWCB tabulated differences between the two modelling approaches, which are shown here as Table 1. Furthermore, the CWCB listed factors to consider when selecting a 1D or 2D hydraulic computer model including the nature of the watercourse, required accuracy, experience of the modeller with the technique, and availability of site specific or physical hydraulic model data.

Table 1 – Differences between One-Dimensional and Two-Dimensional Modelling (COLORADO WATER CONSERVATION BOARD 2006)

Property or Factor	One-Dimensional Modelling	Two-Dimensional Modelling
Flow direction	Prescribed (streamwise)	Computed
Transverse velocity and momentum	Neglected	Computed
Vertical velocity and momentum	Neglected	Neglected
Velocity averaged over	Cross sectional area	Depth at a point
Transverse velocity distribution	Assumed proportional to conveyance	Computed
Transverse variations in water surface	Neglected	Computed
Vertical variance	Neglected	Neglected
Unsteady flow routing	Can be included	Can be included

TOOMBES and CHANSON (2011) discussed limitations of hydraulic computer models, specifically how conservation of momentum and energy are approximated in several software packages. Common numerical approximations in 1D models that the authors discussed were: assumed small channel grades, use of empirical methods to estimate friction losses (e.g., Manning's coefficient), assumed gradually varied flow (steady state), and inability to accommodate two boundary conditions at the

same boundary (unsteady) (e.g., supercritical flow). For 2D models, numerical approximations included: horizontal length scale assumed to be significantly greater than the vertical scale (vertical velocities are negligible) and estimations of forces acting on each fluid component (e.g., shear stress, bed friction). 3D models were stated to remove many limitations related to 1D and 2D models at the expense of increasing complexity and required computations; however, 3D models allow compressible fluids, multi-phase flow, and other effects to be investigated.

TOOMBES and CHANSON (2011) continued their study by verifying software output with two physical hydraulic models: a weir experiment and an open channel flow (hydraulic jump) experiment. For the weir experiment, it was shown that steady HEC-RAS (1D) achieved a good match to the physical hydraulic model data for a low-flow scenario but differed significantly for a high-flow scenario. Flow 3D achieved an excellent match to the physical hydraulic model data for both scenarios of the weir experiment. For the open channel flow experiment, steady HEC-RAS (1D) achieved good agreement with the measured jump location but showed the jump as an instantaneous transition between cross sections, that is the development length was not determined. Similar to the weir experiment, Flow 3D achieved excellent agreement with the physical hydraulic model data of the open channel flow experiment. The authors advised that modellers should study the software documentation to understand its limitations and required approximations, and perform a "reality check" to verify that hydraulic computer model results are reasonable.

RAO et al. (2017) paralleled the work of TOOMBES and CHANSON (2011) by testing several computer programs – including HY-8, HEC-RAS 1D (steady and unsteady), and Flow 3D – to predict the magnitude and location of the hydraulic jump for a similar geometry and flow condition. Differences between the experiments of RAO et al. and TOOMBES and CHANSON were the channel length (15.24 m instead of 12 m), upstream depth (0.04 m instead of 0.062 m), and channel slope (0.012 instead of 0.028). Comparisons of software output with experimental data were as follows:

- HY-8 predicted greater headwater and a more upstream jump location
- Steady and unsteady HEC-RAS predicted a water surface that compared well to the physical hydraulic model data, but the jump occurred more upstream
- Flow 3D also predicted a water surface that compared well, but the jump occurred more downstream and varied per time step

The authors cautioned that while some computer models produce convincing animations and color gradients in great detail, they should be chosen with care and results should be critically interpreted.

SCHNABEL (2015) assessed several alternative modelling approaches for a spillway in Delaware that was subject to tailwater submergence and in close proximity to downstream bridges. Among the

alternative modelling approaches studied, a 3D CFD model was developed to compare the estimated spillway discharge rating curve to the results of an unsteady HEC-RAS 1D model. Results indicated that the discharge rating curve developed with HEC-RAS was acceptable but more conservative (lower capacity) than the 3D CFD model. Possible contributing factors were identified as selection of model elements to represent the spillway and adjacent areas in HEC-RAS, challenges achieving model stability, model interpolation techniques, and computed tailwater submergence. SCHNABEL recommended employing 3D CFD for dams where spillway capacity was of concern as costly rehabilitation efforts might be avoided by acquiring a refined discharge rating curve.

METHOD

The focus of this study was to test several methods to develop and compare spillway discharge rating curves for spillway/bridge combinations common in Delaware. The author endeavoured to use best modelling practices such as sufficient grid refinement, selection of appropriate empirical coefficients, changes of default model numerics, achievement of model stability, etc. No measured hydraulic data was available to verify the results of modelling techniques; therefore, comparisons were limited among employed methods. The following methods were selected for use:

1. Weir Equation and HY-8 Combination: the culvert modelling software HY-8 v7.5 (FHWA 2016) was used to compute the headwater elevations and flow profiles at bridges downstream of investigated spillways. The weir equation shown in Eqn. 1 was used to estimate weir flow with weir coefficients, *C*, and methods to account for submergence effects taken from BRATER and KING (1976). Weir tailwater elevations were assumed to equal the bridge headwater elevations.

$$Q = Q_1 \times \frac{Q}{Q_1} \text{ where } Q_1 = CLH_1^{1.5} = CH_1^n \text{ and } \frac{Q}{Q_1} = f\left(\left(\frac{H_2}{H_1}\right)^n\right) \quad (1)$$

2. HEC-RAS 1D: steady HEC-RAS 1D v5.0.7 (USACE 2016) was used to solve conservation of energy for sites of interest while accounting for energy losses from friction and contraction/expansion effects. Terrains developed with computer aided design (CAD) and geographic information systems (GIS) were represented with a series of cross sections. Weirs were modelled using inline structure elements and bridges were modelled using bridge elements.
3. HEC-RAS 2D: unsteady HEC-RAS 2D v5.0.7 (USACE 2016) was used to solve the depth-averaged St. Venant equations using a grid system to represent the underlying terrain, as developed with CAD and GIS. Spillways and bridges were modelled using SA/2D Area Connections with bridge openings represented as culverts per limitations of the software.
4. Flow 3D: Flow 3D v12.0 (FLOW SCIENCE 2019), a commercially available CFD software, was used to solve the 3D, transient Navier-Stokes equations with the volume of fluid (VOF) method. The VOF method allowed the interface between the fluid and air to be sharp without using a very fine mesh, lending itself to reduced calculations compared to other CFD codes.

Additionally, the program provided 3D flow fields not available in lower order models. The spillway geometries and surrounding terrains were represented with solids in stereolithographic (STL) format developed with CAD and SketchUp.

All tested methods used topographic information and structure data provided by the Delaware Department of Transportation (DelDOT) and Department of Natural Resources and Environmental Control (DNREC). Two sites were investigated for this study, designated as Site 1 and Site 2 as shown in Fig. 1. Site 1 consisted of a semi-circular sheet pile drop structure that discharged outflows through two downstream bridges, the first consisting of a single rectangular opening and the second consisting of three arched openings. Site 2 consisted of a primary linear weir and auxiliary linear weirs to either side that allowed flow to plunge into a rectangular channel and pass through a single rectangular bridge opening.

Fig. 1 – Modelled Spillways: (a) Site 1 and (b) Site 2 (Photos courtesy of Schnabel Engineering)

For all tested methods, the upstream boundary condition (BC) of Site 1 was specified as a volume flow rate while the upstream BC of Site 2 was specified as a fluid elevation to represent the associated reservoir level. The downstream BCs for both sites were modelled with rating curves developed in previous studies that accounted for tailwater. Manning's coefficients were taken from CHOW (1959) to account for friction losses in the channel and surrounding floodplain. Viscous flow in the Flow 3D models was included with the renormalized group (RNG) turbulence model. Selection of this turbulence model was based on guidance from FLOW SCIENCE (2019) that the RNG model was the most robust turbulence closure scheme available. Model numerics were adjusted from their defaults based on the author's experience; one such change was the use of the full momentum (St. Venant) equations for the HEC-RAS 2D model.

Cross sections used in the HEC-RAS 1D models were located approximately 50 ft and 20 ft apart for Sites 1 and 2, respectively. HEC-RAS 2D models included total cell counts of approximately 39,900 and 11,400 for Sites 1 and 2, respectively, with refinement and grid face alignment at structures. For

the Flow 3D models, nested meshes were used with refined mesh blocks located at areas of special interest (e.g., weir crest, downstream apron); total cell counts were 24.4 million and 4.3 million for Sites 1 and 2, respectively.

RESULTS AND DISCUSSION

Site 1

The spillway discharge rating curves for Site 1 were developed to an elevation approximately 9 ft above normal pool using the investigated methods. Only three flow rates were modelled with Flow 3D for comparison as simulations required great lengths of time. Populating the computed discharge rating curve with additional data points was not feasible. The required effort to develop a discharge rating curve with each tested method varied from least effort required to most effort required as follows: weir equation and HY-8 combination, HEC-RAS 1D, HEC-RAS 2D, and lastly Flow 3D. Select graphical output for the employed methods are presented in Fig. 2 and the developed spillway discharge rating curves are presented in Fig. 3. An inset table is included in Fig. 3 that summarizes relative error among Flow 3D results and the other tested methods. Relative errors were calculated with Eqn. 2.

$$Relative\ Error = \frac{Flow\ 3D - Method}{Method} \times 100\% \quad (2)$$

Fig. 2 – Site 1 Select Graphical Output: (a) HEC-RAS 1D, (b) HEC-RAS 2D, and (c) Flow 3D

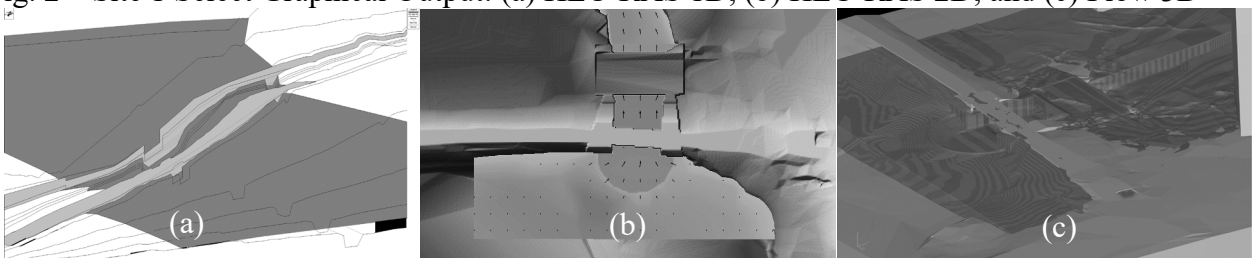

Fig. 3 – Site 1 Spillway Discharge Rating Curve

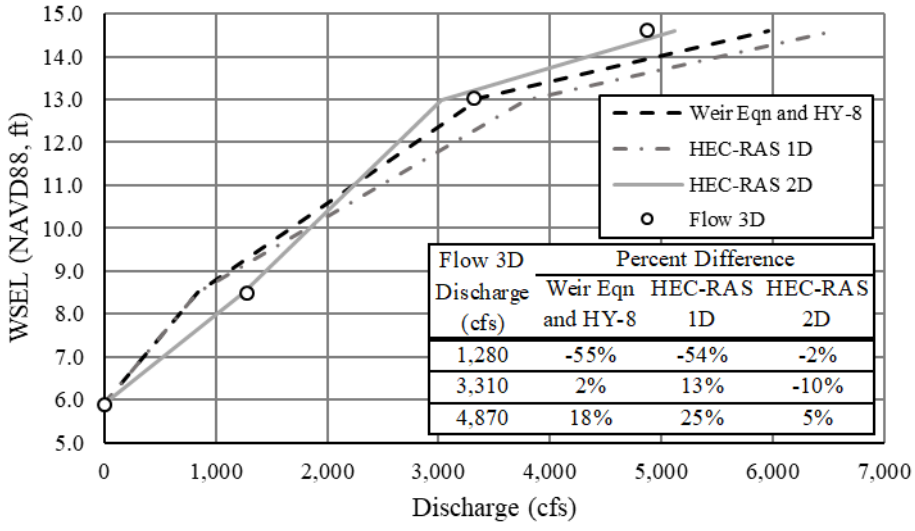

Flow 3D Discharge (cfs)	Percent Difference		
	Weir Eqn and HY-8	HEC-RAS 1D	HEC-RAS 2D
1,280	-55%	-54%	-2%
3,310	2%	13%	-10%
4,870	18%	25%	5%

As shown in Fig. 3, the weir equation and HY-8 combination tended to produce lower discharges up to approximately EL 13.0 as compared to Flow 3D; however, for reservoir levels greater than this, the weir equation and HY-8 combination estimated greater discharges than Flow 3D. Similar results occurred for the HEC-RAS 1D model with greater differences than those of the weir equation and HY-8 combination. HEC-RAS 2D showed relatively good agreement with Flow 3D for its three tested flow rates.

Site 2

The spillway discharge rating curves for Site 2 were developed to an elevation approximately 9 ft above normal pool. Four upstream reservoir levels were tested with Flow 3D as simulation times were less than those for Site 1, largely due to the fewer number of cells. The required effort to develop a discharge rating curve for Site 2 varied in the same manner as Site 1. Select graphical output for Site 2 are presented in Fig. 4 and the developed spillway discharge rating curves are presented in Fig. 5. An inset table summarizing relative errors among Flow 3D and the other tested methods, calculated with Eqn. 2, is included in Fig. 5.

Fig. 4 – Site 2 Select Graphical Output: (a) HEC-RAS 1D, (b) HEC-RAS 2D, and (c) Flow 3D

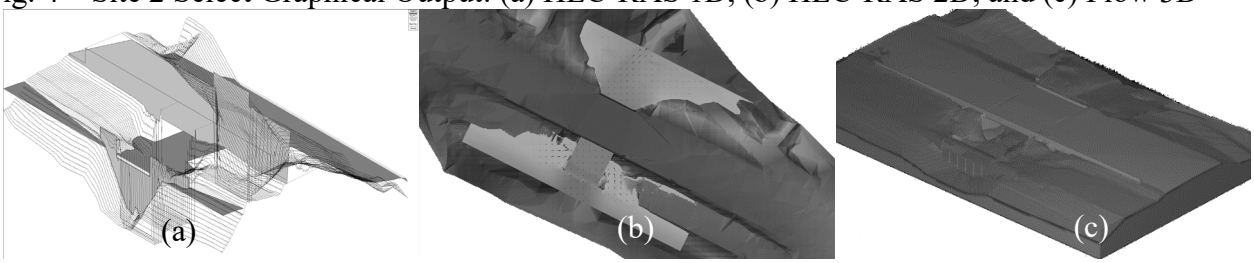

Fig. 5 – Site 2 Spillway Discharge Rating Curve

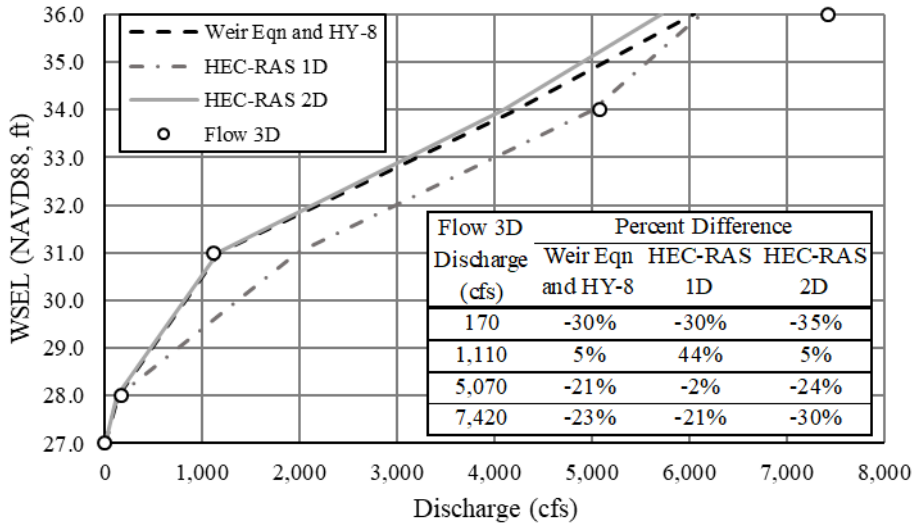

Flow 3D Discharge (cfs)	Percent Difference		
	Weir Eqn and HY-8	HEC-RAS 1D	HEC-RAS 2D
170	-30%	-30%	-35%
1,110	5%	44%	5%
5,070	-21%	-2%	-24%
7,420	-23%	-21%	-30%

For Site 2, the weir equation and HY-8 combination method tended to produce lower discharges for almost all tested reservoir levels of the Flow 3D model, save EL 31.0 where results showed good agreement. The HEC-RAS 1D results only showed good agreement at EL 34.0, otherwise discharges were not consistently lower or greater than those estimated with Flow 3D. HEC-RAS 2D produced results similar to the weir equation and HY-8 combination with slightly lower discharges estimated.

Although no verification of the results was possible due to the lack of measured physical hydraulic data, it is the author's opinion that the Flow 3D model better captured the complex hydraulics of Site 2, specifically flow over the walls perpendicular to the primary weir and the turbulent nature in the rectangular channel upstream of the bridge opening. For both Sites 1 and 2, differences among developed spillway discharge rating curves may have been due to a number of factors including: structure representation (e.g., inline structure, SA/2D Area Connection, STL image), selection of coefficients (e.g., constant weir coefficient, Manning's coefficient), boundary condition parameters (e.g., zero velocity), employed numerical method (e.g., finite difference, finite volume), bias from the modeller, etc. Without measured data it is difficult to know which method(s) produced the most accurate spillway discharge rating curve for the sites investigated. With additional information, it is likely that most if not all methods could be calibrated and brought into agreement with one another. However, it is often the engineer's knowledge and understanding of the available modelling techniques that allow for the successful estimation of a discharge rating curve and associated spillway capacity.

CONCLUSION

In this study, several modelling techniques were tested to develop spillway discharge rating curves for two spillways in Delaware, both in close proximity to downstream bridges and often subject to tailwater submergence. Each method produced a unique discharge rating curve; however, lower order methods that shared approximations tended to agree up to a site-specific threshold. The discharges calculated with 3D CFD were not always greater or lower than those calculated with empirical equations, 1D or 2D hydraulic computer models, or combinations thereof.

The successful selection of an appropriate modelling technique and interpretation of its results are dependent on an engineer's knowledge and understanding of the site-specific conditions and available methods. Careful consideration should be given to governing equations and effectiveness of representing site geometries when selecting which method(s) to use when developing a spillway discharge rating curve and associated spillway capacity, especially when complex site conditions or hydraulics may be better captured with a higher order model.

LIST OF SYMBOLS

C Weir coefficient [$L^{-1/2}T^{-1}$]

H_1 Upstream head [L]

H_2 Downstream head [L]
L Weir length [L]
n Exponent in the free discharge equation
Q Submerged volumetric flow rate [L^3T^{-1}]
Q_1 Free volumetric flow rate [L^3T^{-1}]

ACKNOWLEDGMENTS

The author would like to thank the Delaware Department of Transportation (DelDOT) and Department of Natural Resources and Environmental Control (DNREC) for their permission to use the results from SCHNABEL (2015). The author would also like to thank Dr. Brian Crookston and W. Kortney Brown for sharing their work on the Site 1 computer models, which helped establish the techniques used in this study.

REFERENCES

BRATER, E.F., and KING, H.W. (1976). "Handbook of Hydraulics." 6th Edition, McGraw Hill, New York, United States, pp. **5** – 1-45.

CHOW, V.T. (1959). "Open Channel Hydraulics." McGraw Hill, New York, United States, pp. 110-123.

COLORADO WATER CONSERVATION BOARD. (2006). "Chapter 12 Unique Hydraulic Conditions." *Colorado Floodplain and Stormwater Criteria Manual*, Colorado, United States, pp. CH12-603.

FEDERAL HIGHWAY ADMINISTRATION (FHWA). (2016). "HY-8 User Manual (v7.5)." United States Department of Transportation, Washington, D.C., United States, 116 pages.

FLOW SCIENCE. (2019). "FLOW 3D User Manual." Flow Science, New Mexico, United States.

HDR. (2014). "Comparison and Utilization of 1D, 2D, and 3D Hydraulic Models on a Complex Diversion Structure." HDR, Nebraska, United States.

RAO, P., HROMADKA II, T.V., HUXLEY, C., SOUDERS, D., JORDAN, N., YEN, C. C., BRISTOW, E., BIERING, C., HORTON, S., and ESPINOSA, B. (2017). "Assessment of computer modelling accuracy in floodplain hydraulics." *International Journal of Modelling and Simulation*, Vol. 37, No. 2, pp. 88-95.

SCHNABEL. (2015). "Assessment of Alternative Modeling Approaches." Schnabel Engineering, Pennsylvania, United States, 32 pages.

SOIL CONSERVATION SERVICE. (2003). "Revised Hydrology No. N4." United States Department of Agriculture, Washington, D.C., United States, 12 pages.

TOOMBES, L., and CHANSON, H. (2011). "Numerical Limitations of Hydraulic Models." *Proc. 34th IAHR World Congress – Balance and Uncertainty,* Brisbane, Australia, pp. 2232-2329.

U.S. ARMY CORPS OF ENGINEERS (USACE). (2016). "HEC-RAS River Analysis System." Hydrologic Engineering Center, California, United States, 906 pages.